dc_353_11

Analysis and exploitation of random fluctuations with simulations and hardware developments

DSc Dissertation

Zoltán Gingl

Szeged, 2012.

Table of contents

Preface

Most of the people think about noise what is certainly unpleasant and unwanted. For ordinary people it is a deterministic or random sound that is too loud or too irregular or just interferes with the information of interest. Engineers, physicists, chemists and biologists widen the scope to many kinds of signals including voltage, current, resistance, displacement, light intensity and even more – these may fluctuate randomly, which limits the precision of measurements and therefore limits the information extraction possibilities. In engineering and natural sciences considering random noise is unavoidable in most cases; we speak about signal-to-noise ratio and we still think that noise is something to be eliminated or at least it must be kept as low as possible.

However, randomness is an inherent feature of nature – noise can be found everywhere. Carrier fluctuations cause voltage and current noise in resistors, transistors and amplifiers; random movement of particles corresponds to temperature and pressure fluctuations of gases; diffusion is an inherently random process and quantum mechanics would not exist without a truly probabilistic background. Random fluctuations are present in climate changes, in levels of rivers, in social and economic processes, in heart rate and blood pressure variations, in evolution and behavior of living systems.

Noise output from a system can carry useful information about the system. Audible noise coming from the water in the pot informs us that the temperature is getting close to the boiling point; irregular noise emitted by engines is often an indicator of some dysfunction; integrated circuits regularly get noisier after partial degradation; and, surprisingly, decreased heart rate fluctuations suggest disease.

Noise can also be used as a tool to solve some commercial, technical or scientific problems. Digitized, rough images and characters displayed on a screen can be made more readable and natural by adding some amount of noise; security and PIN codes are generated randomly; random numbers are useful in numerical integration, optimization and in the so-called Monte Carlo – the town of games of chance – simulations and oddly enough, adding noise can improve the linearity of instruments and can even increase the signal-to-noise ratio in some cases – via the phenomenon called stochastic resonance.

The progressive and continuous advances in analog and digital electronics and informatics influenced the research of noise significantly, moved it toward information extraction methods and sophisticated signal processing algorithms that can be run even on very small battery powered devices. The beauty of noise research is its multidisciplinary character and the wide range of investigation methods from basic theoretical and experimental analysis to applied research in which engineers, physicists, computer scientists and many others can work together.

I have started my noise researcher career as a member of the group of Prof. L. Kish in Szeged, 1988. My debut as a speaker was at the International Conference on Noise and Fluctuations (ICNF) organized by Prof. A. Ambrózy – the author of the book Electronic Noise, McGraw Hill, 1983 – at the Budapest University of Technology and Economics in 1989 that was the only one event of this noise conference series held in Hungary. I was lucky that I could work in the lab of Prof. Ambrózy for a short period; I took part in the development of a computer controlled noise generator [A1]. Two other international noise conferences were particularly important for me: the conference series named Unsolved Problems of Noise (UPoN) that was founded by Prof. L. Kish and the first event that was organized in 1996, Szeged; and later I received the invitation to act

as chairman of the conference Noise in Complex Systems and Stochastic Dynamics in 2004, Spain [D22], as a part of the Fluctuations and Noise (FaN) symposium series. Finally, I would mention that I have been working for the unique journal Fluctuation and Noise Letters (http://www.worldscinet.com/fnl/) – exclusively dedicated to noise research – as a handling editor since 2002.

From the beginning I have been committed to do noise investigations in various ways and in many different systems. In the following chapters I shall present the most important results of my noise research conducted after my PhD title. The subjects include:

- fundamental research of 1/f noise properties;
- numerical simulation modeling of noise in electronic device degradation;
- development of a digital signal processor (DSP) based mixed-signal system to support experimental noise analysis;
- theoretical, experimental and numerical simulation investigation of signal-to-noise ratio gain improvement by stochastic resonance;
- hardware and software development for fluctuation-enhanced gas sensing;
- DSP system realization of secure communications utilizing noise.

I would like to note that the experience I have gained in noise research and in related hardware and software developments and signal processing has led to many interdisciplinary research collaborations. Just to mention a few examples, I have worked together with engineers (development of hardware, embedded and host computer software for optoelectronic component testing), laser physicists (active control of excimer laser delay utilizing jitter noise), chemists (fluctuation-enhanced sensing using carbon nanotubes), biophysicists (low-noise instrumentation of bacterial photosynthesis), computer scientists (hardware development to support handwriting recognition by inertial sensors), medical doctors (measurement and analysis of heart rate and blood pressure fluctuations and development of a 128 channel ECG mapping instrument) and even with secondary school teachers (educational applications of sensor-to-USB interfaces and virtual instrumentation technology).

Several parts of this thesis reflect these multidisciplinary findings that, I believe, have been of benefit to those involved and, at the larger scale, to society.

Szeged, 2012. February 22. Zoltán Gingl

1 Amplitude saturation invariance of 1/f$^{\alpha}$ fluctuations

1.1 About 1/f noise

It was a long time ago that 1/f noise (also known as flicker noise, pink noise), whose power spectral density (PSD) is inversely proportional to the frequency, was first discovered in the current fluctuation of a vacuum tube [1,2]. Since then, the topic has been studied intensively, and a considerable amount of knowledge has accumulated.

Rather different systems exhibit 1/f fluctuations. They are found in semiconductors [3,4], superconductors [5], lasers [6,7], astrophysical data [8] and quantum phenomena. It has also been reported that 1/f noise is present in neurons [9], traffic flow [10], geophysical records [11] and even classical music [12]. 1/f spectrum has been found in the long term behavior of the heart rate fluctuations [13] –note that oddly enough too low fluctuations may indicate disease [14] –, in many biological, chemical systems and processes.

Modern instruments and measurement devices use active electronic components like transistors, operational amplifiers, data converters and many other integrated circuits – all of them exhibit some amount of noise that may limit accuracy and reliability. Operational amplifier data sheets include information about input voltage and current noise spectral density always showing 1/f like behavior at low frequencies, typically below a few hundred Hz. Since the variance of 1/f noise is getting higher as the measurement time is increasing, averaging in the time domain does not reduce the statistical error that is something important to keep in mind.

1/f noise has some strange properties: it is at the boundary of stationary processes; it is logarithmically divergent at both high and low frequencies; it is hard to treat it mathematically; it cannot be derived from other well known noise sources (e.g. white noise) using simple linear operations like integration or differentiation which makes 1/f noise models rather complicated and/or limited in most cases [15].

A full understanding of the phenomenon has not been arrived at, especially with respect to the origin of this kind of fluctuation. Concerning the generality of 1/f noise; there are two basic different views:

- There must be some universal mechanism responsible in all systems which exhibit 1/f noise,
- There is no common origin and one should invoke different models for each system.

This problem is still open; the presence of 1/f noise in several different systems has not been completely accounted for, hence 1/f noise is sometimes considered to be a mysterious phenomenon. Research into the properties of 1/f noise can help to construct new models and may lead to a more precise understanding of the systems exhibiting this kind of noise.

1.2 1/f noise generation

1/f noise generators are used in several applications [16,17,18]. In scientific projects they provide the noise for investigation of its properties; they can be used as sources for excitation of various systems or can also be integrated in a complex simulation environment to analyze the behavior of the system under consideration.

Noise generators are also used in system transfer function measurements and in system analysis. Their advantage is the distribution of their power both in the time and in the frequency domain. For example, a linear system can be excited by a pulse or white noise, because both have wide bandwidth. However the pulse has strictly limited distribution of its power in time, while the noise power is distributed in time. 1/f noise has a unique property that makes it useful in system analysis: it has the same power in any frequency range, where the middle frequency and the bandwidth ratio is the same. For example, if one considers a 1/f noise driven tunable bandpass filter whose quality factor is given, the output power is the same for any filter frequency setting. Due to this fact, 1/f noise generators are often used in audio system testing.

Noise generators can be purely numerical in computer simulations but in real world applications and tests analog noise generators are required. Analog generators are typically realized by analog or mixed signal (both analog and digital) circuits [A1] and their output can be converted into many other quantities by the use of proper actuators upon request.

In the following we report the 1/f noise generation methods we have used in our research. Development of a mixed signal digital signal processor (DSP) based generator will also be shown.

1.2.1 Software 1/f noise generation

There are many different ways of generating 1/f noise samples by software. The basis of these generators is the pseudo-random number generator that provides random-like numbers although the generation is deterministic [19]. Linear congruence and XOR-shift generators are popular due to their simple use, fast execution, availability of reliable performance tests [19-21]. Still one should be careful about using unspecified generators come with software packages and compilers. For example the old generator called RANDU built in older FORTRAN systems has poor performance [19]

Pseudo-random generators provide uncorrelated samples that correspond to white noise. Correlated noises – like 1/f noise – can be obtained by processing these samples in either the “time” or “frequency” domain. For example, properly designed finite impulse response (FIR) filters, cascaded infinite impulse response (IIR) filters, fractional integration can do the job using the time series, but transforming the signal into the frequency domain using discrete Fourier transform (DFT) or fast Fourier transform (FFT) allows manipulations in the frequency domain. There are always accuracy, efficiency and frequency band limitations due to the special nature of 1/f noise.

In our numerical simulations we used an FFT-based method [16,17]. The samples were generated by tested pseudo-random generators and FFT was used to convert the data into the frequency domain. The transformed signal was then multiplied by the square root of the required power spectral density. The drawback of this method is that the number of samples must be given to do the transformation therefore it can’t be used to generate continuous stream of 1/f noise samples. However, in our investigations this was not required while the high accuracy and fast execution of the method helped us to obtain reliable results and the use of high number of averages.

1.2.2 DSP 1/f noise generator hardware

In order to produce reliable 1/f noise voltage we have developed a DSP based noise generator [A2]. The principle of the device is shown on Figure 1.1.

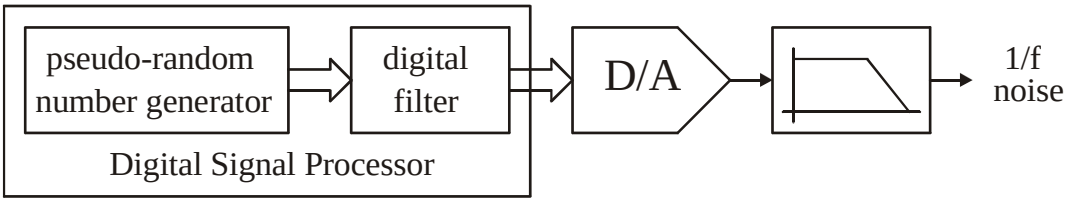

Figure 1.1. *Block diagram of the DSP 1/f noise generator circuit. The pseudo-random number generator outputs white noise that can be properly filtered to approximate 1/f noise. The D/A converter is used to provide the analog signal while the low-pass filter removes any unwanted images.*

A DSP is used to generate the pseudo-random numbers and it performs the digital filtering to get 1/f noise samples. The numbers representing 1/f noise are converted into the analog domain by a digital-to-analog converter (DAC). Due to the nature of the sampled data system and stepped digital-to-analog conversion, the DAC output signal contains so called images above the Nyquist frequency and the spectrum is distorted by a sin(x)/x shape. This latter can be taken into account during the design of the digital filter while the images can be attenuated by a low-pass analog filter.

We have chosen the probably the most often used method to generate 1/f noise from white noise. According to the principle 1/f noise can be approximated by the sum of noises whose spectrum follows the Lorentz-function, $A_i/(1+f^2/f_{c,i}^2)$ that can be easily obtained by passing a white noise through a first order low-pass filter [23-24]. The A_i amplitudes and $f_{c,i}$ corner frequency of the individual signals must follow the rule $A_i/A_{i+1} = f_{c,i+1}/f_{c,i} = 10^{1/M}$, where M is the number of signals per decade. Figure 1.2 illustrates how these signals approximate the 1/f noise in a given frequency band.

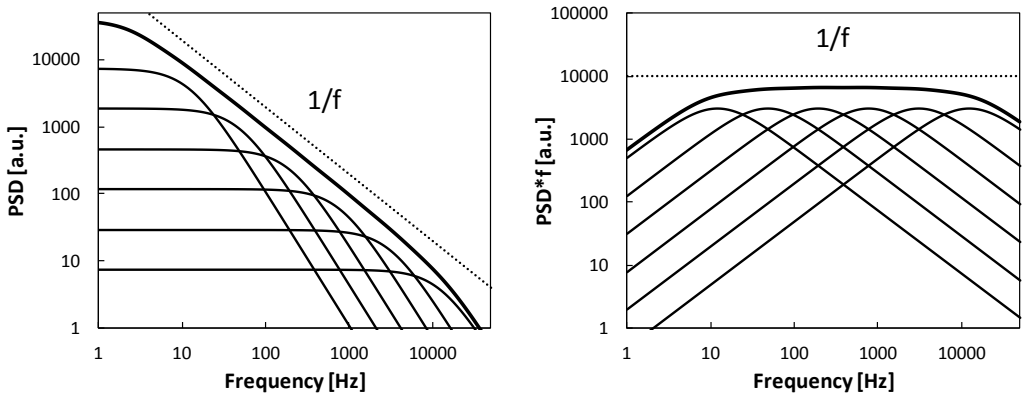

Figure 1.2. *The thick solid line shows the sum of properly selected first order low-pass filtered white noises (thin curves). The dotted line represents ideal 1/f noise.*

For a sampled data system the low-pass filters can be simply realized by IIR filters. In general, the IIR digital equivalent of an analog filter can be found by using the bilinear transform. Note that the sampled data frequency scale is rather different from the real frequency scale at frequencies close to the Nyquist point, and this should be taken into account. If the frequency range and tolerance is given, the number of signals and their parameters can be calculated. R. Mingesz has developed a method to determine the optimal parameters, 1% accuracy can be achieved by using two signals per decade over four decades of frequency [A2]. Figure 1.3 shows the block diagram of the principle discussed above.

We have designed and built two DSP 1/f generator circuits. The simplest, compact design is based on a 16-bit fixed-point DSP, the ADSP2105. Only four integrated circuits were used: the DSP, a boot EPROM, a serial input 12-bit DAC (AD7233) and an operational amplifier (AD845) configured as a Sallen-Key low-pass filter.

The tested linear congruence pseudo-random generator [19,25]

$$x_i = (1664525 \cdot x_{i-1} + 32767) \bmod 2^{32} \tag{1.1}$$

was used to calculate the x_i 32-bit unsigned integer pseudo-random numbers and the sum of ten IIR filters provided the 1/f noise samples. The processor's timer generated the 100kHz update rate, the associated interrupt routine was used for the signal processing. The schematic diagram of the design can be seen on Figure 1.4 and the measured power spectral density of the output of the device is depicted on Figure 1.5.
Note that we also developed a more powerful and accurate version based on the faster ADSP-2181 processor and a 14-bit DAC (AD7836). This much more universal hardware is developed in order to support many different scientific and technical applications and it will be detailed in Chapter 3.

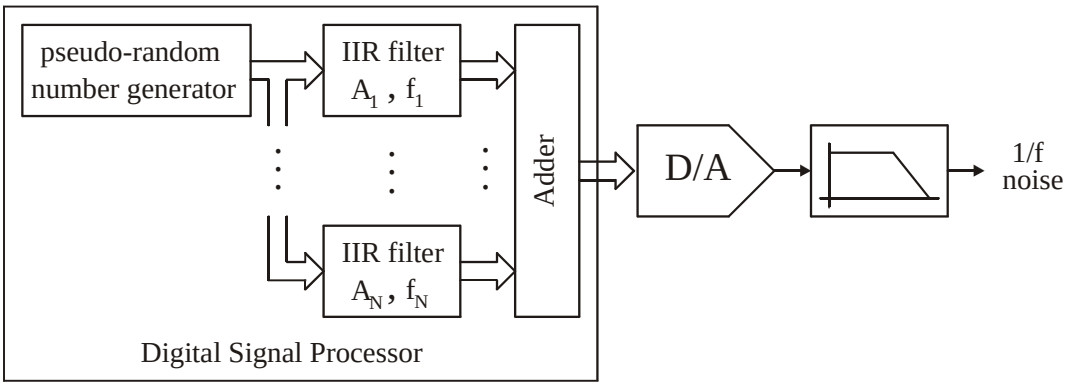

Figure 1.3. *A set of first order digital low-pass IIR filters can be used to generate noises with different amplitudes and cut-off frequencies. The sum of these signals has power spectral density approximately proportional to 1/f in a certain frequency band.*

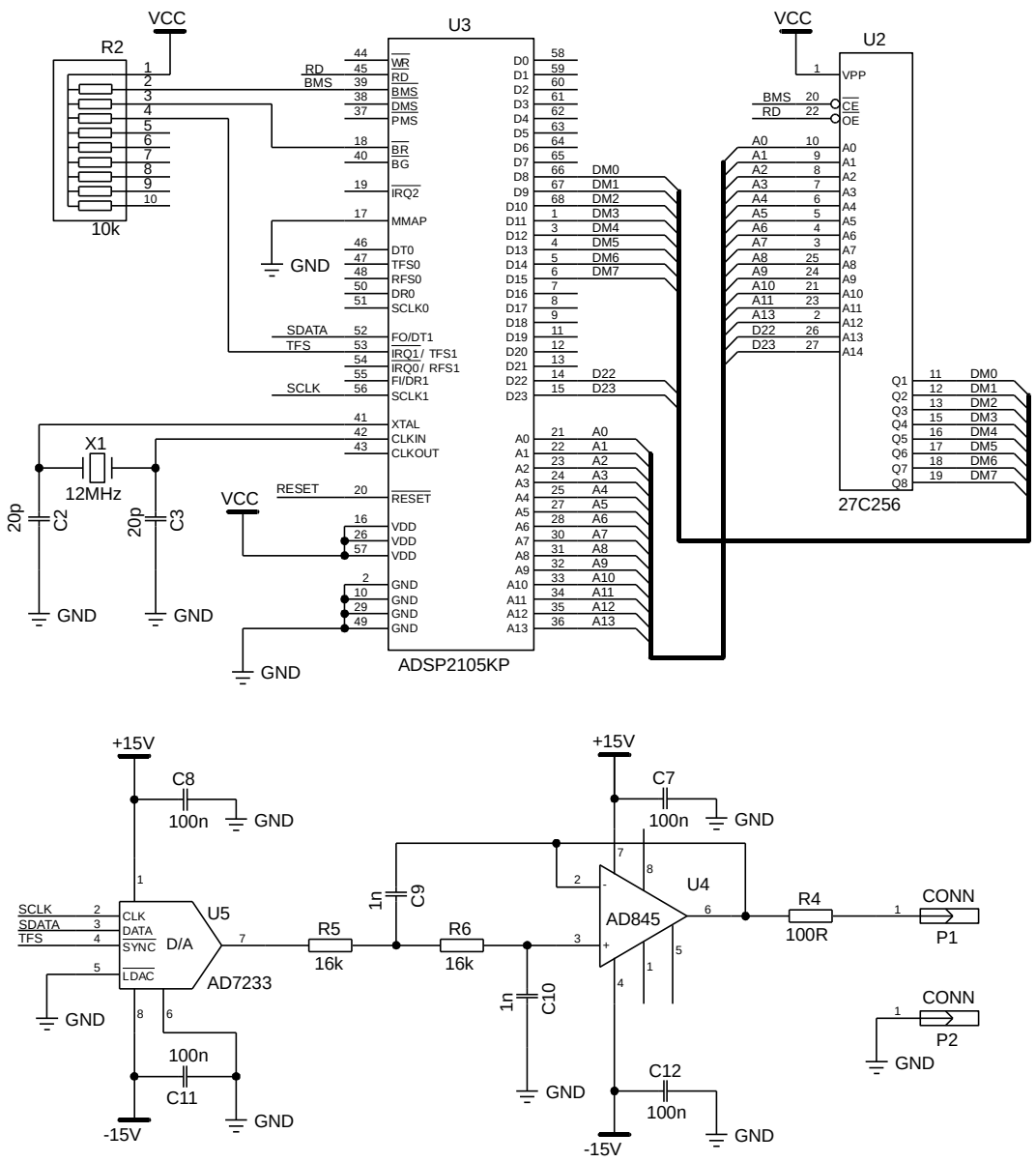

Figure 1.4. *Schematic diagram of the DSP 1/f noise generator circuit. The fixed point DSP generates the pseudo-random numbers and performs the digital filtering. The D/A converter is driven by the serial port of the DSP and an analog filter is used to attenuate the images. Only four integrated circuits are used: the DSP, the boot EPROM, the D/A converter and an operational amplifier.*

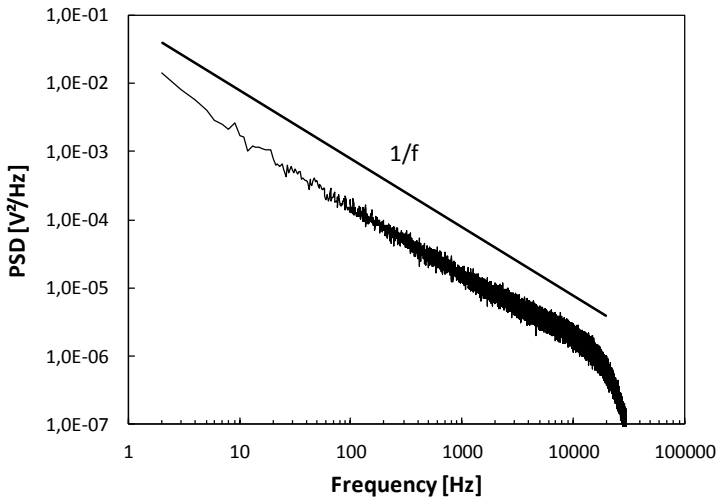

Figure 1.5. *Measured power spectral density of the outputs signal generated by the DSP 1/f noise generator circuit. The noise is close to 1/f over almost four decades of frequency.*

1.3 Amplitude saturation of 1/f fluctuations

1/f noise has several properties that make it unique from some aspects as we have already pointed out in the introduction of this chapter. In addition to these, an interesting property of Gaussian 1/f noise has been found experimentally: the power spectral density remains close to 1/f, if the sign of the noise is kept only [A3]. Two years later we have broadened this during the investigations of 1/f noise driven stochastic resonance: the power spectral density remains the same if the amplitude is saturated at certain levels under rather general conditions [A4, A5]. Later we have extended the analysis to 1/f$^\alpha$ noises with $0<\alpha<2$ by experimental investigations and numerical simulations, but these results were theoretically unexplained [A6]. Finally we have found the theoretical derivation of the above mentioned invariant property for certain cases. In addition, we have examined the phenomenon for even more general conditions with the help of numerical simulations. In the following we show the most important part of our experimental and theoretical work and we also draw the attention to some unsolved problems associated with the amplitude saturation of 1/f$^\alpha$ noises.

1.3.1 1/f noise in a single comparator and a Schmitt-trigger

The following formula produces a dichotomous noise *y(t)* based on the polarity of the input noise *x(t)*:

$$y(t) \propto \begin{cases} +1, & if\ x(t) \geq 0 \\ -1, & if\ x(t) < 0 \end{cases} \tag{1.2}$$

Diffusion noise with power spectral density proportional to 1/f$^{3/2}$ can be obtained if *x(t)* represents the one dimensional random walk with 1/f^2 PSD [22,26]. An experimental setup has been built by G. Trefán [A3] to generate such noise, but besides 1/f^2 noise 1/f noise was also used and the output PSD was close to 1/f in that case. The block diagram of the system is shown on Figure 1.6.

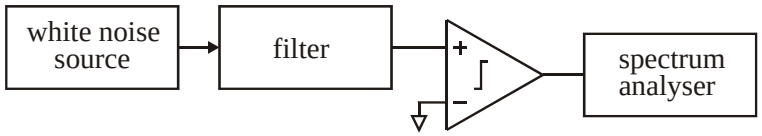

Figure 1.6. *Block diagram of the experimental setup used to measure the power spectral density of the sign of 1/f noise. The properly filtered white noise provides the 1/f noise that drives the comparator's input.*

The experimental study of stochastic resonance (will be detailed in Chapter 4) required a simple bistable system driven by noise and a periodic signal [A4]. The simplest bistable circuit is the Schmitt-trigger whose operation can be described by the following equation:

$$y(t) \propto \begin{cases} +1, & if\ x(t) > x_{\max} \\ -1, & if\ x(t) < x_{\min} \\ no\,change, & otherwise \end{cases} \tag{1.3}$$

Figure 1.7 shows the block diagram of the experimental setup.

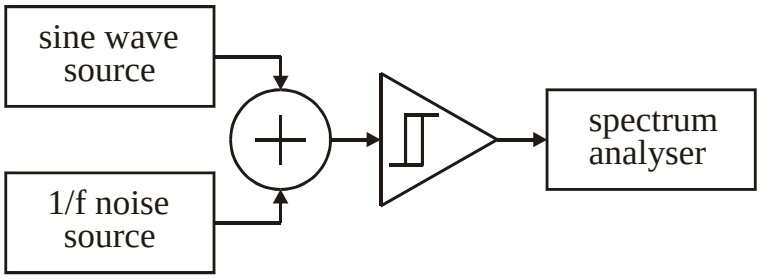

Figure 1.7. *Block diagram of the system used to investigate stochastic resonance in a bistable system, in the Schmitt-trigger.*

We have applied a small amplitude sinusoidal signal plus 1/f noise and found that the output spectrum has two parts:

- above a certain corner frequency it is proportional to $1/f^2$,
- below this frequency it gets close to 1/f.

This behavior seemed to be the same for various threshold levels of the Schmitt-trigger, only the corner frequency has been changed.

Figure 1.8 shows a typical output power spectral density obtained by numerical simulation. The noise root mean square (RMS) amplitude was set to 1, the switching levels of the Schmitt-trigger were -1 and 1 and the sinusoidal signal had amplitude of 0.2. The 1/f noise was generated using the frequency domain method described earlier; the length of the sequences was 8192 points. The PSD is given as an average of 1000 runs.

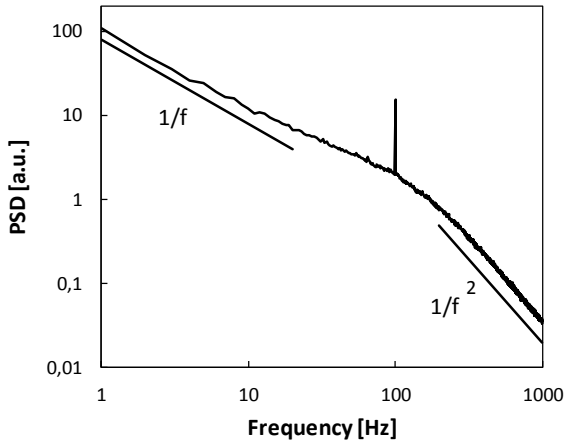

Figure 1.8. *Simulated power spectral density at the output of a Schmitt-trigger driven by a periodic signal plus 1/f noise. The Schmitt-trigger thresholds are -1 and 1, the noise RMS is 1 and the amplitude of the sinusoidal signal is 0.2, the frequency is 100Hz. At low frequencies the spectrum remains close to 1/f.*

1.3.2 Various saturation levels

In order to explore the amplitude saturation properties of 1/f fluctuation in a more general manner the following transformation can be considered [A5]:

$$y(t) = \begin{cases} x_{\max}, & \text{if } x(t) > x_{\max} \\ x_{\min}, & \text{if } x(t) < x_{\min} \\ x(t), & \text{otherwise} \end{cases} \tag{1.4}$$

The amplitude saturation operation is illustrated on Figure 1.9.

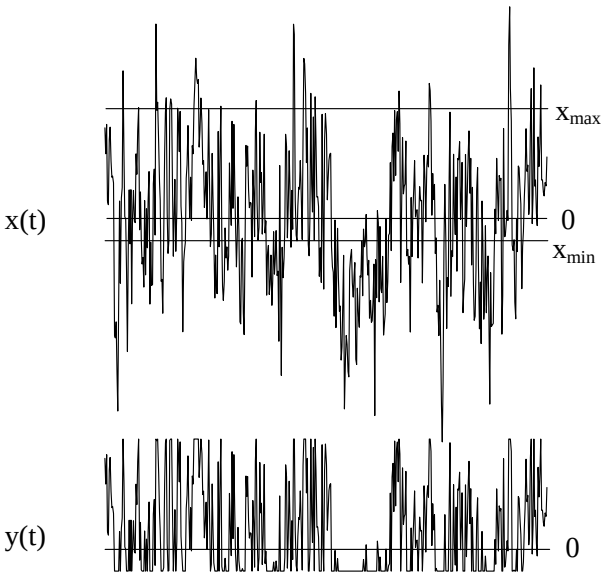

Figure 1.9. *Amplitude saturation of a typical 1/f noise sample*

Three rather different saturation examples and the corresponding power spectral densities are shown on Figure 1.10.

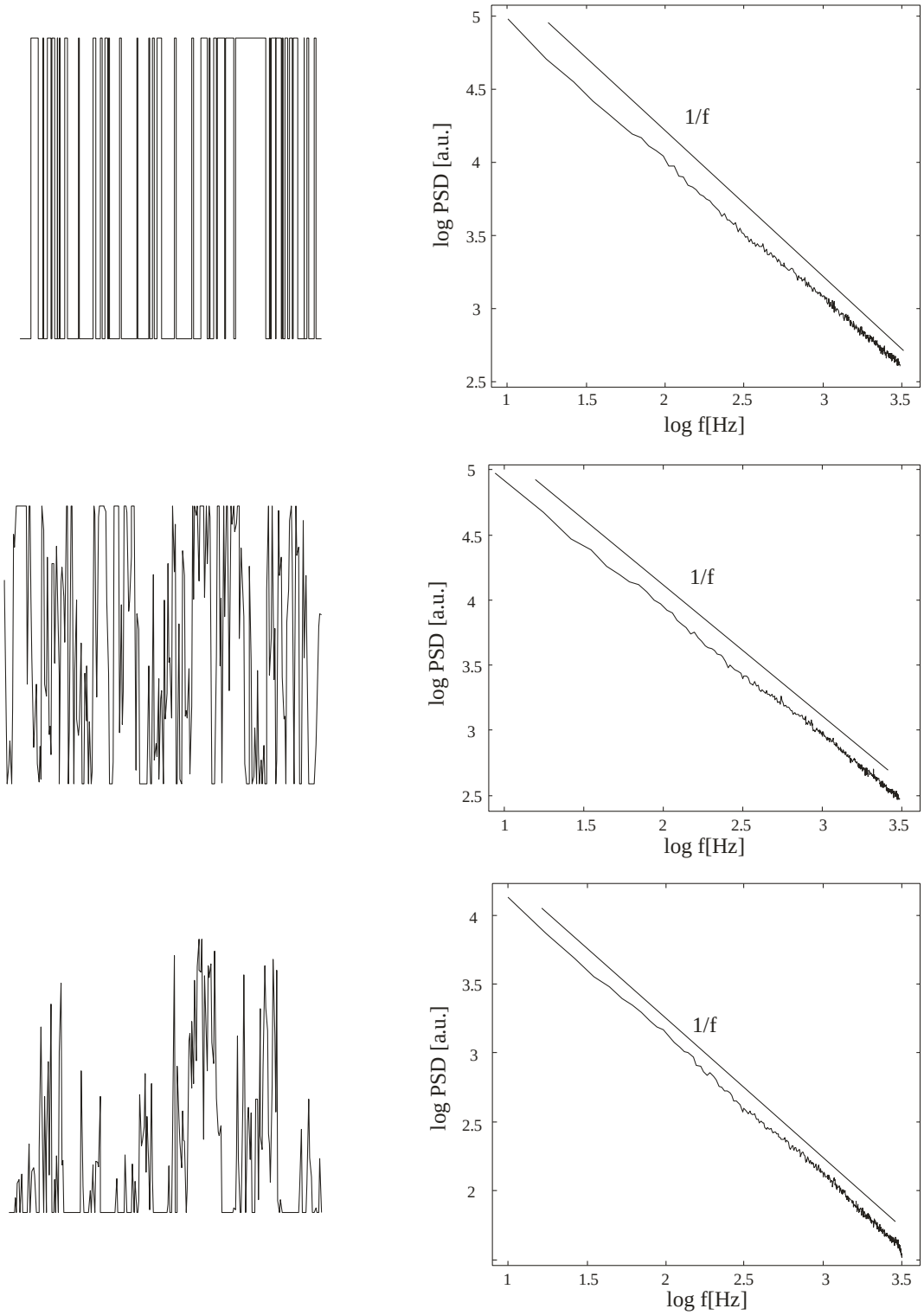

Figure 1.10. *Amplitude saturation examples of a typical 1/f noise sample. The amplitude saturated signals are shown on the left, the corresponding spectra can be seen on the right hand side. For all cases the spectrum of the saturated signal remains very close to 1/f.*

1.4 Amplitude saturation of 1/f$^\alpha$ fluctuations

The results mentioned above implied the consequence that 1/f noise may have a special feature that its PSD is invariant to almost any kind of amplitude saturation. Note that the two saturation levels always included the mean of the noise, later we'll address this point in a bit more detail.

The question easily arises: is it unique to 1/f noise or can be valid for other kind of noises? Since 1/f noise can be viewed from a more general point, namely it is quite typical to use the term 1/f noise even when one observes 1/f$^\alpha$ PSD, where α is not equal to 1, rather a range is specified, in most cases from 0.8 to 1.2 as these values are often found in real systems. Therefore it is straightforward to consider noises that have PSDs proportional to 1/f$^\alpha$.

1.4.1 Simulation results

First we show the numerical simulation results for the amplitude saturation analysis of 1/f$^\alpha$ noise [A6]. We have investigated the case when the mean value of input noise is zero and the upper and lower saturation levels are symmetric and very close to the mean value: x_{min}=-x_{max}≈0. In this case, we get an almost dichotomous output signal *y(t)*, which can be approximated by the following formula:

$$y(t) \propto \begin{cases} +1, & if\ x(t) \geq 0 \\ -1, & if\ x(t) < 0 \end{cases} \tag{1.5}$$

According to our results the output signal's PSD has 1/f$^\beta$ dependence and our aim was to find the relation between α and β. The 1/f$^\alpha$ noise was generated using the frequency domain method described earlier; the length of the sequences was 2^{18} points. The PSD is given as an average of 1000 runs.

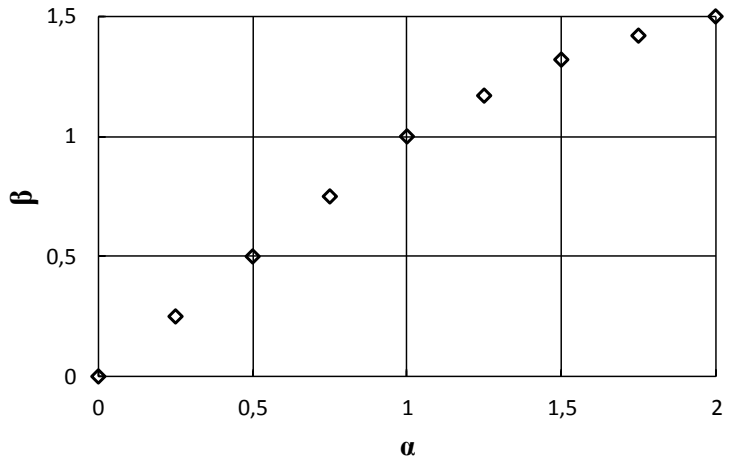

Figure 1.11. *Exponent β of the truncated signals PSD versus the exponent α of the input PSD. The data are obtained by numerical simulations.*

Figure 1.11 shows the result of the simulation. One can see that α and β are practically the same in the range of 0 to 1, while above 1 β is smaller than α. The case of α=0 (white noise) and α=2 (1/f^2 noise) were already known, since the PSD of the white noise is obviously invariant to amplitude saturation, because it remains uncorrelated. The dichotomous diffusion noise whose PSD is proportional to 1/f$^{3/2}$ can be derived

from 1/f^2 noise representing a one-dimensional random walk or Brownian motion. The simulation results are in agreement with these facts.

1.4.2 Theoretical results for dichotomous output signals

In 1997 we have started collaboration with the research group of S.Ishioka and N. Fuchikami at the Tokyo Metropolitan University in the subject and the theoretical explanation of the phenomenon had been found [A7-A10]. Note again that we have considered the case of dichotomous output signal when the saturation levels are almost zero and the mean of the noise is zero as well. In the following the main steps of the calculation will be presented.

First we derive the relation between the correlation functions $R_x(t)$ and $R_y(t)$ of the input and output signals, respectively. The correlation function of the output signal is given by

$$\begin{aligned} R_y(t) &= (+1)\cdot P(y(0)\cdot y(t)=1) + (-1)\cdot P(y(0)\cdot y(t)=-1) \\ &= P(x(0)\cdot x(t)>0) - P(x(0)\cdot x(t)<0) = 2\cdot P(x(0)\cdot x(t)>0) - 1 \end{aligned} \tag{1.6}$$

where *P(.)* is the probability that the condition of the argument is satisfied.
If we assume a stationary Gaussian process, the joint probability density is

$$P(x(t_1), x(t_2)) = P(x(0), x(t_1 - t_2)) = \frac{1}{A_0} e^{-(x^2 - 2cxy + y^2)/B} \equiv f(x,y), \tag{1.7}$$

where $x \equiv x(0)$, $y \equiv x(t_1\text{-}t_2)$, $c \equiv R_x(t_1\text{-}t_2)$, $A_0 \equiv 2\pi R_x(0)\cdot(1\text{-}c^2)^{½}$, $B \equiv 2R_x(0)\cdot(1\text{-}c^2)$, $R_x(t)$ is the correlation function of $x(t)$. Using Equation 1.7 the probability $P(xy>0)$ can be written as

$$P(x\cdot y>0) = \int_0^\infty\int_0^\infty f(x,y)dxdy + \int_{-\infty}^0\int_{-\infty}^0 f(x,y)dxdy = \frac{1}{2} + \frac{1}{\pi}\arcsin(R_x(t)). \tag{1.8}$$

Therefore we obtain

$$R_y(t) = \frac{2}{\pi}\arcsin(R_x(t)). \tag{1.9}$$

The relation (1.9) between the correlation functions leads to the relation between power spectral densities (PSD) applying the Wiener-Khinchine theorem, because we have assumed stationary processes

$$\begin{aligned} S_I(\omega) &= 2\int_0^\infty R_I(t)\cos(\omega t)dt = -2\int_0^\infty R_I(t)\frac{\sin(\omega t)}{\omega}dt, \\ I &= x, y \end{aligned} \tag{1.10}$$

It turns out that the PSD of the form $S_x(\omega)\sim 1/\omega^{\alpha}$ is transformed into PSD $S_y(\omega)\sim 1/\omega^{\beta}$.

We have investigated the relation of the exponents α and β for the following cases: $0<\alpha<1$, $\alpha=1$ and $1<\alpha<2$.

1.4.2.1 Case 1<α<2

For $1<\alpha<2$, we have chosen the correlation function

$$R_x(t) = \begin{cases} 1 - t^{\alpha-1}, & if\ t \le 1 \\ 0, & if\ t > 1 \end{cases} \tag{1.11}$$

The corresponding PSD can be calculated using Equation (1.10):

$$\begin{aligned} S_x(\omega) &= 2\frac{\alpha-1}{\omega^{\alpha}}\int_0^{\omega}\frac{\sin(z)}{z^{2-\alpha}}dz \\ &= \frac{2}{\omega^{\alpha}}\left[\Gamma(\alpha)\sin[\pi/2(\alpha-1)] - (\alpha-1)\int_{\omega}^{\infty}\frac{\sin(z)}{z^{3-\alpha}}dz\right] \end{aligned} \tag{1.12}$$

At high frequencies (ω>>1), the second term can be neglected because the integrand sin $x/x^{2-\alpha}$ becomes small for $x \ge \omega >> 1$, so the spectrum becomes ~$1/\omega^{\alpha}$. The high frequency condition ω>>1 actually means that $\omega >> 1/\tau_1$, where τ_1 is a correlation time of the signal. Using Equations (1.11) and (1.9), we obtain the correlation function of the output signal as

$$\begin{aligned} R_y(t) &= \frac{2}{\pi}\arcsin(1-t^{\alpha-1}) && (t \le 1) \\ &\sim 1 - 2\frac{\sqrt{2}}{\pi}\sqrt{t^{\alpha-1}} && (t << 1) \\ R_y(t) &= 0 && (t > 1) \end{aligned} \tag{1.13}$$

The transformed signal's PSD becomes

$$S_y(\omega) \sim \frac{1}{\omega^{\beta}}, \quad \beta = \frac{\alpha+1}{2} \quad (\omega >> 1), \tag{1.14}$$

in the high frequency limit, because when ω>>1, the main contribution to the integral (1.10) comes from small values of t, thus the approximation of (1.13) can be used.

1.4.2.2 Case 0<α<1

In the case of 0<α<1, the correlation function is chosen as

$$R_x(t) = \begin{cases} 1, & if\ t \le 1 \\ \dfrac{1}{t^{1-\alpha}}, & if\ t > 1 \end{cases} \tag{1.15}$$

Using Equation (1.10), the corresponding PSD is obtained as

$$S_x(\omega) = 2\int_1^{\omega}\frac{\sin(\omega t)}{t^{2-\alpha}\omega}(\alpha-1)dt = \frac{2}{\omega^{\alpha}}\left[\Gamma(\alpha)\cos(\pi/2\alpha) - (1-\alpha)\int_0^{\omega}\frac{\sin(z)}{z^{2-\alpha}}dz\right] \tag{1.16}$$

At low frequencies (ω<<1) the second term can be neglected, because 1<2-α<2 and we get $S_x(\omega)$~$1/\omega^{\alpha}$. The dimensionless relation $\omega << 1$ actually corresponds to $\omega << \tau_2$, where τ_2 is a typical time scale of the system above which the correlation function decays. The correlation function

$$R_x(t) = \frac{1}{1+t^{1-\alpha}}, \tag{1.17}$$

also leads to the same form of PSD, because this expression of $R_x(t)$ may be replaced by (1.15) in the integral of Equation (1.10) if ω<<1.

Substituting Equation (1.15) into (1.9) gives the correlation function of the output signal:

$$\begin{aligned} R_y(t) &= 1 && (t<1) \\ R_y(t) &= \frac{2}{\pi}\arcsin\left[\frac{1}{t^{1-\alpha}}\right] && (t\geq 1) \\ &\sim \frac{2}{\pi}\frac{1}{t^{1-\alpha}} && (t>>1) \end{aligned} \tag{1.18}$$

Using the approximation of Equation (1.18) in (1.10), we obtain

$$S_y(\omega)\sim\frac{1}{\omega^{\beta}},\quad \beta=\alpha,\quad (\omega<<1), \tag{1.19}$$

in the low frequency limit.

1.4.2.3 Case α=1

For 1/f noise (α=1) the correlation function is approximated by the following formula:

$$R_x(t)=\begin{cases}1, & if\ t\leq 1\\ \dfrac{1}{1+\log t}, & if\ t>1\end{cases} \tag{1.20}$$

Using this function the PSD calculated as

$$S_x(\omega)=\frac{2}{\omega}\int_{\omega}^{\infty}\frac{\sin(z)}{(1+\log z/\omega)^2 z}dz \tag{1.21}$$

Assuming ω<<1, 1+log(x/ω) can be replaced by log(1/ω) in the integrand and we get

$$S_x(\omega)\sim\frac{2}{\omega(\log 1/\omega)^2}\int_0^{\infty}\frac{\sin(x)}{x}dx=2\frac{\pi}{2}\frac{1}{\omega(\log 1/\omega)^2}. \tag{1.22}$$

The correlation function

$$R_x(t)=\frac{1}{1+\log(t+1)}, \tag{1.23}$$

can also be used to get the same approximated PSD as (1.22). The PSD of the output signal is given by the formula

$$S_y(\omega)\sim 2\frac{1}{\omega(\log 1/\omega)^2}\quad (\omega<<1), \tag{1.24}$$

in the low frequency limit.

The PSDs were calculated over the same frequency range for the input and output signals, and in summary we found that the exponent β of the output PSD depends on the exponent α of the input PSD as follows:

$$\beta=\begin{cases}\alpha, & if\ 0<\alpha\leq 1\\ \dfrac{\alpha+1}{2}, & if\ 1<\alpha<2\end{cases} \tag{1.25}$$

The approximations used to derive this relation (ω<<1 for 0<$\alpha\leq$1 and ω>>1 for 1<α<2) were verified by the numerical integration of Equation (1.10), into which the proper correlation function was substituted. Figure 2 shows the results of the numerical integration for the cases of α=0.75, α=1 and α=1.25.

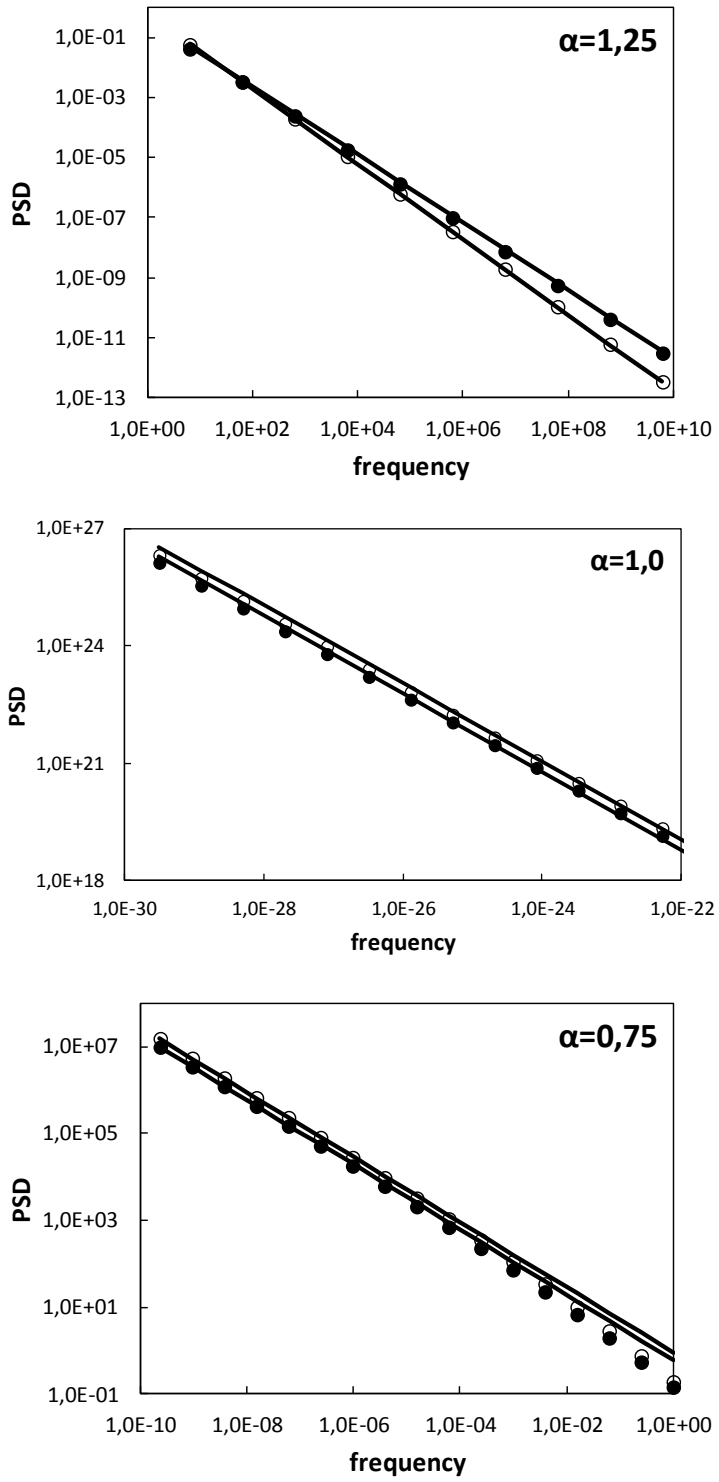

Figure 1.12. *PSD of the input (hollow circles) and output (filled circles) signals obtained by numerical integration for α=1.25, α=1 and α=0.75. The solid lines represent ideal 1/f$^{\alpha}$ and 1/f$^{\beta}$ spectra*

Our results have been confirmed by numerical simulations also. Gaussian noises with length of 2^{18} were generated, and the PSD was calculated by averaging 1000 samples. On Figure 1.13 the numerical simulation result for 1/f noise (α=1) is plotted and Figure 1.14 shows how the numerical simulation confirms Equation (1.25).

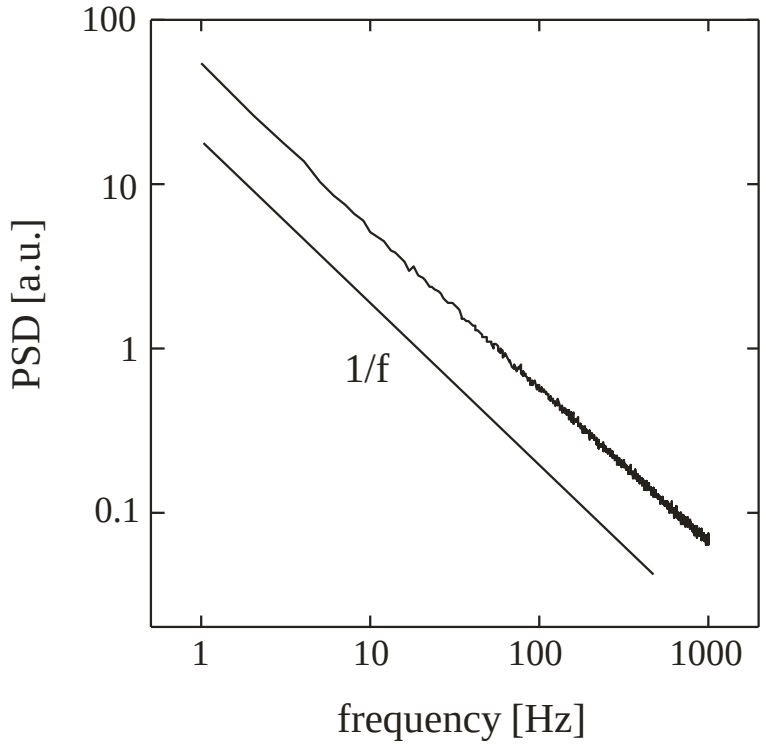

Figure 1.13. *Power spectral density of the simulated 1/f noise obtained by averaging of 1000 samples.*

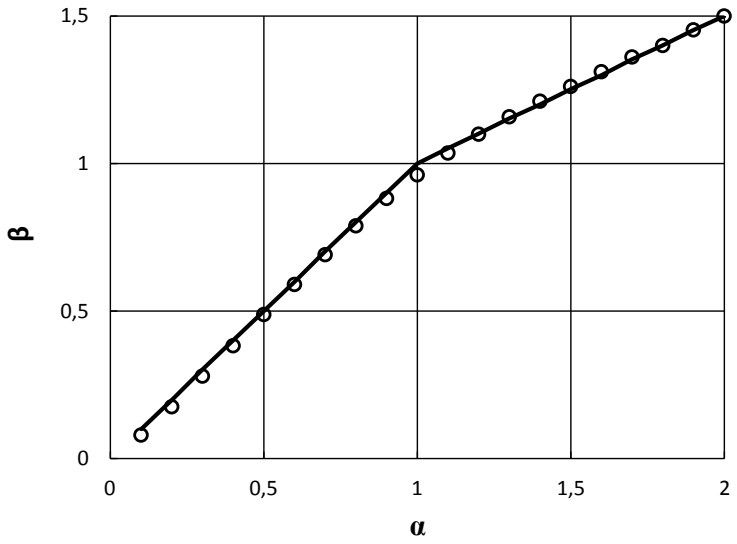

Figure 1.14. *Exponent β of the saturated signal's PSD versus the exponent α of the input PSD. The solid line represents the theoretical result, the circles show data obtained by numerical simulation.*

1.4.3 Extending the theoretical results to other saturation levels

The above results for very close truncation levels can be generalized to distant truncation levels as well [A9-A10]. Let us assume that we have a zero-mean Gaussian 1/f$^{\alpha}$ noise and truncation levels $x_{min}<0<x_{max}$. For short time intervals (high frequencies)

the PSD of the truncated signal is mainly determined by the noise amplitude behavior between the levels. On the other hand, for time intervals much longer than the time required by the signal to pass between the two levels, the signal has similar PSD as in the case of low levels. If $\alpha \leq 1$, this means that the spectrum has the same dependence both for low and high frequencies, while for $\alpha > 1$ the low frequency part below a certain corner frequency has exponent $\beta=(\alpha+1)/2$, while for high frequencies $\beta=\alpha$ is expected. The corner frequency depends on the truncation levels, of course. Let us assume that the truncation is symmetric, i.e. $x_{max}=-x_{min}=U$. When the level is changed from U to aU, then the corner frequency changes from f_c to $a^{-2/(\alpha-1)}f_c$ for $1<\alpha<2$. This scaling property can be obtained from the self-affine character of the signal $x(t)$. Note that this argument does not hold for cases in which the mean of the input noise is not located between the truncation levels.

1.4.4 Behavior at asymmetrical truncation levels excluding the mean value

We have carried out numerical simulations for cases when the mean value of the noise is not included in the interval defined by the upper and lower truncation levels. Equation (1.25) does not hold valid for this case, however the output PSD seems to follow a power law again with a modified value of β. Figure 5 illustrates the results for 1/f input noise, where both the upper and lower truncation levels are close to σ (label 2), 2σ (label 3) together with the previous case (label 1). Here σ is the standard deviation of the simulated noise.

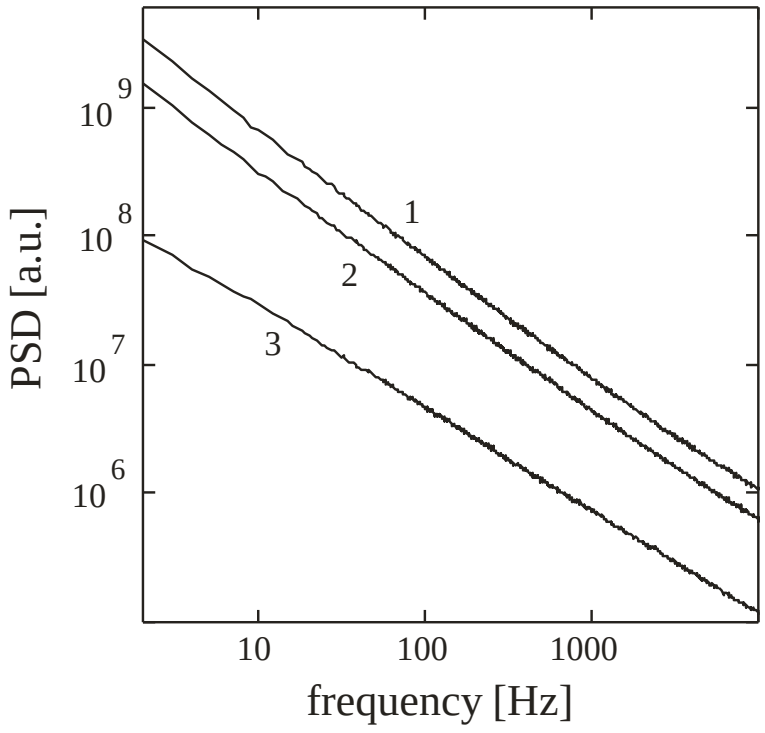

Figure 1.15. Output PSDs for 1/f input noise with truncation levels located at 0, σ, and 2σ labeled with 1,2,3, respectively. The corresponding slopes are ;0.98, 0.91, and 0.8.

The theoretical result of Equation (1.25) cannot be applied to these cases as the phenomenon is rather complex here.

1.5 Conclusions

Two results related to Gaussian 1/f$^{\alpha}$ fluctuations have been shown. We reported about the development of a compact and accurate DSP-based 1/f$^{\alpha}$ generator that can be used as a tool to support experimental analysis and can serve as a signal source for system analysis and mixed signal simulations.

Our discovery of the special invariant property of these fluctuations related to amplitude saturation is a significant addition to the knowledge about 1/f$^{\alpha}$ fluctuations and can help to understand the origin, general occurrence and special behavior of these fluctuations. The results obtained by measurements and numerical simulations followed by theoretical explanation of the invariance of the PSD of Gaussian 1/f$^{\alpha}$ fluctuations against the amplitude saturation for $0<\alpha\leq 1$ and the dependence for $1<\alpha<2$ has also been derived. The theoretical results are extended to asymmetrical and distant truncation levels between which the mean value of the noise is located. Note here that the 1/f$^{3/2}$ PSD of diffusion noise can be obtained using amplitude truncation of 1/f^2 noise [22] in accordance with Equation (1.25) even though $\alpha=2$ is not included in our theoretical derivation.

The theoretical results do not include the case when the saturation levels both are above or under the mean value. Our numerical simulations show that the PSD of the truncated signals follows a power law again, but the exponent β of the output PSD has a theoretically unexplained dependence on the exponent α of the input PSD.

In natural systems, measurements and data communications noise is always present, and several non-linear transformations can occur including amplitude saturation. Simple examples are signals with limited amplitude range, overdriven systems and systems with saturating transfer functions. It is obvious that linear amplifiers exhibit this behavior due to the supply-limited output range. Note that investigations of other non-linear transforms of 1/f$^{\alpha}$ noises might also help to understand these noises more precisely. Since the PSD is invariant to almost any truncation of the amplitude, the level-crossing dynamics seem to play a crucial role concerning the spectral dependence.

Our result may also suggest a possible convergence from 1/f^2 noise to 1/f noise via successive amplitude saturation processes on the sum of multiple fluctuations. Dichotomous 1/f$^{\alpha}$ noises – like 1/f noise in ion channel switching fluctuations – might also be related to this interesting invariance.

2 Biased percolation model for degradation of electronic devices

Reliability is probably the most important factor in many applications of electronic devices. All modern instruments, machines, health-care and life-saving devices, industrial and medical robots – just to name a few only – are using more and more electronic circuits and components. Early detection and prediction of the failure of such components is extremely important and in most cases must be performed during operation with proper sensitivity and of course, only non-destructive methods can be applied and the information can only be read from the signals coming from the system under consideration during natural operation [1-13].

The progressive miniaturization of electronic components, very large scale integration often result in excessive current densities and increased operating temperature – both increase the probability of the damage of some parts of the circuit [1].

Experimental and theoretical investigations of the degradation process often caused by stress induced voids, mechanical or electromigration show special change of the conductivity, inhomogeneous distribution of the defects, filamentary damage pattern and a definitely increased 1/f noise [2].

Percolation models – where random connectivity in a complex system is considered [14] – are successfully applied to study the conductivity and noise in random resistor networks [14-22] with conductor-superconductor and conductor-insulator transitions [18-19]; a random fuse model has been introduced for the failure of disordered materials [23-25].

We have introduced a new type of percolation model called biased percolation that is promising in understanding and analyzing the degradation process and can serve as a sensitive, non-destructive diagnostic tool and early predictor of failure using the noise as information source [B1-B13].

2.1 Biased percolation model of electronic device degradation

Our simple model for a homogeneous thin film resistor mounted on a substrate is a two dimensional resistor network contacted at two sides, see Figure 2.1. For simplicity we consider a square lattice of identical resistors whose value is unity, 1Ω. In our model a defect is represented by resistor that has infinite value, in other words, by an open circuit. Note, that one can also consider a short circuit-like defect; we'll discuss this possibility later. Our aim is to

- define a defect generation process at the microscopic level;
- calculate microscopic quantities (current distribution);
- calculate macroscopic quantities (sample resistance, current, noise);
- determine the time evolution of the quantities.

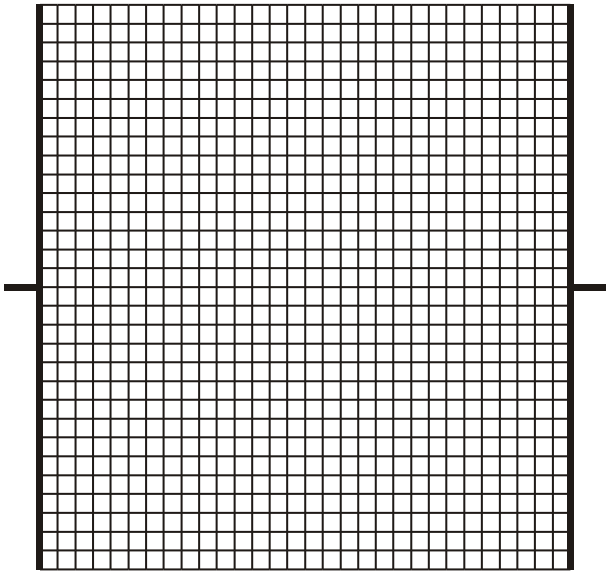

Figure 2.1. *Resistor network model of a thin conducting film. The thin lines represent resistors, while the thick lines show the contacts.*

In our model the defect generation is a thermally activated statistical process that we have included in our Monte Carlo simulations. The probability of generating a defect at a given position *k* in a simulation step is given by the following formula:

$$W_k = \exp\left(-\frac{E_0}{k_B T_k}\right) \tag{2.1}$$

where E_0 is the activation energy of the defect generation, k_B is the Boltzmann constant and T_k is the temperature of the resistor. Since the power generated by the current flowing through the resistor is equal to the resistor value multiplied by the square of the current, assuming linear dependence of the temperature versus power we can get

$$T_k = T_0 + A r_k i_k^2 \tag{2.2}$$

where T_0 is the temperature of the substrate and the value of parameter A depends on the thermal coupling between the film and the substrate. If the heat coupling is perfect, then the film has the same temperature as the substrate that means A is zero, therefore the probability if generating a defect is

$$W_k^0 = \exp\left(-\frac{E_0}{k_B T_0}\right). \tag{2.3}$$

This case we call *free percolation*, it is the classical 2D percolation well known in many other systems [14]. Since this percolation process does not depend in the local current distribution in the lattice, it will give homogeneous defect pattern. However, when A is nonzero, a defect is generated with higher probability where the current flowing through the local resistor is higher. If a defect is generated at a certain position, the current in the neighboring resistors will be increased; therefore the probability of generating a defect is higher close to a defect. This will result in an inhomogeneous defect pattern and we call this process *biased percolation.* Biased or directed percolation can occur in many different systems with external excitations [26-28].

2.2 Development of the numerical simulation framework

In order to carry out Monte Carlo simulations, we have developed an optimized software framework in C and later in C++ programming language.

2.2.1 Determining the voltages and currents in the network

The solution of the network means that we have to calculate all node voltages and all currents flowing though the resistors. Connecting a voltage source between the contacts will force current through the sample. A simple way to calculate the local currents is the method of the loop currents, when Kirchhoff's second law is used to write an equation for each loop. Figure 2.2 illustrates a 3x3 resistor network and the association of the loop currents. The numbering of the loops can be optimized to reduce the required computational power dramatically, as it will be shown later.

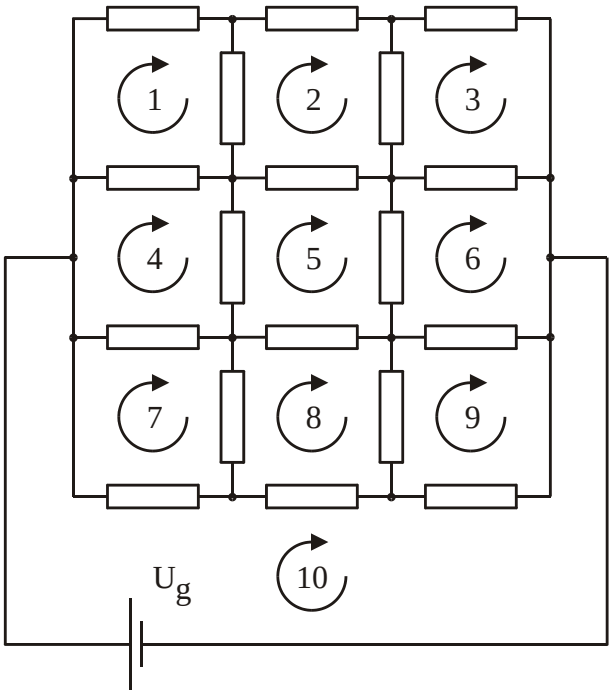

Figure 2.2. *3x3 resistor network solution scheme. The directed arcs correspond to the loop currents, the last loop contains the voltage generator.*

The loop equation system can be written in this form:

$$\begin{pmatrix} 0 \\ 0 \\ 0 \\ 0 \\ 0 \\ 0 \\ 0 \\ 0 \\ 0 \\ U_g \end{pmatrix} = \begin{pmatrix} r_{11} & r_{12} & 0 & r_{14} & 0 & 0 & 0 & 0 & 0 & 0 \\ r_{21} & r_{22} & r_{23} & 0 & r_{25} & 0 & 0 & 0 & 0 & 0 \\ 0 & r_{32} & r_{33} & 0 & 0 & r_{36} & 0 & 0 & 0 & 0 \\ r_{41} & 0 & 0 & r_{44} & r_{45} & 0 & r_{47} & 0 & 0 & 0 \\ 0 & r_{52} & 0 & r_{54} & r_{55} & r_{56} & 0 & r_{58} & 0 & 0 \\ 0 & 0 & r_{63} & 0 & r_{65} & r_{66} & 0 & 0 & r_{69} & 0 \\ 0 & 0 & 0 & r_{74} & 0 & 0 & r_{77} & r_{78} & 0 & r_{710} \\ 0 & 0 & 0 & 0 & r_{85} & 0 & r_{87} & r_{88} & r_{89} & r_{810} \\ 0 & 0 & 0 & 0 & 0 & r_{96} & 0 & r_{98} & r_{99} & r_{910} \\ 0 & 0 & 0 & 0 & 0 & 0 & r_{107} & r_{108} & r_{109} & r_{1010} \end{pmatrix} \begin{pmatrix} i_{L1} \\ i_{L2} \\ i_{L3} \\ i_{L4} \\ i_{L5} \\ i_{L6} \\ i_{L7} \\ i_{L8} \\ i_{L9} \\ i_{L10} \end{pmatrix} \tag{2.4}$$

or in a short form

$$u = R \cdot i_L \,, \tag{2.5}$$

where i_L is the vector of the loop currents; u is the vector whose elements are the signed sum the voltage sources in the corresponding loop; the R matrix has the elements R_{ij} that is the signed sum of the network resistors that belong both to the i-th and to the j-th loop. One can see that only the last loop has nonzero voltage source, and the resistance matrix has many zero components, it has a form of a band matrix.

For an N by N network the number of resistors is $2N(N+1)$ and the number of equations is N^2+1. Although there are $(N^2+1)^2$ coefficients in the resistance matrix, the number of nonzero coefficients in the above arrangement is reduced to less than $(2N+1)(N^2+1)$. Therefore the numerical solution of the equation systems needs less than $(2N+1)^2(N^2+1)/2$ operations. Without this optimization $(N^2+1)^3/2$ operations would be required. For example, a 100x100 network has 20200 resistors and the number of equations is 10001. The optimization gives close to 2500 times faster execution. The code written in C took less than 10 seconds on a DEC Alpha workstation installed at the University of Lecce, where we have carried out the Monte Carlo simulations in 1995 in collaboration with C. Pennetta and L. Reggiani. Later we have developed a graphical user interface version [B14] that allowed easier simulations and real-time visualization as well, see Figure 2.3.

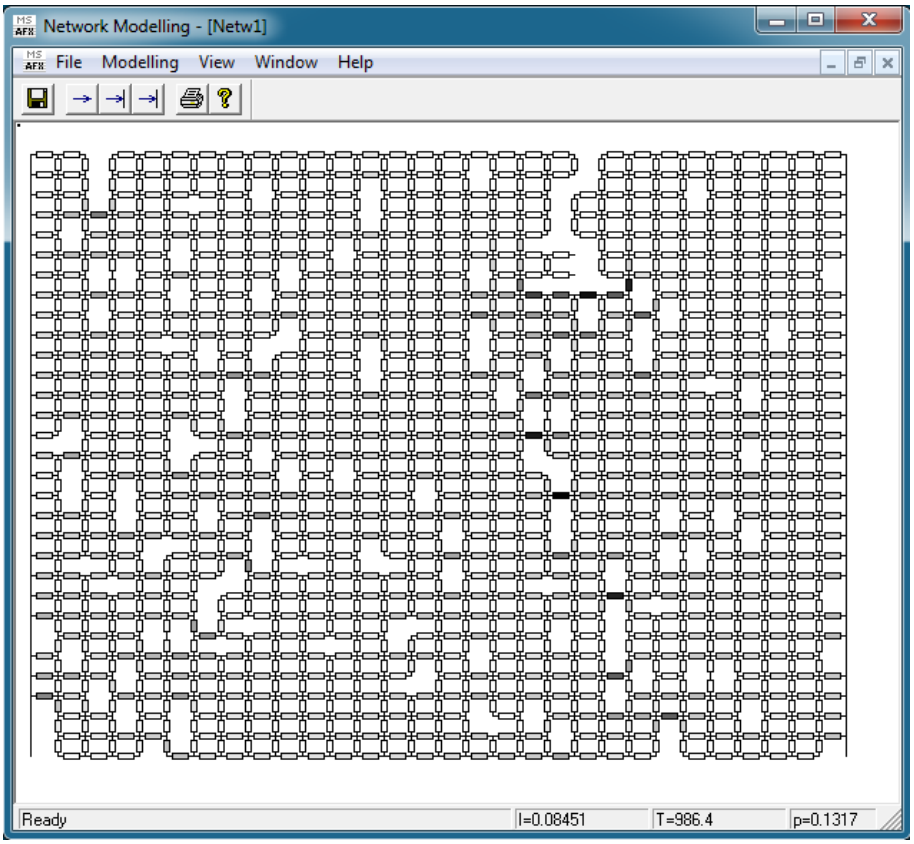

Figure 2.3. *Graphical user interface of the network modeling software. The user can set all modeling parameters, can monitor the simulation process. The status bar shows the actual current, temperature and probability of creating a defect at the resistor on which the user has been clicked. Darker resistors are warmer and carry higher current.*

Figure 2.4 shows a completely degraded lattice in the case of free percolation, there is no conducting path between the two contacts. Figures 2.5-2.6 illustrate the damage patterns and current distribution in the network close to the failure for the case of free and biased percolation processes, respectively. These figures clearly visualize the differences between the two kinds of degradation. The free percolation exhibits homogeneous damage pattern and current distribution while the biased percolation causes a filamentary damage pattern, defect grow perpendicular to the global current flow and strong inhomogeneity.

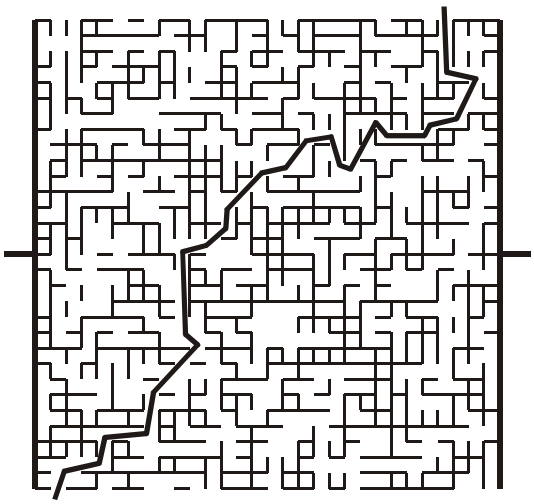

Figure 2.4. *Completely degraded 30x30 resistor network. The free percolation shows homogeneous defect creation pattern. The thick solid line helps to find the insulating path.*

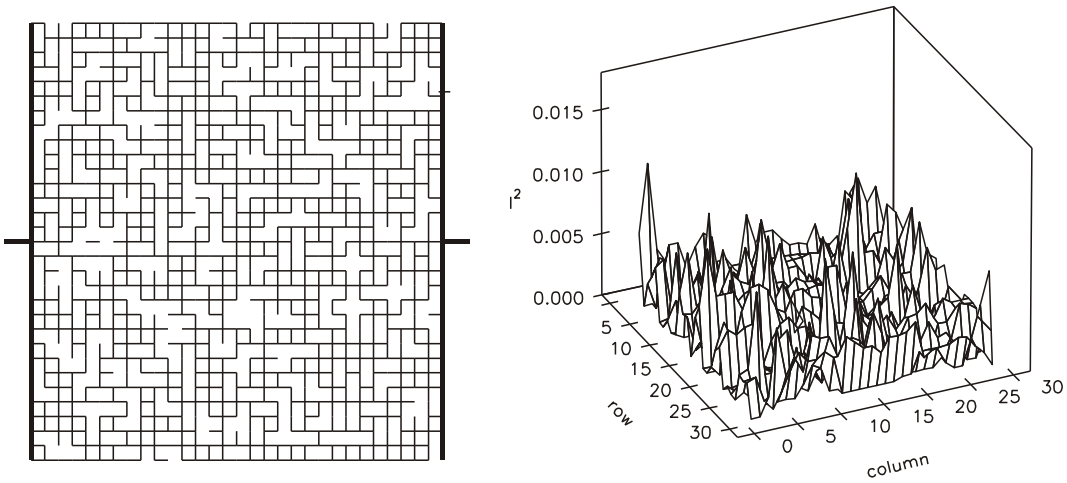

Figure 2.5. *Partially degraded 30x30 resistor network in the case of free percolation. The corresponding distribution of the squared currents can be seen on the right.*

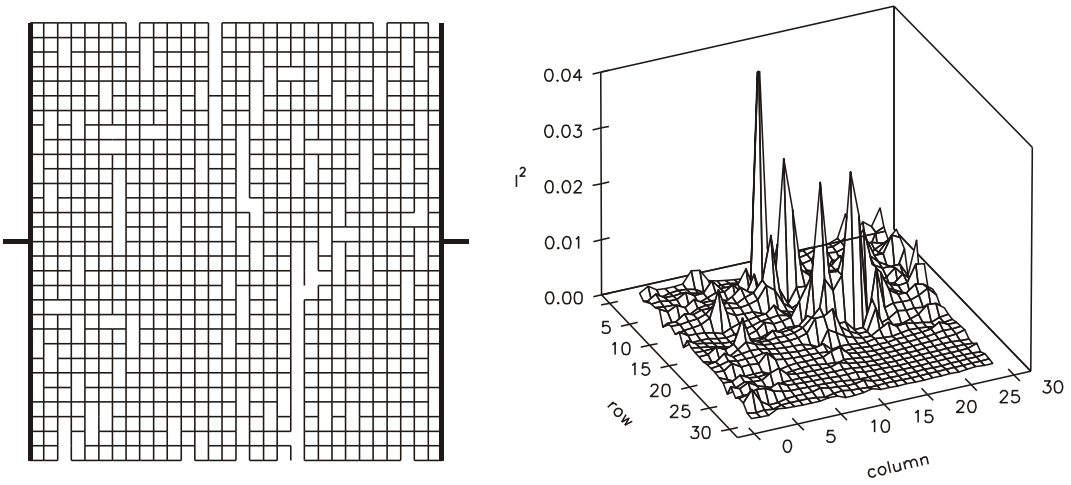

Figure 2.6. *Partially degraded 30x30 resistor network in the case of biased percolation shows a filamentary damage pattern. The corresponding distribution of the squared currents can be seen on the right.*

2.2.2 Calculating the fluctuations

Solving the above described equations by Gauss elimination one can get the values of all loop currents therefore the local currents can also be known. After completing the elimination the sample resistance can be given by R_{MM}, where $M=N^2+1$.

Assuming the each resistor is fluctuating in time as $r_k+\delta r_k(t)$. For simplicity, all resistors have the same mean value $r_k=r$ and the same variance of the fluctuations $<\delta r_k(t)>^2=\rho^2$. Using Cohn's theorem [15,29] it is possible to calculate the relative variance of the total network resistance as

$$\frac{\left\langle \delta R^2 \right\rangle}{R^2} = \frac{\rho^2}{r^2} \frac{\sum_k i_k^4}{\left(\sum_k i_k^2 \right)^2}, \tag{2.6}$$

if $\rho^2<<r^2$.

2.2.3 Time evolution of the resistance and resistance fluctuations

In order to determine the time evolution of the sample resistance and its fluctuations we have carried out Monte Carlo simulations using a 100x100 resistor network. The substrate temperature T_0 was 300K, the activation energy and Boltzmann constant ratio E_0/k_B was equal to 3000K, the thermal coupling parameter A was $100 \cdot N^2$K/W, we assumed 1Ω resistors in the network and the 1V excitation voltage applied at the contacts. In each Monte Carlo step all the currents were calculated then the local temperatures and the corresponding defect generation probabilities were determined using Equation (2.1). The random decision was made at each location using the defect generation probability to replace the resistor with an open circuit to represent a defect. Note that the open circuit corresponded to a reasonable high resistance value of $10^9\Omega$ to avoid problems with the numerical representation.

Figure 2.7 shows a typical evolution of the sample resistance and its variance for the free and biased percolation cases. It can be clearly seen that much shorter time is required for a significant degradation of the sample in the case of biased percolation.

The reason is twofold. It is obvious from figures 2.5 and 2.6 that during biased percolation much smaller number of defects can cause total degradation. In addition, the defect generation probability is higher at the locations where the current is increased.

On one hand the degradation process is faster but it is also more abrupt. This means that it is harder to predict the failure, therefore research to find other indicators is important.

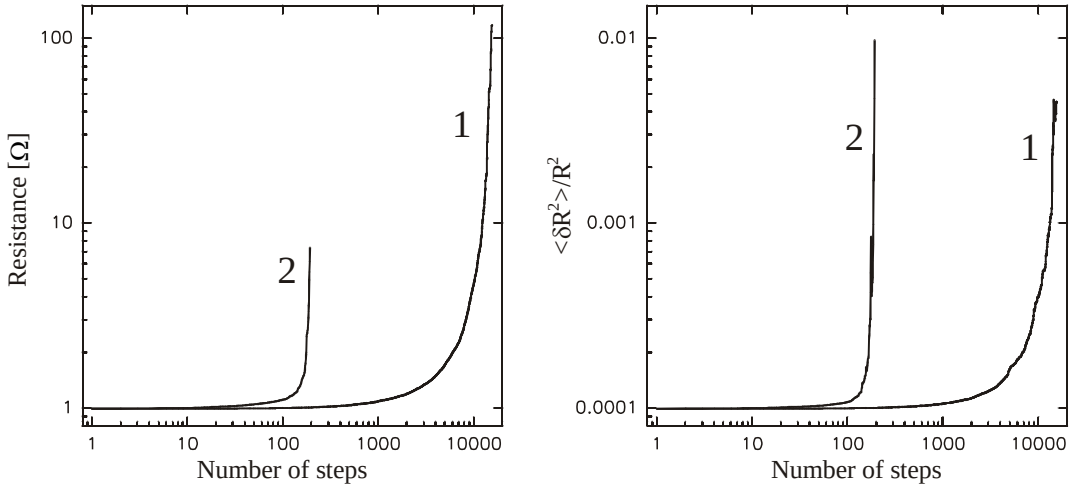

Figure 2.7. *Evolution of the sample resistance and normalized variance during the degradation process in a 100x100 lattice caused by free (label 1) and biased (label 2) percolation processes. Both quantities show faster and more abrupt change in the case of biased percolation.*

During the evolution both the resistance and the variance of its fluctuations increase. The dependence of these quantities on each other differs significantly in the free or biased percolation cases as can be seen on Figure 2.8. Both curves have linear shape in a log-log plot indicating power law dependence that is normally observed in percolation phenomena:

$$\frac{\langle \delta R^2 \rangle}{R^2} \propto R^{\gamma} \tag{2.7}$$

The free percolation theory for 2D lattices results γ=0.86 [14-16], however we have found γ=2.05±0.08 for the biased percolation process. This finding is in agreement with experimental results that show much stronger increase of the noise during the degradation process that can be predicted by usual percolation models.

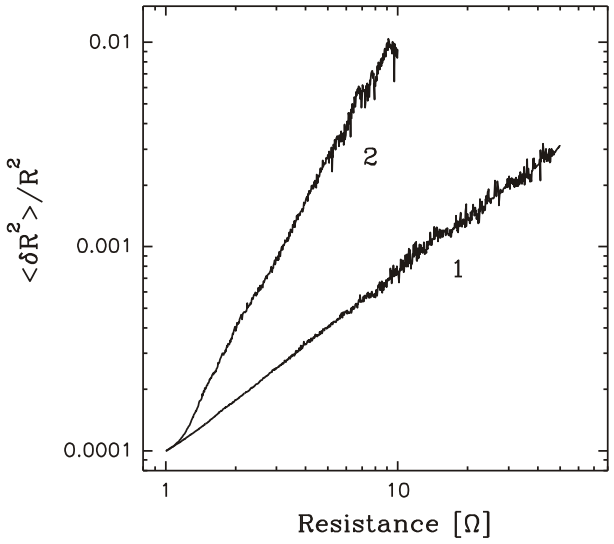

Figure 2.8. *Normalized variance as a function of the total resistance of the lattice for the cases of free (label 1) and biased (label 2) percolation models, respectively. Curves refer to average values over 10 and 50 samples, respectively, with sizes 100x100.*

We have carried out numerical simulations also for the case when short circuits (conductor-superconductor transition) are generated as defects rather than open circuits (conductor-insulator transition). This way it is possible to analyze the case when the experiments show decrease of the resistance during the degradation process. The similarities are discussed in detail in our publication here we only show a few typical findings.

Figure 2.9 compares the relative variance of the total resistance as a function of the total resistance for the cases of conductor-superconductor transition and conductor-insulator transition. The plot suggests that the two processes are counterparts in the sense that the absolute value of the scaling exponent γ is close to 2 in both cases while its sign is the opposite.

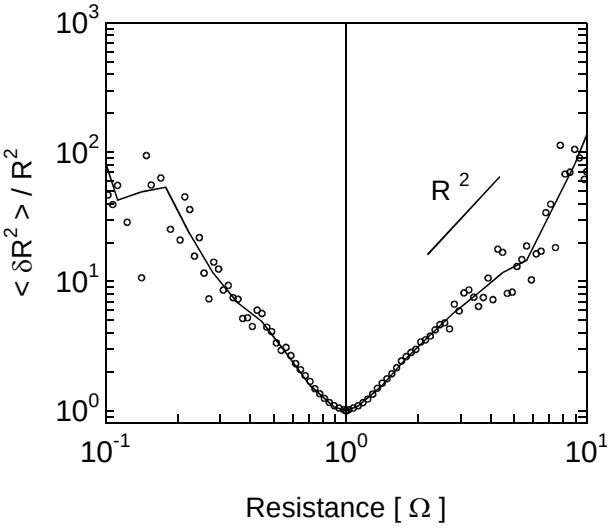

Figure 2.9. *Relative variance of the total resistance as a function of the total resistance, for the cases of conductor-superconductor transition (left part of the figure) and conductor-insulator transition (right part of the figure). Constant-voltage operation mode and a substrate temperature of 300 K are assumed. Points are representative of about 6000 data originating from 50 samples with sizes 100x100. Continuous line interpolates these points, each point is representative of an average of the data made on a hyperbolic density sampling.*

2.2.4 Temperature dependence

In this section we report the dependence of the resistance and normalized resistance fluctuations on the substrate temperature. If the temperature is lower, then more steps (longer time) is needed for the degradation, however the transition is more abrupt as it is visualized by Figure 2.10. The conductor-superconductor and conductor-insulator transitions exhibit very similar degradation behavior.

We have also investigated the lifetime of the sample as a function of the substrate temperature both for constant current and constant voltage operation modes. At the actual value of E_0 these results show a roughly T_0^{-4} decrease of the lifetime in the low temperature region 77 K < T0<200 K. This dependence bends at temperatures above 200 K, where the two operation modes give results which differ significantly, current mode being associated with a longer lifetime. The power dissipated under constant voltage conditions increases during degradation, while it decreases when the total current is kept constant. Both the figures 2.10 and 2.11 show the longer lifetime at reduced substrate temperatures that is due to the longer time needed to generate the first defects after that the degradation process will be significantly accelerated.

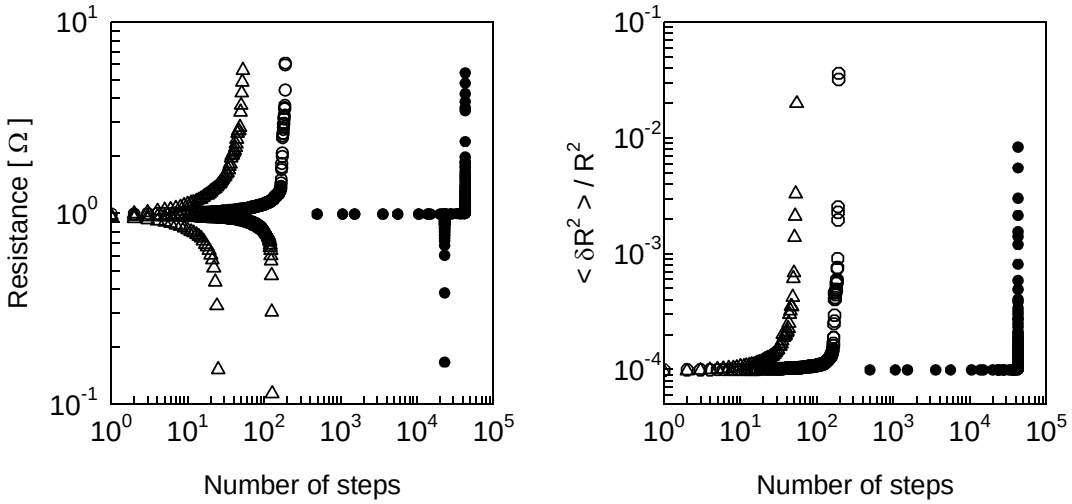

Figure 2.10. *Evolution of the sample resistance (left panel) and variance of the resistance fluctuations (right panel) normalized to R^2 under constant-voltage condition. Triangles, open circles and full circles refer, respectively, to a substrate temperature of 500K, 300K and 77K. The sizes of the sample are 100x100.*

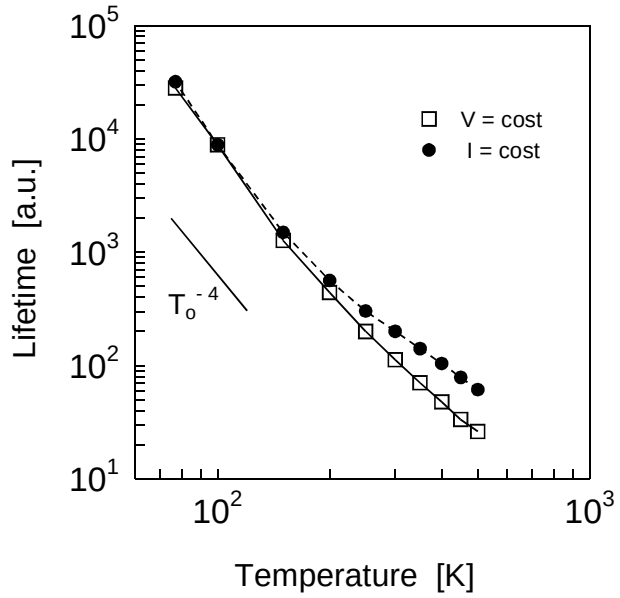

Figure 2.11. *Film lifetime as a function of the substrate temperature. Constant voltage (open squares) and constant current (filled circles) operation modes are compared. The data refer to an average over 50 samples with sizes of 100x100.*

In order to illustrate the power dissipation characteristics of the process during the degradation the average temperature of the sample can be calculated using the following formula:

$$\langle T \rangle_{N_{tot}} = \frac{1}{N_{tot}} \sum_k T_k = \frac{1}{N_{tot}} \sum_k (T_0 + \Delta T_k) = T_0 + \frac{A}{N_{tot}} \sum_k r_k i_k^2 = T_0 + \frac{A}{N_{tot}} RI^2 \qquad (2.8)$$

Figure 2.12 plots this as a function of the resistance that can be considered as an indicator of the degradation process.

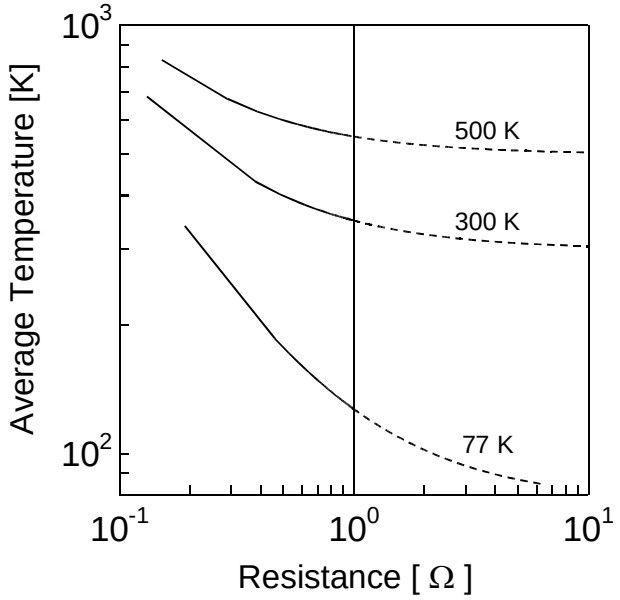

Figure 2.12. *Average temperature of a 100x100 network in constant voltage operation mode as a function of the sample resistance. The left part (continuous curve) below 1Ω corresponds to the conductor-superconductor transition, the conductor-insulator transition is shown by dashed line.*

2.2.5 Power spectral density of the resistance fluctuations

In the search of another indicator for the actual state and predictor of failure one can consider the power spectral density of the total resistance fluctuations that can give more information than taking only the variance. The PSD typically has 1/f frequency dependence in such samples as a superposition of the elementary fluctuations. A typical way to construct 1/f noise is to assume superimposition of elementary resistance fluctuations in the form of

$$S_{rk}(f) = \frac{\rho^2 \tau_k}{1+(2\pi\tau_k f)^2} \tag{2.9}$$

where τ_k is the correlation time of the fluctuation [30]. In our simulations we have used hyperbolically distributed τ_k values in the range of 10^{-6}s to 1s to provide 1/f noise over a frequency range of 6 orders of magnitude and these fluctuations are randomly assigned to the resistors. Thus the power spectral density of the total resistance fluctuations can be expressed as [15,16]

$$S_{\delta R}(f) = \frac{R^2}{r^2\left(\sum_k i_k^2\right)^2}\sum_k S_{rk} i_k^4 \,. \tag{2.10}$$

Note that one can expect a change in the shape of the power spectral density if the damage pattern is getting inhomogeneous since the individual fluctuations are weighted by the 4th power of the local current.

This is evidenced on Figure 2.13. Here four different degradation states are shown both for the free and biased percolation processes. While no significant change in the PSD frequency dependence can be observed for the free percolation, biased percolation can exhibit noticeable changes.

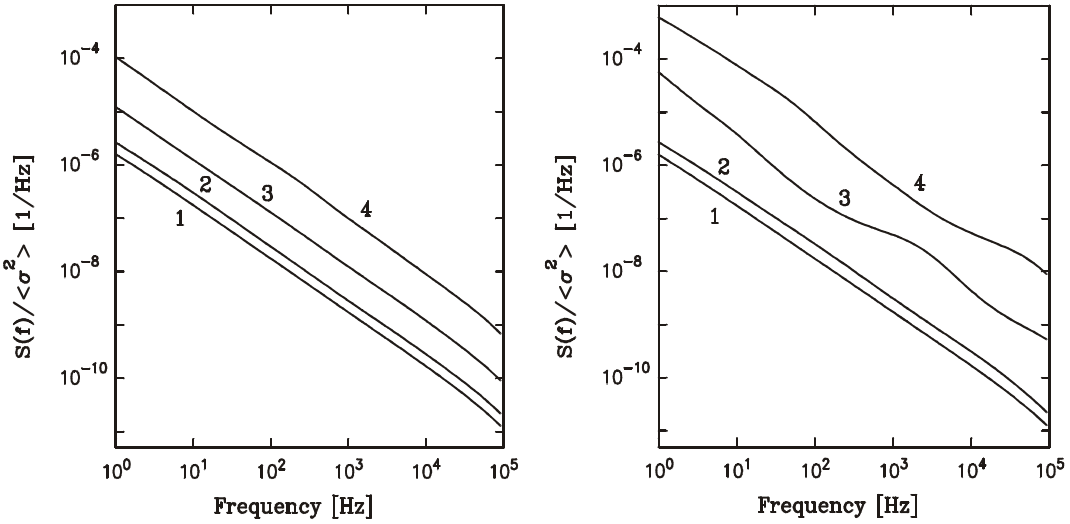

Figure 2.13. *Normalized spectral density of total resistance fluctuations at different values of the resistance for the free (left panel) and biased (right panel) percolation model for a lattice with size of 100x100. Numbers label the state corresponding to different sample resistance values: free percolation: (1) R=1.0 Ω, (2) R=1.2 Ω, (3) R=2.0 Ω, (4) R=4.1 Ω. biased percolation: (1) R=1.0 Ω, (2) R=1.2 Ω, (3) R=2.0 Ω, (4) R=4.3 Ω.*

2.3 Conclusions

We have introduced a biased percolation model suited to investigating degradation and abrupt failure of electronic devices. A software framework has been developed to numerically simulate the 2D resistor network model of a thin conducting film. As indicators of degradation, we have studied the evolution of the damage-pattern, resistance evolution, current and temperature distributions, the relative resistance fluctuations and their frequency dependence. A comparative analysis with the free percolation model shows interesting features.

- The damage pattern exhibits an anisotropic distribution of defects perpendicular (conductor-insulator transition) or parallel (conductor-superconductor transition) to the direction of the current flow which exhibits a characteristic filamentary damage pattern.
- The resistance and relative variance both exhibit a fast and sharp transition to failure with decreasing temperature, the former showing a progressive decrease and the latter an increase.
- The fraction of defects responsible for the failure is much smaller than that expected from standard percolation.
- By associating a time scale with the iteration steps, the lifetime of the device has been found to decrease radically with temperature.
- The variance of resistance fluctuations scales with the resistance with a scaling exponent of γ=2.05±0.08.
- Pure 1/f noise spectra exhibit an increase in amplitude and a colored transition near the abrupt failure of the device.

- The model can be extended to consider different reasons of defect generation by replacing the thermally activated degradation process. The local current dependence must be kept in order to have similar damage pattern, conductivity and noise evolution.

Finally, we note that the above features are in satisfactory agreement with existing experiments [2-13], indicating that this kind of model can offer interesting possibilities to study reliability and failure of electronic devices. The strong increase of the noise during degradation indicates the relevance of the use of the noise as a sensitive and non-destructive diagnostic tool of device degradation.

3 DSP data acquisition and control system for noise analysis

There are many accurate, fully featured professional instruments on the market that can be used to support special scientific experimentation, signal and system analysis. Noise measurements usually require low-noise preamplifiers, spectrum analyzers and special low-noise power supplies. Some manufacturers [1] are specialized to develop such devices and today there is rapidly improving alternative of modular computer controlled data acquisition systems and software support from companies like National Instruments [2] that might help scientists and engineers to develop their specialized, optimized experimental solution quickly and efficiently.

These solutions still may have several limitations because of high cost, they can be too bulky, in many cases the lack of galvanic isolation and differential input/output structure limit the performance and application possibilities while the required reliability and accuracy can be satisfied with custom solutions. Although building custom solutions need considerable expertise, the availability of high performance components and building blocks and the excellent technical documentation and tools eases the development of highly efficient experimental systems. Another significant advantage of the approach is the possibility of easy deployment. Keeping these in mind we have developed a special modular DSP-based data acquisition and control system in 1999 that allowed us to perform many scientific measurements and experiments not only in noise research ($1/f^{\alpha}$ noise generation [A1], analog computer experiments of stochastic resonance [D8], fluctuation enhanced gas sensing [E3-E6] and absolutely secure communications using analog electronic components [F1-F3]; see the next chapters), but in many other multidisciplinary research and engineering fields including laser physics and photoacoustics [G9], lock-in amplifier applications, nanotechnology related measurements [E3-E6], atomic force microscope optimization and research of experimental education based on virtual instrumentation [C7]. We have made more than ten units that are used in many research laboratories at the University of Szeged, however some are installed in foreign research institutes (Texas A&M University, Department of Electrical and Computer Engineering; Rice University, Department of Mechanical Engineering & Materials Science; University of California Santa Barbara, Neuroscience Research Institute, USA; Fachhochschule, Emden, Germany).

Note that many of the above mentioned reasons still hold and the development of customized scientific instruments are continued at our research laboratory with a widened scope including medical and biophysics applications and we always tend to use the latest, highest performing components from leading suppliers like Analog Devices, Linear Technology, Texas Instruments [3-10].

In the following we briefly introduce the DSP-based system and the mixed signal modules that were used to achieve the results that will be detailed in the following three chapters.

3.1 DSP module

The modular system follows the Eurocard standard (IEEE Std 1101.11-1998). The individual modules can be plugged into a backplane with a 96-pin male DIN41612 connector. The backplane provides separate analog and digital grounds, 5V digital supply, low noise -5V, 5V, -15V and 15V analog supply. The backplane connects the

boards' signals including the 16-bit bidirectional data bus, 8-bit address bus, I/O control signals, reset, two high-speed DSP serial ports, an UART port and three interrupt lines.

A1	+15V	B1	+15V	C1	+15V
A2	+15V	B2	+15V	C2	-15V
A3	-15V	B3	-15V	C3	-15V
A4	+5V	B4	+5V	C4	+5V
A5	+5V	B5	+5V	C5	+5V
A6	-5V	B6	-5V	C6	-5V
A7	-5V	B7	-5V	C7	-5V
A8	AGND	B8	AGND	C8	AGND
A9	AGND	B9	AGND	C9	AGND
A10	AGND	B10	AGND	C10	AGND
A11	DGND	B11	DGND	C11	DGND
A12	DGND	B12	DGND	C12	DGND
A13	DGND	B13	DGND	C13	DGND
A14	UART Transmit	B14	DATA15	C14	DATA14
A15	UART Receive	B15	DATA13	C15	DATA12
A16	undefined	B16	DATA11	C16	DATA10
A17	undefined	B17	DATA9	C17	DATA8
A18	undefined	B18	DATA7	C18	DATA6
A19	RESET	B19	DATA5	C19	DATA4
A20	Interrupt IRQE (ADSP2181)	B20	DATA3	C20	DATA2
A21	Interrupt IRQ2 (ADSP2181)	B21	DATA1	C21	DATA0
A22	Interrupt IRQL0 (ADSP2181)	B22	ADDRESS7	C22	ADDRESS6
A23	I/O SELECT	B23	ADDRESS5	C23	ADDRESS4
A24	I/O WRITE	B24	ADDRESS3	C24	ADDRESS2
A25	I/O READ	B25	ADDRESS1	C25	ADDRESS0
A26	Serial data read DR0 (ADSP2181)	B26	undefined	C26	undefined
A27	Serial data transmit DT0 (ADSP2181)	B27	Transmit frame sync TFS0 (ADSP2181)	C27	Read frame sync RFS0 (ADSP2181)
A28	Serial data read DR0 (ADSP2181)	B28	Transmit frame sync TFS1 (ADSP2181)	C28	Serial clock SCLK0 (ADSP2181)
A29	Serial data transmit DT0 (ADSP2181)	B29	Serial clock SCLK1 (ADSP2181)	C29	Read frame sync RFS1 (ADSP2181)
A30	5V DIGITAL	B30	5V DIGITAL	C30	5V DIGITAL
A31	5V DIGITAL	B31	5V DIGITAL	C31	5V DIGITAL
A32	5V DIGITAL	B32	5V DIGITAL	C32	5V DIGITAL

Table 3.1. *Pin description of the 96-pin DIN41612 connector. The backplane provides the analog and digital supply, the ADSP2181 digital signal processor module drives the buffered address bus, reset and I/O control signals and receives the interrupt lines via Schmitt-triggers to improve noise immunity. The data bus is buffered and bidirectional, the ADSP2181 serial ports are connected directly to the connector.*

The DSP board is the main module (see Figure 3.1 and 3.2) that can be plugged in the backplane. The heart of this module is the ADSP2181 digital signal processor from Analog Devices. The DSP integrates 80kbytes of SRAM – note that the modified Harvard architecture allows to store data in the program memory as well – and all

instructions are executed in a single cycle. The non-pipelined architecture ensures predictable execution time in most cases without the use of any hardware generated synchronization signals that has advantages for example in data conversion applications.

We have used lower and higher speed grade versions of the 16-bit fixed point DSP, 24MHz and 40MHz, respectively. The DSP data and address bus is buffered with 74HCT245 bidirectional and 74HCT541 unidirectional drivers. Three interrupt lines of the DSP are also routed to the connector. The I/O control lines are generated by a programmable logic device (PLD), a GAL16V8D chip. Although the DSP's read and write I/O time can be programmed, the data hold and setup times are fixed, therefore to ensure reliable communication with the other modules' components (data converters, latches, etc) a state machine is programmed into the PLD that generates the proper timing for the I/O control signal based on the DSP clock. This is done by counting four periods of the system clock to hold the read and write signals active, while the original DSP I/O signal last seven clock periods. A boot EEPROM contains a simple monitor program that allows downloading any DSP code without reprogramming the EEPROM. This way in system programming is made simple.

One channel of a dual universal asynchronous receiver/transmitter (UART) integrated circuit (PC16552D) is used to communicate with the host computer. The RS323 and RS422/485 hardware are protected against electrostatic discharge (ESD) and are available with data rates up to 230kbit/s and 1,152MBit/s, respectively. Later we have also integrated a USB-UART interface using the reliable FT232R chip. Note that the host computer interface is galvanically isolated to avoid possible ground loops, power line interference and noise in sensitive applications. An LCD interface helps to display information during operation and eases implementation of standalone operation modes.

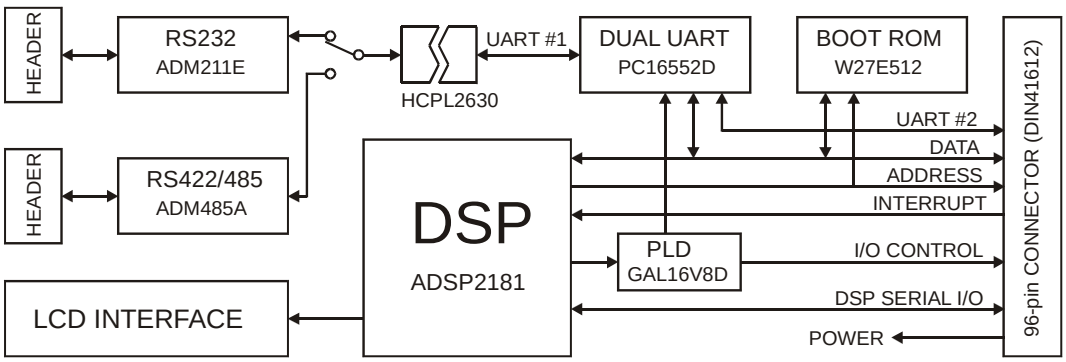

Figure 3.1. *Simplified block diagram of the main DSP module.*

We have used the easy algebraic assembly language of the ADSP21xx family of digital signal processors to develop software for the DSP module. Note that in most cases the DSP was used to acquire and generate data with precise timing and to perform simple signal processing like averaging, look-up table transformations, while the more complicated processing (like the spectral analysis, curve fitting, etc.) were done on the host computer. This way the software development could be kept rather simple and fast.

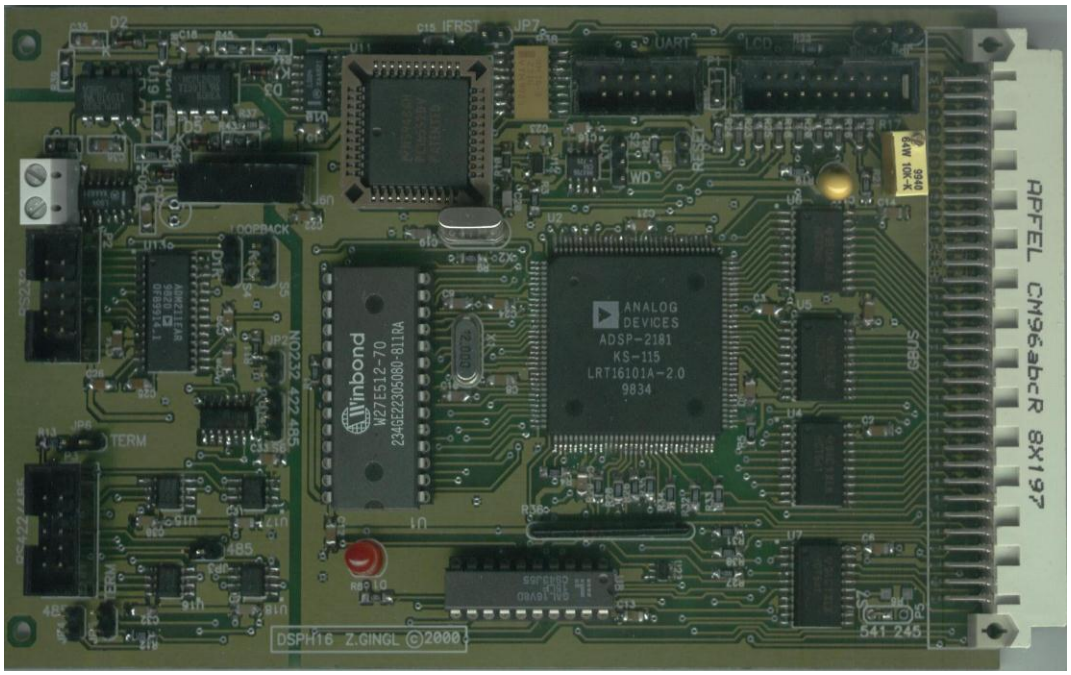

Figure 3.2. *Assembled printed circuit board of the DSP module.*

3.2 16-bit ADC, quad 14-bit DAC and dual 12-bit multiplier DAC module

Our experimental research of stochastic processes often needed the generation of multiple time dependent noisy and periodic waveforms with amplitude control, tuning of the system parameters by a few DC voltages, acquisition of noisy waveforms in a quite large dynamic range. We have designed and built a special Eurocard module to perform all of these functions. The block diagram and photo of the module are shown on Figure 3.3 and 3.4, respectively.

The DC voltages and/or the waveforms can be generated by a quad 14-bit D/A converter integrated circuit (AD7835). Although direct digital signal synthesis provides a way of amplitude control just by scaling the number to be sent to the D/A converter, the amplitude accuracy may be degraded, since for small signals only a fraction of the voltage range is used. To overcome this limitation we have used two 12-bit multiplying D/A converters (DAC1230) in two quadrant operating mode to precisely tune the amplitude of full-scale signals generated by external hardware or the other D/A converters integrated on the module. The signal to be scaled must be connected to the reference input of the multiplying DAC that has considerable input resistance, therefore the external signal is buffered by an operational amplifier. Another amplifier is used to convert the DAC output current into voltage. In order to reduce board complexity and provide good quality ground plane these multiplying DACs are driven by a small microcontroller (AT89C2051) that is connected to the DSP boards via an UART interface that uses only two wires.

The analog input signal conditioning consists of an input buffer amplifier and a second stage to convert the -10V to 10V input signal range into the ADC's input range of 0 to 2,5V. The 16-bit sigma-delta ADC (AD776) eliminates the need for complicated anti-aliasing filters. The ADC is connected to the DSP's serial communication port and

the ADC clock is also generated by the DSP. This ensures precise synchronization of all data conversion processes under the control of the DSP.

Note that the data converters are driven by a precision voltage reference circuit (AD780) to improve the reliability and accuracy of the system.

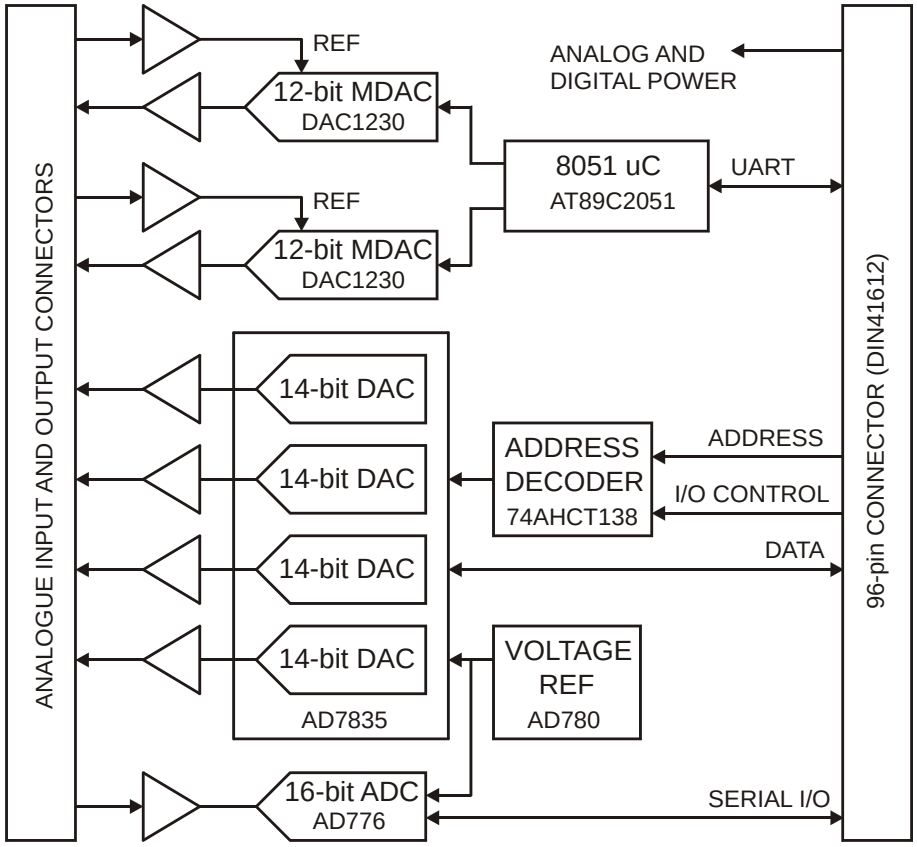

Figure 3.3. *Simplified block diagram of the data acquisition and control module.*

Electrical characteristics summary:
A/D conversion and analog inputs

- 100kHz maximum sample rate
- 16-bit resolution
- integral non-linearity: ±3LSB typical
- total harmonic distortion (THD): 90 dB typical

D/A conversion and analog outputs

- four independent channels with fixed ±10V range
- 14-bit resolution, 1LSB typical non-linearity
- 100KHz update rate
- 10us settling to 0.01%

Two quadrant multiplying D/A conversion I/O

- two independent channels with ±10V signal range
- 12-bit resolution, 1LSB typical non-linearity

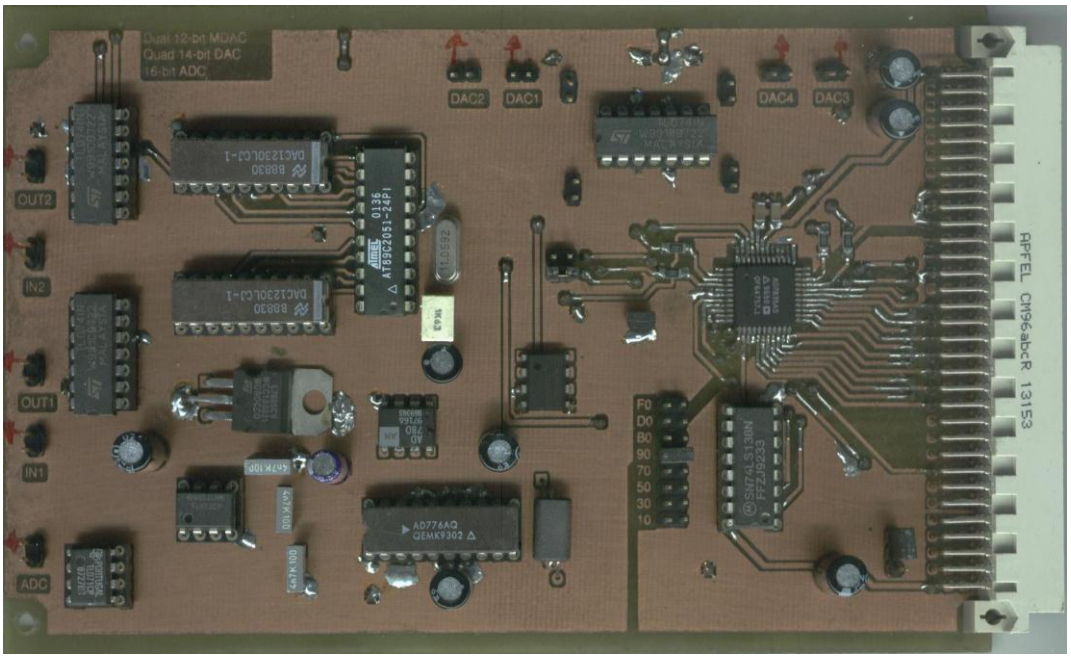

Figure 3.4. *Assembled printed circuit board of the of the data acquisition and control module.*

3.3 Quad 14-bit ADC and DAC module

In several applications it required to measure multiple time dependent voltage signals. There are two typical solutions to provide this: use of a single ADC and an analog multiplexer whose output can be switched quickly enough to realize a quasi simultaneous sampling. Signal source impedance, multiplexer settling time, sampling and conversion timing must be carefully considered and sigma-delta ADCs can't be used since their settling needs several conversion cycles. A better way is to use an ADC for each signal and use a single sampling clock for all ADCs. We have chosen this latter method to build a four channel analog input/output module based on a quad simultaneously sampling single-chip 14-bit ADC (AD7865). The four analog outputs were realized by a quad 14-bit DAC (AD7836). The block diagram and photo of the card can be seen on Figure 3.5 and 3.6, respectively.

Two ADC channels are connected to dual 4-to-1 fault-protected analog multiplexers (AGD439F) followed by an instrumentation amplifier (AD620) and a software programmable gain amplifier (PGA103). The inputs can be configured in single ended or differential modes by software. The two other ADC channels have simple unity gain voltage followers to eliminate the signal source loading by the ADC's input resistance.

The DSP provides the programmable sampling clock and the ADC's end of conversion signal is used to generate an interrupt after each conversion. The DSP's interrupt service routine can simply store the data into the memory or send it to the host but can even process the data and set the DAC outputs ensuring tight synchronization with the sampling process.

Electrical characteristics summary:
A/D conversion and analog inputs

- 8 differential or single ended inputs (software selectable)

- overvoltage protection for -35V..35V out of operating range
- software programmable gain/input range : ±0.1V, ±1V,±10V
- 2 auxiliary channels with fixed ±10V range
- approximately 1MHz bandwidth
- 350kHz maximum sample rate
- 14-bit resolution
- 10us settling time to 0.01%
- simultaneous sampling capability of 2 selected channels plus 2 auxiliary channels
- integral non-linearity: ±1LSB typical (60ppm)
- total harmonic distortion (THD): 90 dB typical (30ppm)
- external digital triggering, analog triggering based on converted input voltage
- external clock for conversion, software configurable polarity

D/A conversion and analog outputs

- four independent channels with fixed ±10V range
- 14-bit resolution, 1LSB typical non-linearity
- 100KHz update rate
- 10us settling to 0.01%

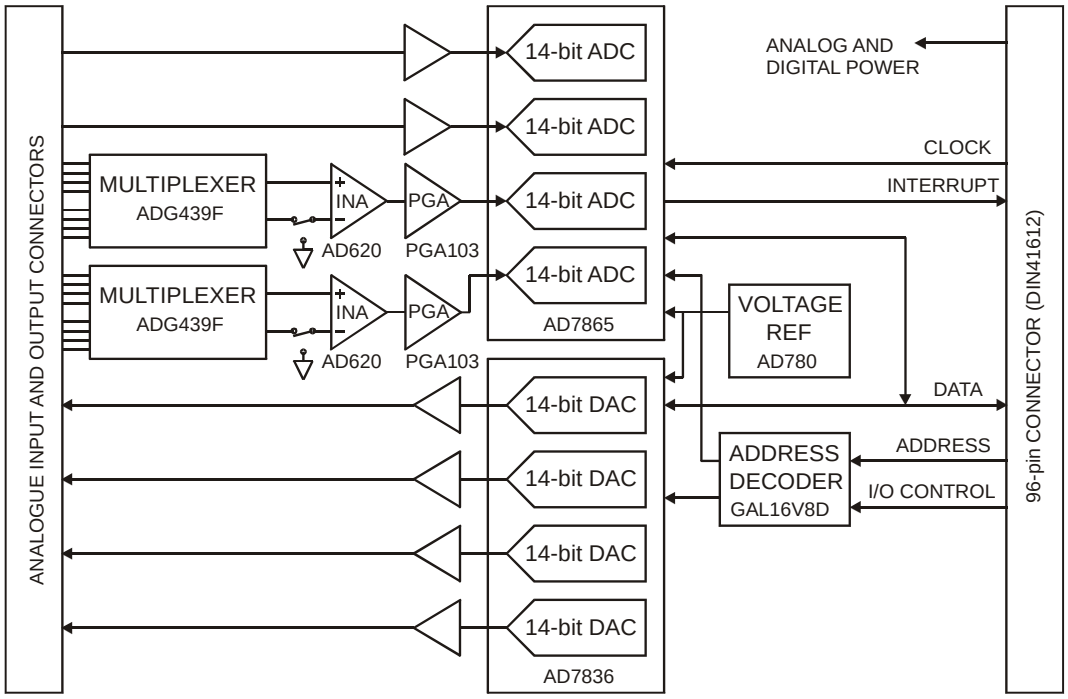

Figure 3.5. *Simplified block diagram of the 14-bit simultaneously sampling data acquisition and control module.*

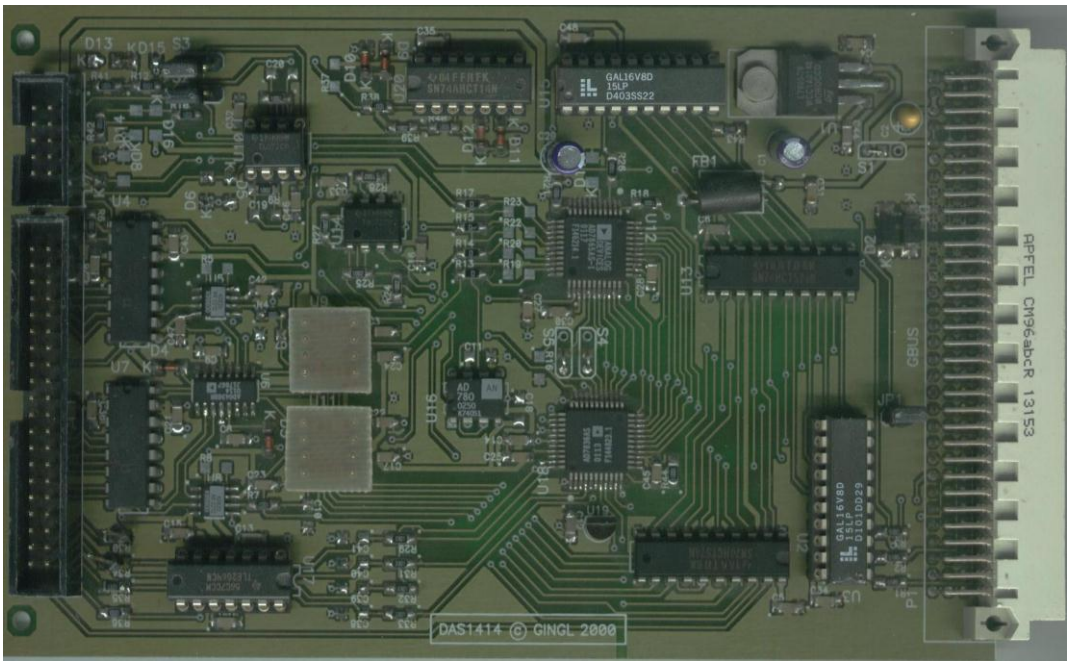

Figure 3.6. *Assembled printed circuit board of the 14-bit simultaneously sampling data acquisition and control module.*

3.4 Dual 16-bit oversampling ADC module

The last module that will be discussed is a high-speed and high-resolution two channel simultaneously sampling ADC card especially developed for recording noisy signals with wide amplitude and frequency range.

Figure 3.7 depicts the block diagram of the module and its photo can be seen on Figure 3.8. The unit incorporates two parallel output 16-bit sigma-delta ADCs (AD7723) whose sampling clock input is driven by the DSP. The maximum sample rate of the converters is 1MHz. The input signal chain contains a dual 4-to-1 fault-protected analog multiplexer (ADG439F) followed by two buffers (AD825). A high-speed fully differential amplifier (AD8132) drives the differential ADC inputs and does the required level shift also (note that the inputs are bipolar while the ADC is a single supply device).

Electrical characteristics summary:

- 8 differential or single ended inputs (software selectable)
- overvoltage protection for -35V..35V out of operating range
- approximately 400kHz maximum bandwidth
- 1MHz maximum sample rate, 16-bit resolution
- simultaneous sampling of 2 selected channels
- integral non-linearity: ±1LSB typical
- total harmonic distortion (THD): 90 dB typical
- software analog triggering based on converted input voltage

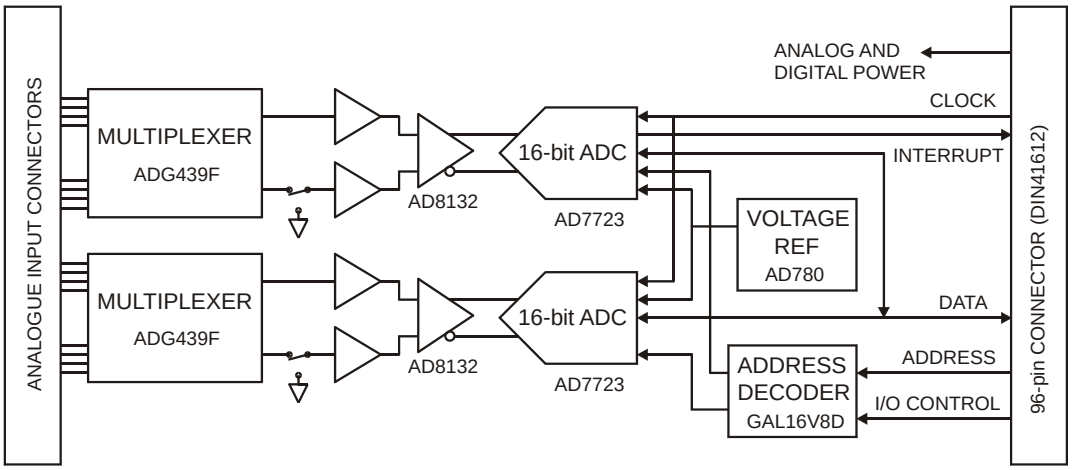

Figure 3.7. *Simplified block diagram of the dual 16-bit sigma-delta simultaneous data acquisition module.*

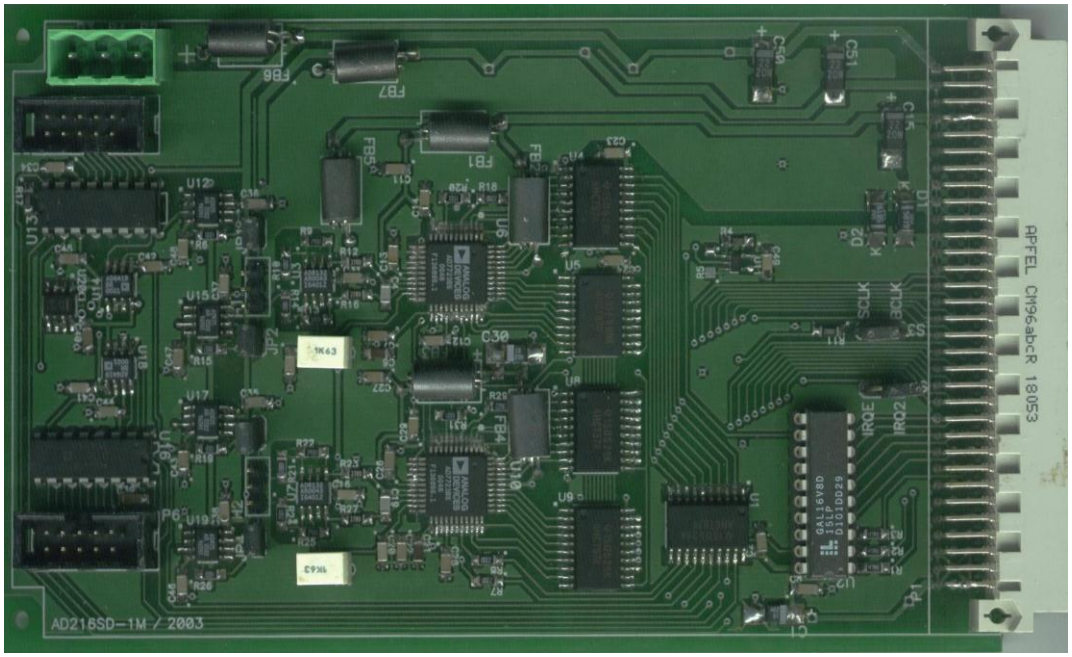

Figure 3.8. *Assembled printed circuit board of the dual 16-bit sigma-delta simultaneous data acquisition module.*

3.5 Conclusions

A highly flexible and high performance modular DSP controlled data acquisition and control system has been developed in order to effectively support precision experimentation in the field of noise research. The main unit is based on a 16-bit fixed-point DSP that allows real-time control and data acquisition with accurate timing and communication with a host computer via isolated serial interface and controls all other analog and digital modules in the system. The DSP is made in-system programmable to provide high flexibility.

Three high precision special data acquisition and control modules have been developed that were used in various research experiments that will be reported in the next chapters. Data conversion resolution up to 16 bits, simultaneously sampling

capability and high functional density along with the flexibility allowed performing high quality research in various fields. Several compact customized instruments have also been developed as an exploitation of the results obtained with the universal system as it will be shown later. The system has been successfully used in many multidisciplinary research projects, educational and engineering applications [A1,A2,C1-C7, D7,D8,D11,D19-D22,]. The system has been shown in an invited talk at HUNGELEKTRO 2002, 7th International Exhibition and Conference on Electronics Technology, Budapest, 23 April 2002 [C3].

4 High signal-to-noise ratio gain by stochastic resonance

4.1 Stochastic resonance

Surprisingly enough, in some non-linear systems a certain amount of random noise helps to optimize the signal transfer, in other words, to maximize the signal-to-noise ratio (SNR) at the output. This phenomenon is called stochastic resonance (SR), and it is one of the most exciting topics of noise research with several possible applications [1-12, D1-D5]. In addition to technical and physical systems, SR also occurs in biological systems, and is promising in neuron modeling based on noisy excitations [13-20].

The term stochastic resonance was introduced by Benzi and coworkers [1] when they wanted to find the mechanism behind the more or less periodic occurrence of ice ages. This period of 10^5 years matches the period of the eccentricity changes of the orbital of the Earth, therefore they assumed that the Sun's radiation power on the Earth's surface was also periodically changed. Since the effect is very small – only about 0,1% – the additional short-term climatic fluctuations were assumed to possibly trigger the occurrence of an ice age period. In other words, noise was considered to enhance the effect of a small periodic perturbation.

A simple way to show the concept of stochastic resonance is to consider a system that has a single tone periodic signal and Gaussian white noise as input signals and an output signal that is determined by some nonlinear transform of the inputs. Stochastic resonance occurs, if the output SNR has a maximum at nonzero input noise (see Figure 4.1).

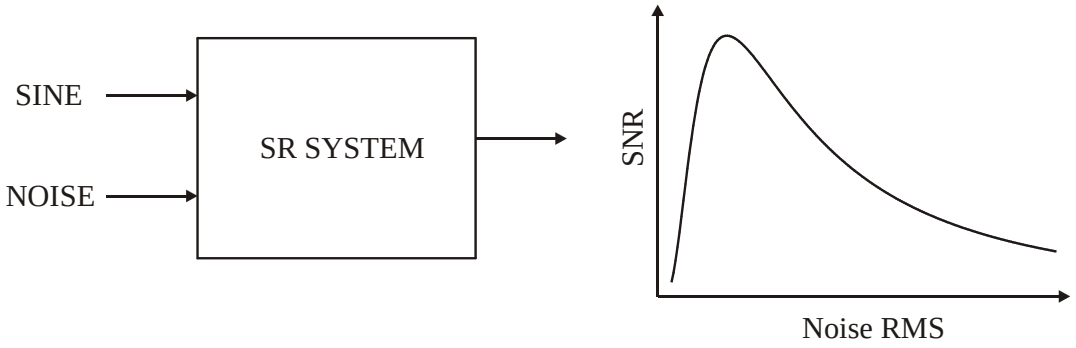

Figure 4.1. *System block diagram and SNR versus noise RMS*

In the field stochastic resonance the signal-to-noise ratio for the output signal is defined as [10]

$$SNR := \frac{\lim_{\Delta f \to 0} \int_{f_0-\Delta f}^{f_0+\Delta f} S(f)df}{S_N(f_0)}, \tag{4.1}$$

where $S(f)$ and $S_N(f)$ is the power spectral density of the output signal and background noise, respectively and f_0 is the frequency of the input periodic signal. Since the output signal is not purely periodic – although it has periodic components at the fundamental and even at higher harmonics – the power spectral density is continuous with Dirac-

delta peaks at f_0 and its multiples. The SNR definition tries to compare the strength of the signal to the background noise at f_0. However the periodic component's power is concentrated at while the noise power is distributed over a wide frequency range, this is the reason why this unusual definition is used. Note that its dimension is frequency (power divided by power spectral density) that may be quite odd from a technical point of view.

4.1.1 Stochastic resonance in dynamical systems

4.1.1.1 Double well potential

The so called double well system became the archetypal model for SR. In this case we assume that a particle is moving in a double well potential *V(x)* with two stable states [10]:

$$V(x) = -\frac{a}{2}x^2 + \frac{b}{4}x^4, \tag{4.2}$$

where x is the position of the particle, a and b are parameters. The potential has two minima at $-x_m$ and x_m and a barrier with height of ΔV between these two stable states, where

$$x_m = \sqrt{\frac{a}{b}}, \quad \Delta V = |V(0) - V(x_m)| = \frac{a^2}{4b} \tag{4.3}$$

If the particle is driven by a periodic force that is too weak to flip the particle between the two states and additional noise may help to do this. The periodic force can also be thought as a modulation of the potential as shown of Figure 4.2.

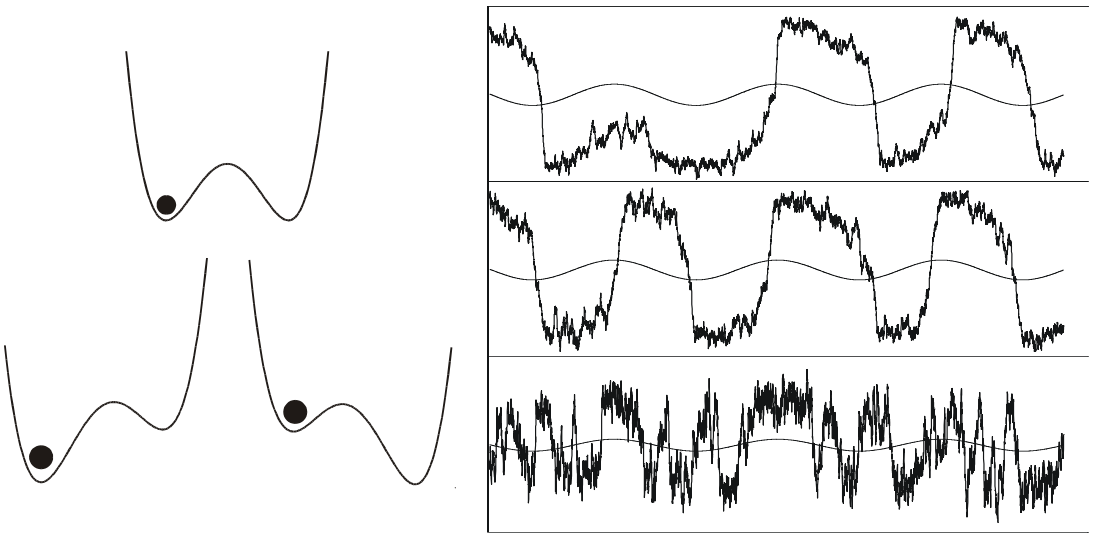

Figure 4.2. *Different states of the modulated double well potential are illustrated on the left. The right panel shows some typical particle position waveforms for too low, near optimal and too high noise from top to bottom, respectively.*

One can easily understand that some amount of noise can induce transitions between the two stable states at time instants synchronized to the period of the modulation. Too small noise won't force the transitions while too high noise makes the transitions randomly occurring. Therefore if the output signal is just the position of the particle, the SNR will have maximum at nonzero noise.

4.1.2 Non-dynamical stochastic resonance

Stochastic resonance can occur in even simpler systems. The first experimental system showing SR was a Schmitt-trigger [9], a bistable electronic circuit that was driven by a sub-threshold signal plus noise and behaves similarly to the double well system. The simplest stochastic resonator is a level crossing detector formed by a comparator followed by a monostable circuit as shown on Figure 4.3 [8,21,22]. Again we need a sub-threshold periodic signal plus noise to observe the phenomenon called non-dynamical stochastic resonance [D1].

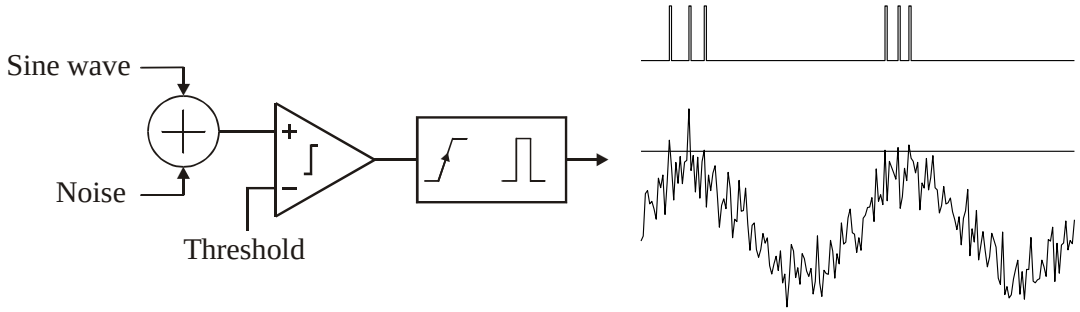

Figure 4.3. *A certain amount of noise optimizes the detection of a sub-threshold periodic signal fed into a level crossing detector. With too low or too high noise the output will have low signal-to-noise ratio.*

4.1.3 Dithering

Dithering that is used in many engineering applications and is similar to stochastic resonance [23]. Random dithering can be used to enhance the resolution of quantization; to improve linearity and spurious free dynamic range of analog-to-digital converters [24]; it is also used to improve the quality of digitized images. There are many similar applications where randomness is utilized to improve performance including stochastic time-to-digital conversion, pulse width modulation and many more.

Some modern high-speed analog-to-digital converters have on-chip random noise generator whose output is added to the input signal *before* digitization to improve the linearity of the converter. This clearly shows the fact that noise is not necessarily bad and adding noise can even have advantages in technical many applications. The LTC2208 (www.linear.com) and AD9268 (www.analog.com) analog-to-digital converters are good examples. Besides adding noise to the analog input, they employ a further optimization. A pseudorandom number generator followed by a digital-to-analog converter provides the analog noise source, and after the conversion the pseudorandom number is subtracted from the digital output. This way the noise injected by random dithering can be reduced. The block diagram of the solution is shown on Figure 4.4.

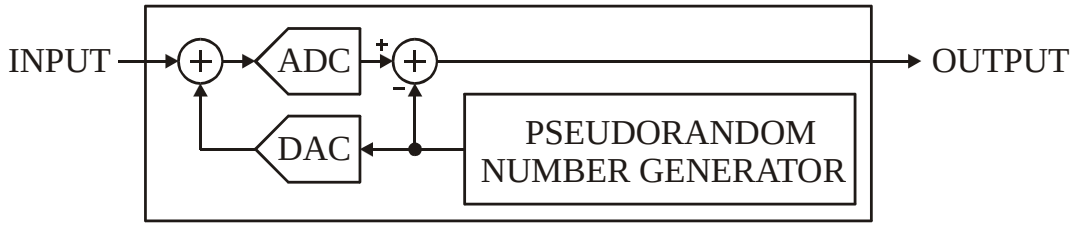

Figure 4.4. *The linearity of the AD9268 16-bit analog-to-digital converter is improved by the on-chip pseudorandom dither generator. The pseudorandom numbers are converted into an analog signal and added to the input. After the analog-to-digital conversion the number is subtracted from the output to reduce the noise introduced by the dithering.*

4.2 Signal-to-noise ratio gain

SR actually means that the output SNR (SNR_{out}) has a maximum as a function of the input noise intensity, but the input SNR (SNR_{in}) usually exceeds SNR_{out} for any noise amplitude. Researchers tried to find systems and conditions where SNR gain define as $G=SNR_{out}/SNR_{in}$, however in some promising cases it turned out that a measurement artifact caused by improper anti-alias filtering [25,26] and it was shown theoretically that SNR_{out} cannot be higher than SNR_{in} if the system works in the linear response regime [27]. The first successful attempt reported in 1995 by Kiss [28]: very large SNR gain has been found in a non-dynamical level-crossing SR system. Here the signal was a random pulse train therefore the classical SNR definition could not be used and the impact of the result remained relatively low. Later SNR gain exceeding unity was found in several systems including monostable and bistable, dynamical and non-dynamical systems. Our research group achieved significant results in the field that will be summarized in the following.

4.3 Signal-to-noise ratio gain in a level-crossing detector

4.3.1 Introduction

As it was mentioned above, it was shown that SNR gain above unity can be observed taking randomly repeating pulses as signal, but the conventional SNR definition given by Equation (4.1) can't be used since the signal is not periodic. Our aim was to show that it is possible to get very high gain even using periodic signals and the original SNR definition.

4.3.2 Signal-to-noise ratio gain improvement

We have developed a numerical simulation framework to carry out the investigations [D2]. The input signal was a periodic pulse train as shown on Figure 4.5.

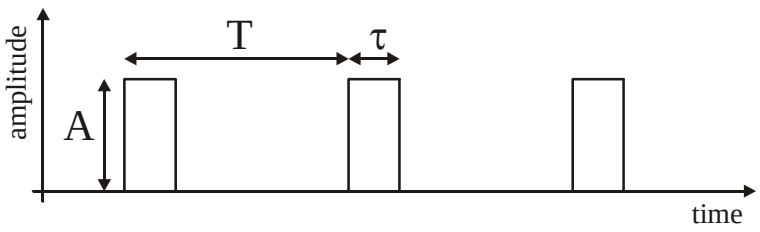

Figure 4.5. *Periodic pulse train with amplitude A and period T. The duty cycle is defined as τ/T, where τ is the width of the pulses.*

In our numerical simulations the amplitude of the signal was A=9, the duty cycle was varied between 1/128 and 1/2. The threshold was set to 10 and a Gaussian pseudo-random noise was generated and added to the signal. When the threshold was crossed, a pulse at the output was generated with the same width. The operation was not retriggerable to guarantee uniform pulse width at the output. The power spectral density was estimated using time series consisting of 16384 points with pulse width of 256 points. The PSD was calculated using an average of 10000 runs that allowed highly accurate calculation of the signal-to-noise ratio using

$$SNR = \frac{S_k}{\frac{1}{6}\sum_{j=1}^{3}\left(S_{k-j} + S_{k+j}\right)}, \tag{4.4}$$

where S is the discrete PSD, k is the index of the fundamental frequency.

Figure 4.6 shows how the signal-to-noise ratio gain depends on the input noise strength. For duty cycle of 1/2 no gain above unity is observed, but decreasing the duty cycle increases the gain, for 1/128 duty cycle it is well above 10^4.

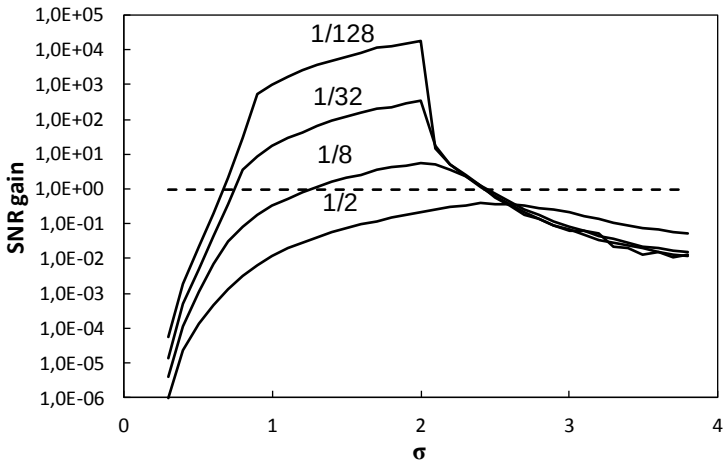

Figure 4.6. *Signal-to-noise ratio gain in a level-crossing detector obtained by numerical simulation. The gain can be very high, above 10^4, if the duty cycle (indicated above the individual curves) of the signal is low.*

4.4 Signal-to-noise ratio gain in non-dynamical bistable systems

Significant SNR gain can also be obtained in bistable systems as well. The first result demonstrating SNR gain exceeding unity was reported in 1997 [30]. The authors used the simplest bistable system, the Schmitt-trigger and a regular sub-threshold square wave input signal plus Gaussian noise for a single case. We have examined the possibilities of SNR improvement using pulse-like signals with different amplitude and duty cycle values [D7]. The symmetric periodic pulse train is depicted on Figure 4.7.

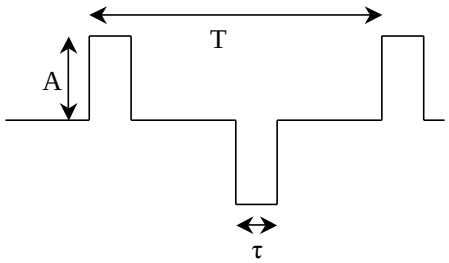

Figure 4.7. *The shape of the periodic input signal p(t): A is the amplitude expressed as a percentage of the threshold value, T stands for the period, τ denotes the width of the pulses and the duty cycle is defined as 2τ/T*

Since the commonly used SNR definition [10]

$$SNR := \frac{\lim\limits_{\Delta f \to 0} \int\limits_{f_0-\Delta f}^{f_0+\Delta f} S(f)df}{S_N(f_0)} \tag{4.5}$$

considers a single frequency only, there were many critical remarks in the literature using it for non-sinusoidal signals and also the presence of SNR gain was questioned and alternatives were provided [31-33,40,41]. We have introduced the wide band SNR definition to the field stochastic resonance that is commonly used in the field of engineering:

$$SNR_w := \frac{P_S}{P_N} = \frac{\sum\limits_{k=1}^{\infty} \lim\limits_{\Delta f \to 0} \int\limits_{kf_0-\Delta f}^{kf_0+\Delta f} S(f)df}{\int\limits_0^{\infty} S_N(f)df}. \tag{4.6}$$

This definition takes the total signal power and total noise power, and is commonly used in engineering. We have carried out numerical simulations and calculated the SNR gain using both definitions. To obtain the SNR gain as a function of the input noise amplitude σ, we recorded 1000 independent samples with lengths of 32768 data points for each σ value; the input pulse train was periodic by 1024 data points. Then we calculated the averaged PSD of these samples and from the PSD we obtained the signal-to noise ratio. The results are plotted on Figures 4.8 and 4.9.

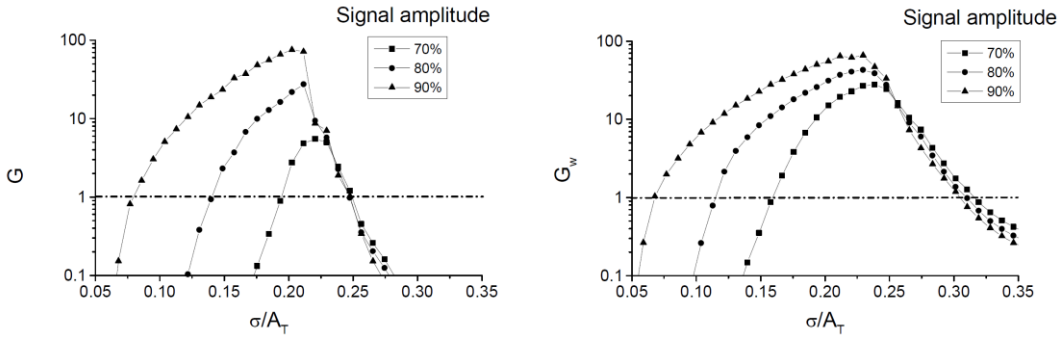

Figure 4.8. *Narrow-band (G) and wide-band (G_w) SNR gains in a Schmitt trigger as functions of input noise amplitude σ, for three different values of periodic signal amplitude. The latter is expressed as a percentage of the threshold value A_T, and σ is also scaled by A_T. The duty cycle is 10%.*

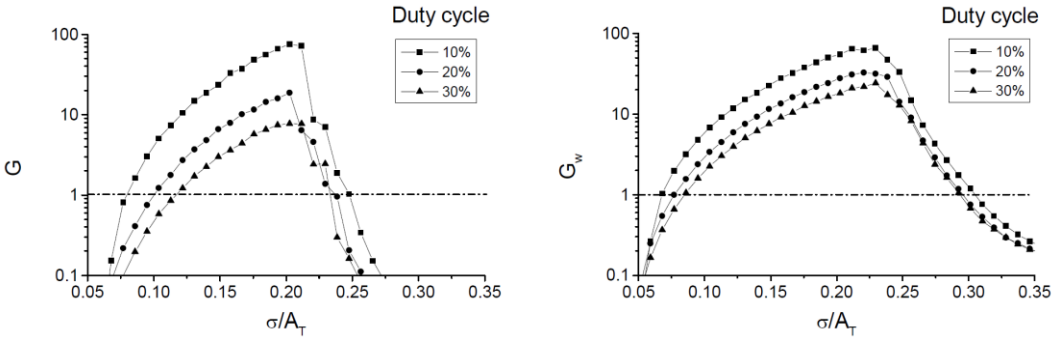

Figure 4.9. *Narrow-band (G) and wide-band (G_w) SNR gains in a Schmitt trigger as functions of input noise amplitude σ, for three different duty cycles. The amplitude of the noise is scaled by the threshold value A_T; the amplitude of the periodic signal is 90% of the threshold value*

4.5 Signal-to-noise ratio gain in the archetypal double well system

Although the double well system is similar to the bistable Schmitt-trigger, the mechanism is much more complex here and the SNR value can be very sensitive to the filtering and threshold crossing conditions. We have designed and built an analog computer to model the double well potential and used our special DSP data acquisition and control system to carry out the experiments and to get reliable, precise measurement results [D8-D12].

Using the potential [10]

$$V(x) = -\frac{a}{2}x^2 + \frac{b}{4}x^4, \tag{4.7}$$

we get the following equation for the motion of the particle:

$$m\ddot{x} = -\gamma\dot{x} - \frac{\partial V(x)}{\partial x} + p(t) + \xi(t) \tag{4.8}$$

where m is the mass of the particle, γ represents the friction, $p(t)$ and $\xi(t)$ is the periodic and white noise force, respectively.

With the substitutions

$$\frac{x}{x_m} \to x, \quad \frac{a}{\gamma} t \to t, \quad \frac{1}{a x_m} p\left(\frac{\gamma}{a} t\right) \to p(t), \quad \frac{\gamma}{a} f_0 \to f_0, \frac{1}{a x_m} \xi\left(\frac{\gamma}{a} t\right) \to w(t) \quad (4.9)$$

the following Langevin equation can be obtained for the overdamped situation:

$$\dot{x} = x - x^3 + p(t) + w(t) \quad (4.10)$$

This model can be used to analyze the SNR gain in the double well system. Figure 4.10 shows the block diagram of the corresponding analog computer and the DSP data acquisition and control system.

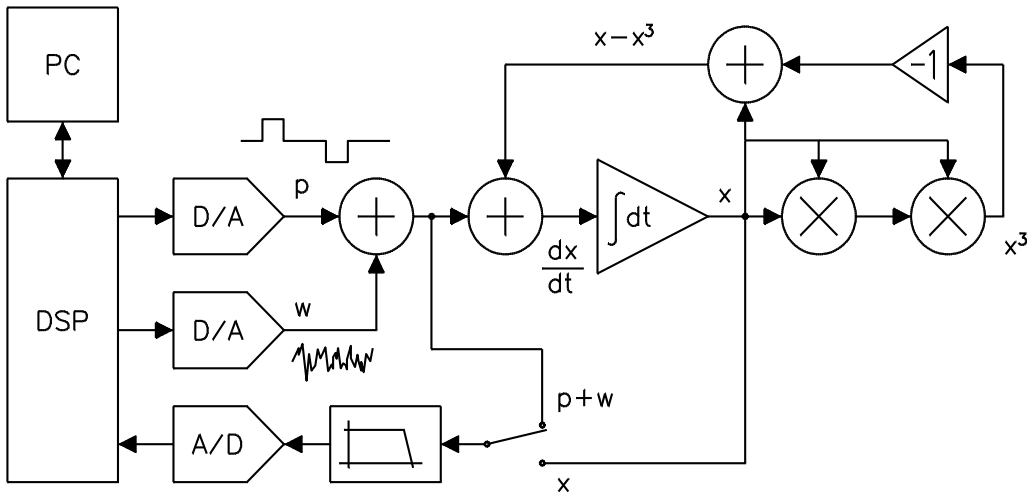

Figure 4.10. *Simplified block diagram of the mixed signal system.*

The DSP and data converter modules have already been shown in Chapter 3.1 and 3.2, respectively. The schematic of the analog computer is depicted on Figure 4.11. The AD734AN analog multipliers are chosen for their high accuracy and a dual precision operational amplifier has been used to provide the adder and integrator functions. The periodic and noise signals were generated by the DSP driving two DACs while the amplitude of these signal were precisely controlled by the data converter modules 12-bit multiplying DACs. The 16-bit sigma-delta ADC connected to the DSP's serial port ensured precisely coherent sampling that was important to achieve very highly accurate PSD estimation. The input and output signals were measured with exactly the same parameters to guarantee reliable SNR gain calculations.

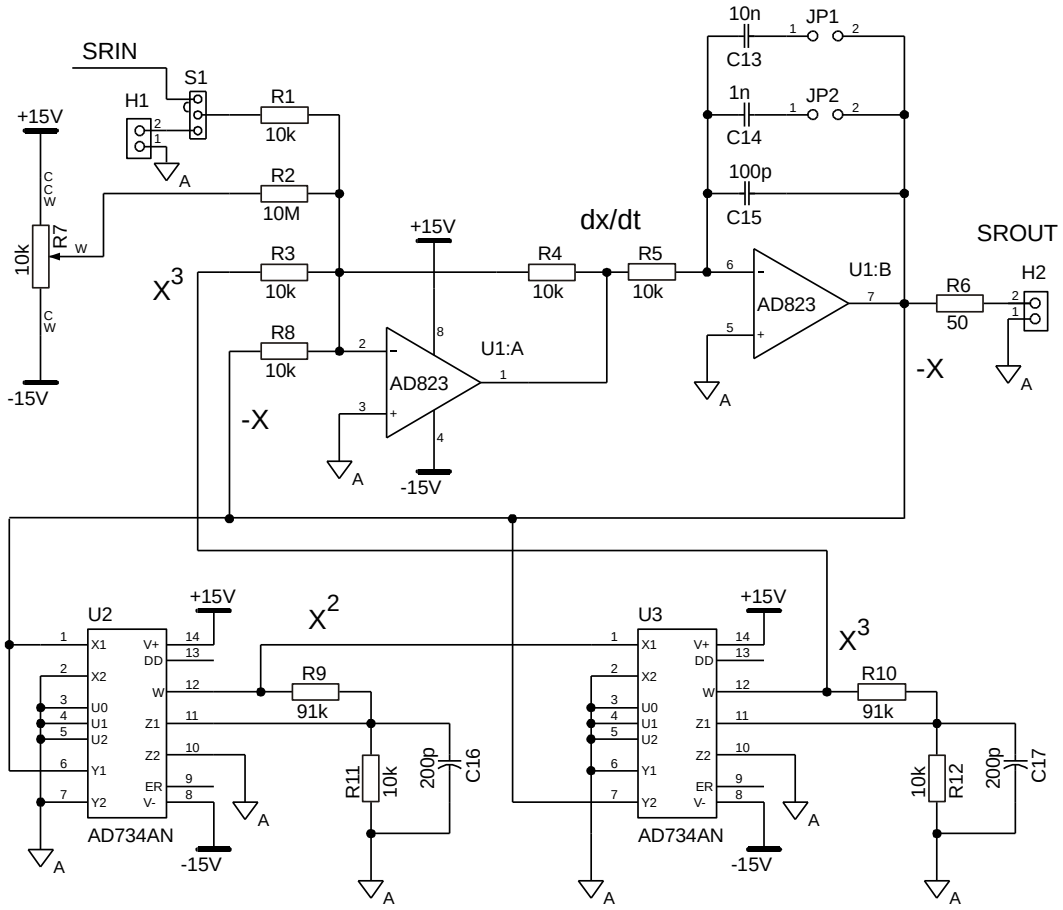

Figure 4.11. *Schematic diagram of the analog computer unit.*

We carried out measurements and calculated the input and output SNRs as well as SNR gains for three different values of the amplitude of the deterministic signal (70%, 80% and 90% of threshold value) with duty cycles of 10%, 20% and 30% for each amplitude value. A sample length of 2048 was used for recordings and 1000 samples were averaged to compute the power spectral density and the SNR. The sampling frequency was 8 kHz, the frequency of the periodic input signal was set to 31.25 Hz and the bandwidth of the white noise was 50 kHz.

We have found that the double well potential can provide high SNR amplification if the input excitation is a periodic pulse train plus Gaussian white noise. High SNR gains can be observed for small duty cycles and signal amplitude close to the switching threshold. It is important to emphasize that the SNR gain is greater than unity even over a wider range if we apply a much more realistic wideband SNR definition based on the total power of signal and noise.

Figure 4.12 shows the input and output SNR dependence for different signal amplitudes. One can see that while the input SNR is practically independent of the duty cycle, SNR drops at the output with decreasing amplitude resulting in a decreased gain.

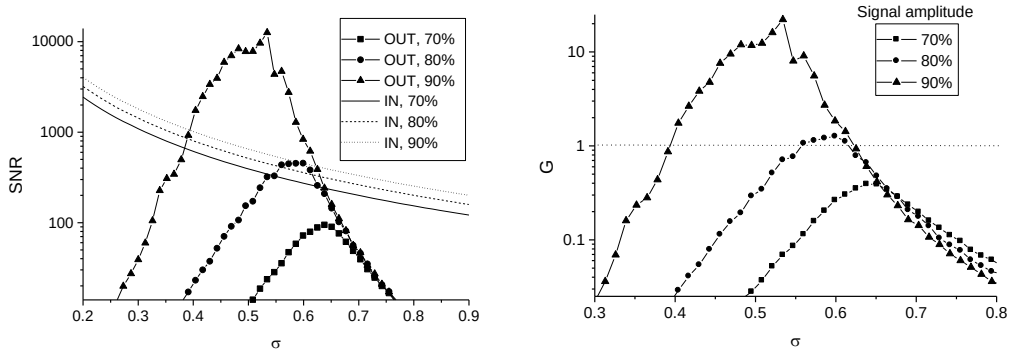

Figure 4.12. *Input and output SNR and SNR gain as a function of noise amplitude. The signal amplitude is 70%, 80% and 90% of the threshold value, the duty cycle is 10%.*

If the duty cycle is varied, the opposite effect can be observed: the output SNR remains practically unchanged, while the input SNR strongly drops if the duty cycle is decreased, see Figure 4.13.

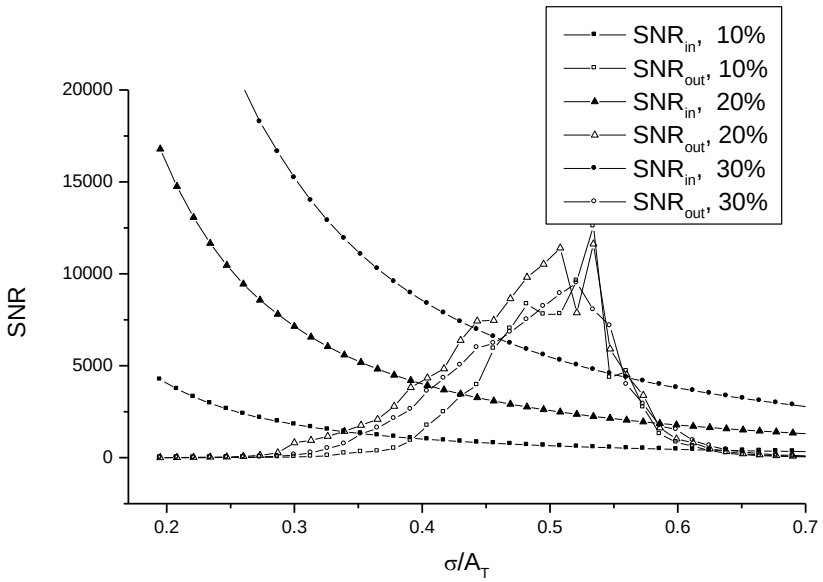

Figure 4.13. *Input and output SNRs as functions of input noise amplitude σ, for three different duty cycles. The amplitude of the noise is scaled by the threshold value A_T; the amplitude of the periodic signal is 90% of the threshold value.*

The SNR gain can for different duty cycles can be seen on the left of Figure 4.14; on the right the SNR gains obtained using the two different SNR definitions are compared.

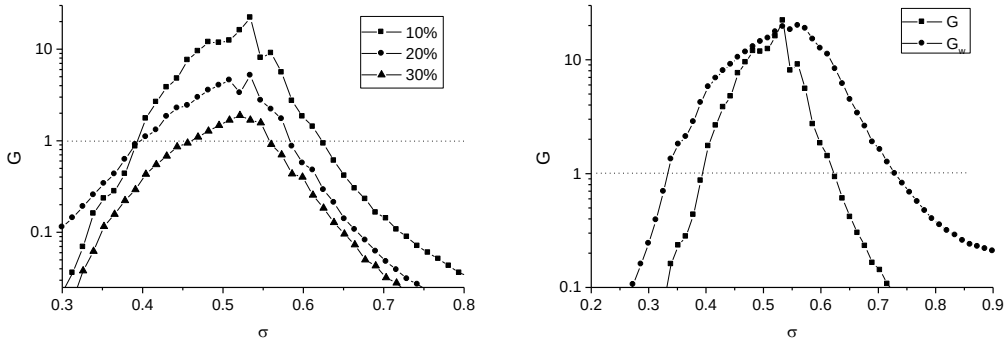

Figure 4.14. *The plot on the left shows SNR gain versus noise amplitude for different duty cycles. On the right panel the G and G_w plots are compared. The signal amplitude is 90% of the threshold value.*

4.6 Signal-to-noise ratio gain in stochastic resonators driven by colored noises

4.6.1 Can colored noise optimize stochastic resonance?

Most of the investigations have been carried out using wide band white noise excitations, however colored noises including 1/f noise are naturally present in real systems. This also holds for several biological systems – such as the neuronal system that is one of the most important application fields of SR – where $1/f^{\kappa}$ noises with $\kappa \approx 1$ are quite common. The effect of colored input noises in dynamical and non-dynamical systems was investigated earlier [10,D1] and it turned out, that colored noises usually result in poorer SNR. However it was reported that 1/f noise seems to be an optimal noise excitation and in a special case 1/f noise might optimize the sensory function of neurons according to the FitzHugh-Nagumo (FHN) model [37,38]. Exponentially correlated colored noise excitations were also analyzed in one of the most common dynamical SR model, the double well potential [10,34]. In order to understand the role of noise color better we have extended the investigations of SR in a double well and in the FHN neuron model to $1/f^{\kappa}$ noises with $0 \le \kappa \le 2$. The results for the two systems are compared [D13-D15].

We have already introduced the double well system above. The FHN dynamical model is based on the following differential equation system [37]:

$$\varepsilon \dot{v} = v(v-a)(1-v) - w + c + p(t) + \xi(t), \tag{4.11}$$

$$\dot{w} = v - w + b, \tag{4.12}$$

where we used parameters values of ε=0.005, a=0.5, b=0.15 and c=0.04 while $p(t)$ and $\xi(t)$ were the sinusoidal and noise terms. Our simulations based on the fourth-order Runge-Kutta method, the length of data sequences were 32768 and the SNR calculations were based on an average of 1000 spectra.

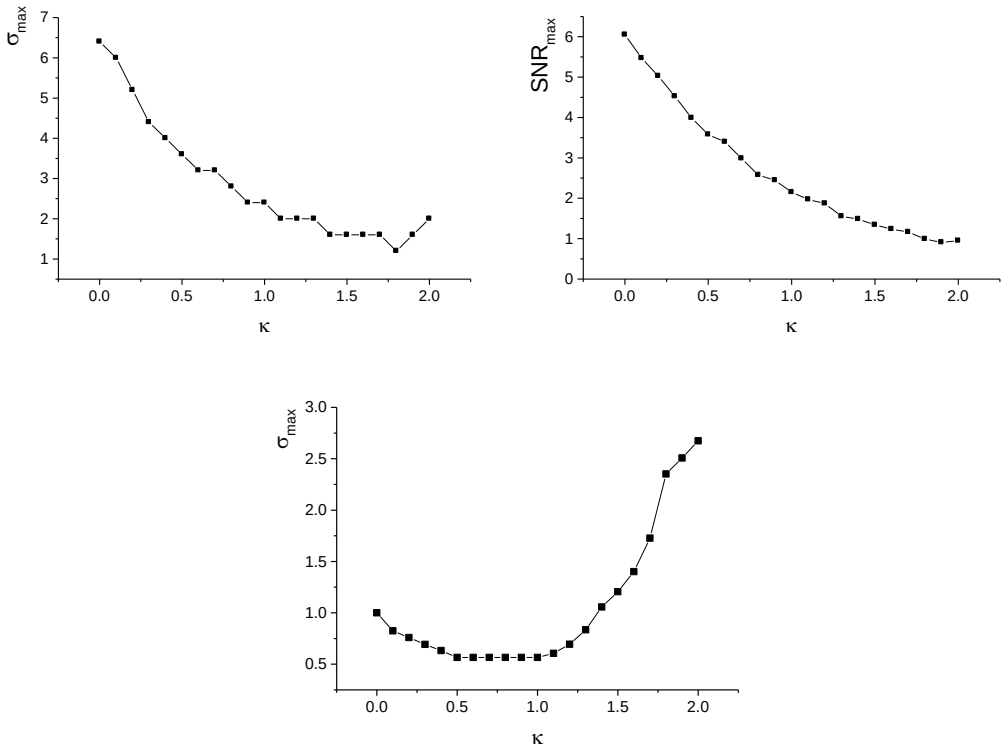

Figure 4.15. *Noise amplitude σ_{max} required to maximize SNR (top left), and the maximum value of SNR as a function of κ for the double well system (top right). The plot at the bottom shows σ_{max} for the FHN system.*

It turned out that smaller noise can indeed maximize the SNR for $\kappa>0$ than required by white noise ($\kappa=0$) for both systems, but the maximum SNR value is smaller for larger κ, the maximum SNR is occurs at white noise. The main difference between the two systems is that SNR versus κ does not exhibit a definite minimum for the double well system (see Figure 4.15). Previous results indicate that 1/f noise (κ =1) maximizes the SNR with smaller amplitude than required by white or $1/f^2$ noise [37-39], however our simulations with much higher resolution shows that the minimum does not occur necessarily at κ =1, although its practical relevance is questionable.

It seems to be clear that the reason for this kind of enhancement of SR is simply due to the filtering effect of these dynamical systems. This means that for example if the high frequency part of the noise is attenuated by the system, then larger amplitude is required for white noise to be effective. A band pass filtering character was found for the FHN model earlier [38,39] which gives a good explanation of the SNR dependence on the noise color. For the double well potential a low pass character is expected rather, which gives a reason, why the SNR behavior differs for the two systems. It is also clear, why the non-dynamical SR systems does not exhibit enhancement via noise coloring: filtering does not occur in most of such systems.

We can conclude that SNR enhancement strongly depends on the input noise bandwidth and 1/f noise probably does not play an emphasized role in SR in neural systems: one can easily find several other types of physically relevant noises (e.g. exponentially correlated noise) which are more efficient than 1/f noise.

4.6.2 Signal-to-noise ratio gain as a function of the noise color

We have also investigated the impact of the noise color on the SNR gain in the level crossing detector and in the Schmitt-trigger – two simple non-dynamical systems that can show SNR gain well above unity [D14].

We carried out each of our simulations with the following parameters: the input signals consisted of 32768 data points and the deterministic part was periodic by 2048 data points. The relative amplitude we chose as 90%, and the duty cycle was 10%. The frequency of the periodic input was chosen as 0.00375 Hz, which meant that the time increment between neighboring data points was 0.13 s. The maximum frequency in the noise was 3.84 Hz, 1024 times as much as the signal frequency. We varied the spectral exponent of the noise between 0 and 2, with an increment of 0.1.

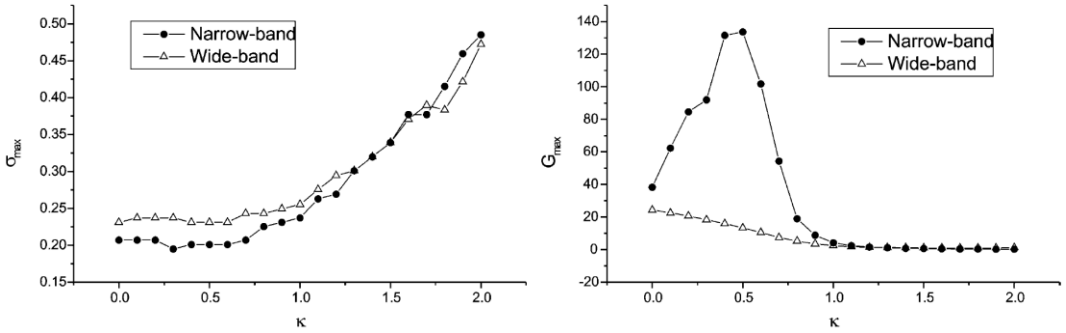

Figure 4.16. *Noise amplitude required to maximise the gain σ_{max} and the maximum of the gain G_{max} in an LCD, as functions of the spectral exponent of the noise κ. The narrow-band quantities are marked with solid dots and the wide-band ones are represented by hollow triangles*

Figure 4.16 shows that the maximum SNR gain occurs at nonzero κ. In order to make clear this clear, we show Makra's theoretical explanation [D14]. First we calculate the total power of the input noise using the following formula:

$$\sigma^2 = \int_{f_{\min}}^{f_{\max}} S_{noise,in}(f)df \,, \tag{4.13}$$

where we took f_{min} and f_{max} is the lower and upper frequency limit of the generated noise, respectively. Using this we can get the PSD for a $1/f^{\kappa}$ noises ($0 \le \kappa \le 2$, $\kappa \ne 1$)noise as

$$S_{noise,in}(f) = \sigma^2(\kappa - 1)\frac{(f_{\min} f_{\max})^{\kappa-1}}{f_{\max}^{\kappa-1} - f_{\min}^{\kappa-1}}\frac{1}{f^{\kappa}} \tag{4.14}$$

The input SNR is given as

$$SNR_{in} = \frac{S_{signal,in}(f_0)}{S_{noise,in}(f_0)} = SNR_{in}(f_0, \sigma, \kappa, f_{\min}, f_{\max}) \tag{4.15}$$

If we increase the spectral exponent, a greater portion of the same noise power will be concentrated in the domain of small frequencies, thus for a small f_0, SNR_{in} will decrease. Further increasing κ, the frequency domain wherein the noise is strongly attenuated might include f_0 as well, which means that the noise level around f_0 might drop as compared to that in the case of smaller spectral exponents, producing greater SNR_{in}. Thus the input SNR may have a definite minimum at non-zero κ. Combined with a monotonically decreasing SNR_{out}, this effect may result in the non-monotonic behavior of the gain maximum. Figure 4.17 illustrates the tendencies of the input SNR

(calculated from the theoretical formula) and the output SNR (obtained from simulations, as no analytical formulae for the output in the case of colored noises is available), and the resulting gain.

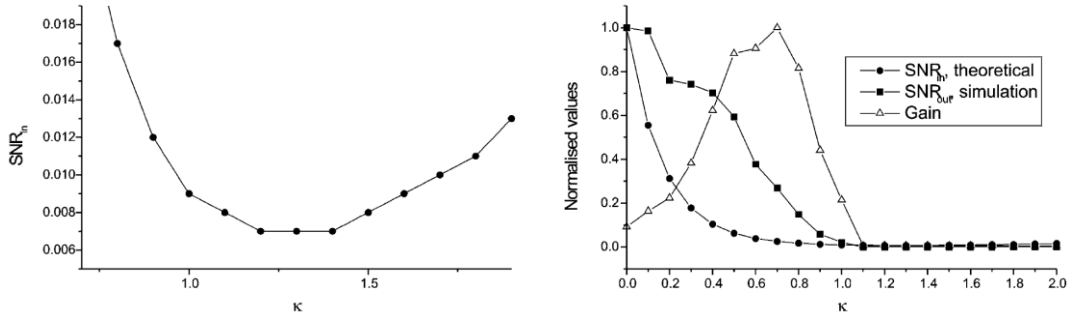

Figure 4.17. *The input SNR around the minimum, calculated from the analytical formula (left panel), and the output (simulated) and the input (calculated) SNRs compared at σ = 0.21, along with the resulting gain (right panel).*

The same parameters were used to analyze the SNR gain dependence in the bistable Schmitt-trigger system. The results of the simulation are shown on Figure 4.18.

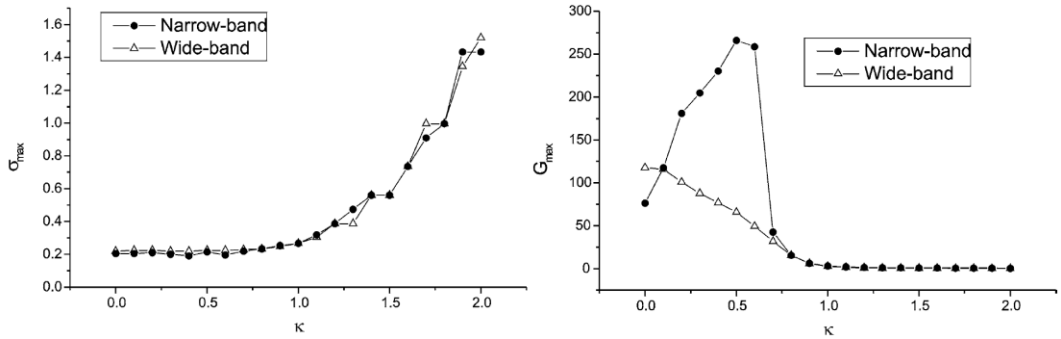

Figure 4.18. *Noise amplitude required to maximize the gain σ_{max} and the maximum of the gain G_{max} in a Schmitt-trigger, as functions of the spectral exponent of the noise κ. The narrow-band quantities are marked with solid dots and the wide-band ones are represented by hollow triangles.*

We can conclude that there is a marked difference in the behavior of the two types of gains. Regardless of what kind of gain we consider, we can predict that in both systems, increasing the spectral exponent (the correlation) of the noise is not desirable in the sense that the maximum of the gain will occur for greater noise amplitudes than for white noise. As for the value of the maximum itself, the two kinds of gains diverge: the wide-band gain is maximal for white noise and increasing the correlation only degrades it, while the narrow-band gain can be optimized at a non-zero spectral exponent.

4.7 Cross-spectral measurements of signal-to-noise ratio gain

Although the first significant SNR gain by stochastic resonance far above unity is demonstrated using a random pulse train as input signal, in most cases periodic signals were used in investigations. To show how robust is the SNR gain in the systems we have already considered, we have applied the SNR gain definition used by Kish [28,D16,D17]:

$$SNR_{CS} := \frac{P_S}{P_N} = \frac{\int_0^{\infty} \frac{\left|S_{in,out}(f)\right|^2}{S_{in,sig}(f)} df}{\int_0^{\infty} S_{out}(f) - \frac{\left|S_{in,out}(f)\right|^2}{S_{in,sig}(f)} df}. \tag{4.16}$$

where P_S and P_N are the total power of the signal and noise part at the output, respectively, $S_{in,\,out}(f)$ denotes the cross power spectral density of the input signal and the total output, while $S_{in,sig}(f)$ is the PSD of the input signal.

We have applied three different signals: periodic pulse train, aperiodic pulse train and band-limited white noise with periodic extension (see Figure 4.19) as input signals and Gaussian white noise for stochastic resonance.

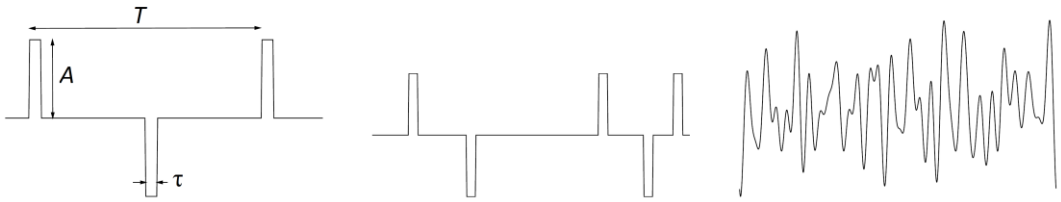

Figure 4.19. *Different input signals.*

The experiments were carried out with our analog computer built to model the double well potential and used our special DSP data acquisition and control system. Table 4.1 summarizes the most important parameters of the experiments.

	Periodic pulse train	Aperiodic pulse train	Noise
Sample length	8192		
Cycles per sample	32		n/a
Sampling frequency	10 kHz		
Pulse width	1.3 ms (13 data points)		n/a
Duty cycle	10%	n/a	
Bandwidth	n/a		39 Hz
Averages	10—50		

Table 4.1. *Analog simulation parameters for the different input signals*

The results show that SNR gain exceeding unity can be obtained for a quite general set of input signals; examples are shown on Figure 4.20 and 4.21. Note also that for periodic signals the cross-spectral SNR definition gives the same result as the wide-band SNR definition that emphasizes the reason to use of the latter instead of the narrow band formula.

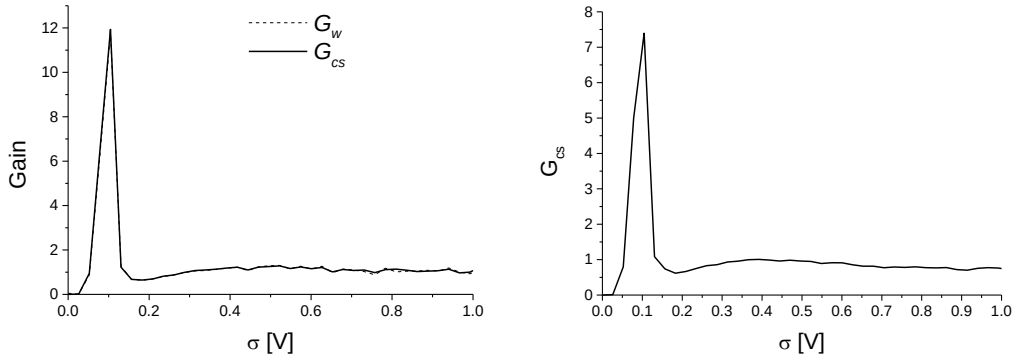

Figure 4.20. *SNR gain as a function of the input noise RMS. The left plot compares the wide-band and the cross-spectral SNR definition in the case of the periodic input pulse train and shows very close matching between the two quantities. On the right the cross-spectral SNR gain for the aperiodic pulse train is shown. The behavior is similar, although the maximum value is considerable lower.*

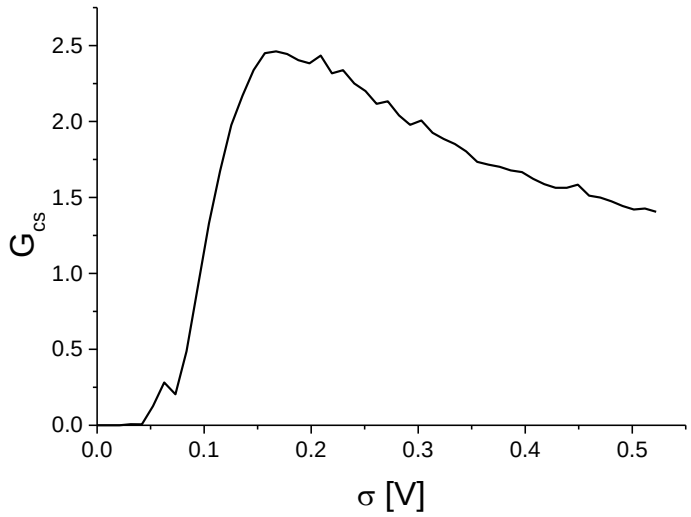

Figure 4.21. *Cross-spectral SNR gain as a function of the input noise RMS. The gain is above unity over a quite wide range of the input noise RMS.*

4.8 Hardware and embedded software development to support noise enhanced synchronization of excimer laser pulses

In this section we report about our hardware and software development aiming to improve the precision of the synchronization of excimer laser pulses. We utilized noise to enhance performance and we have also found a stochastic resonance related phenomenon in the behavior of control under certain conditions.

Precise time-synchronization of excitations, events is very important in experimental research in many disciplines including high-energy physics, photosynthesis research, chemical relaxation time measurements, technical applications of time-to-digital conversion and many more [42, 43].

In systems, where the trigger signal causes a delayed event at the output, regulation of the delay is required to maintain precise timing if the system's properties are time dependent, therefore the delay would change in time. A good example is the hydrogen thyratron that is widely used in excimer, carbon dioxide and copper vapor pulsed gas lasers, fast kickers in high-energy processes. In such applications it is important to keep the uncertainty and precision of synchronization below 1-2ns. The switching time – often called anode delay – of the thyratrons typically fall in the range of 100ps to 1ns, however this time is not constant. It has a slow, more or less deterministic, slowly varying component mainly due to temperature changes and an additive random jitter component associated by the gas discharge in the thyratron. Since the latter component is unpredictable, it cannot be compensated by active control; however the slow changes can be eliminated by inserting a tunable delay element between the start pulse and the input of the thyratron [D19].

In the following we present a brief overview of the regulation and show our improved solution to the problem for internally and externally triggered cases.

The principle of controlling the delay of the laser is illustrated on Figure 4.22. A programmable delay can be added to the laser delay to keep the time between the trigger and laser pulse at the desired value. The actual delay value must be measured in order to calculate the programmable delay value; note that the laser delay can be calculated as well, since the programmed delay is known. The time delays can be measured by various time-to-digital converters [44, 45], some of them are based on high speed counters running at a certain update rate [46].

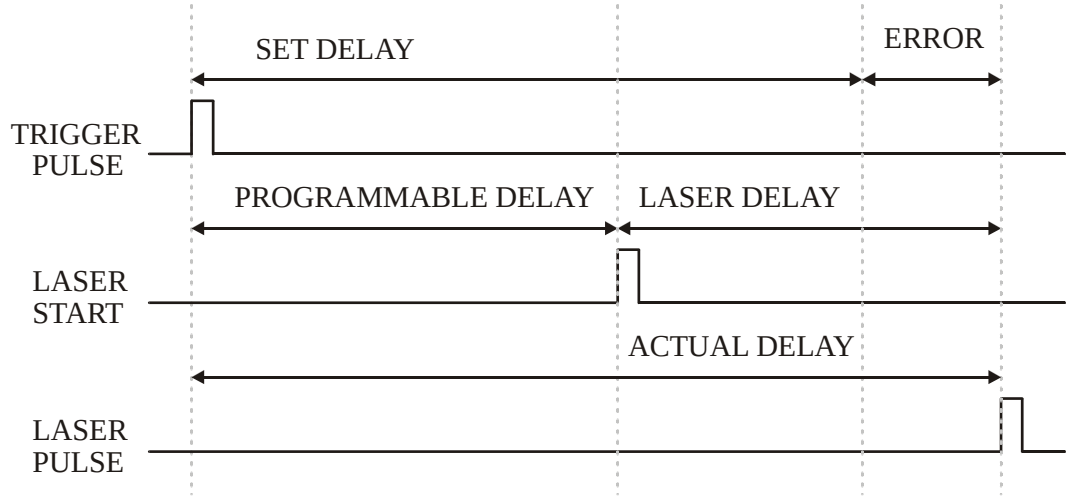

Figure 4.22. *The rising edge of the input pulse triggers a programmable delay element and this will start the laser. The delay of the whole system is the sum of the programmable delay and the laser inherent delay, thus the desired delay can be realized by compensating the varying delay of the laser.*

In our original design [D19] we have used integrated programmable delay lines to adjust the total delay of the system and a five-window digital window comparator to estimate the actual delay. The principle of detecting the time window in which the laser pulse appears is based on a software selectable reference delay signal that drives a 5-tap delay line integrated circuit (DS1100-30) whose four used outputs are equally spaced providing three 6ns wide neighboring time windows. Figure 4.23 shows the basic arrangement and the corresponding timing diagram.

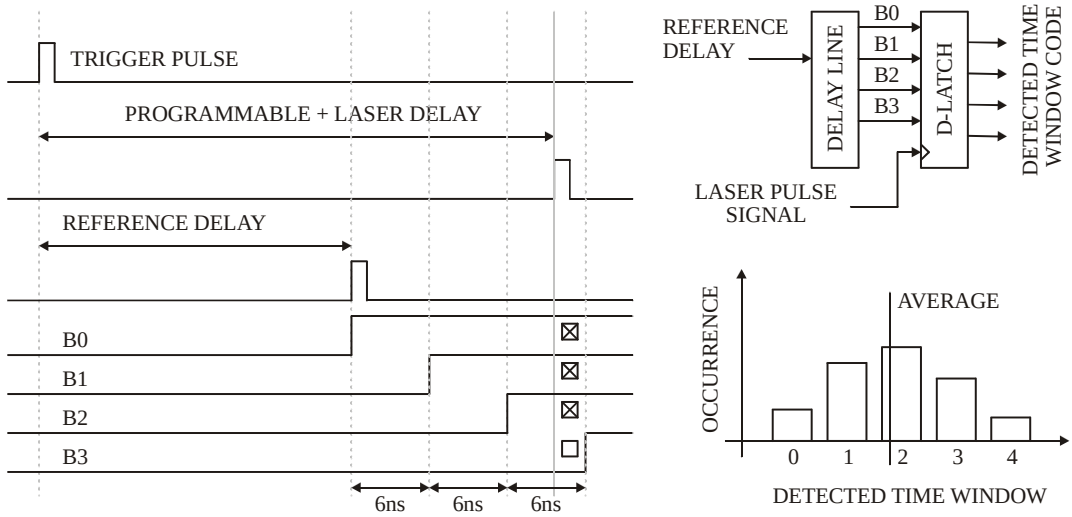

Figure 4.23. *The laser output signal can fall into five different time windows. The three windows in the middle have length of 6ns and are generated by a 5-tap delay line (DS1100-30) whose output signal can be captured by an edge-triggered D-type flip-flop upon the detection of the laser output pulse. For repetitive signals averaging can help to improve the time resolution if a certain amount of jitter noise is present.*

We have observed a stochastic resonance-like phenomenon here: the jitter noise of the system helped to improve the quality of the control, the RMS of the error of the delay had a minimum as a function of the strength of the laser jitter noise [D19], see Figure 4.24.

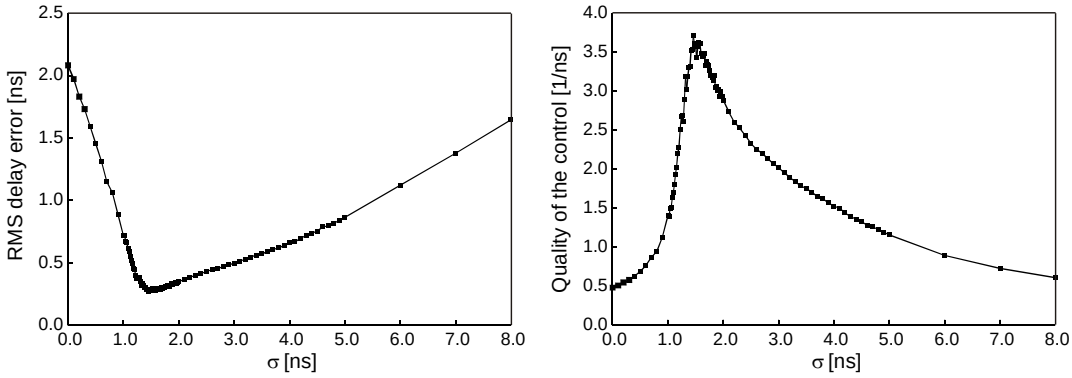

Figure 4.24. *The RMS delay error and its reciprocal, the quality of the control as a function of the standard deviation of the laser jitter noise (σ). The RMS error of the control has a minimum at non-zero jitter noise; in other words certain amount of noise is needed to optimize the quality of the control.*

The main drawback of the approach shown above is the seriously limited range of the time-to-digital conversion, while the absence of internal triggering and the limitations of the programmable delay circuits reduce the performance of the system considerably. In order to overcome these limitations we have designed a compact and flexible microcontroller based hardware to perform all measurement and control operations [D20]. A C8051F120 microcontroller has a built in programmable counter array (PCA) that consists of a 16-bit counter and six independent 16-bit compare/capture modules [47]. The main counter is running at 100MHz, and its actual value can be captured on the rising edge at the input of a module, therefore these modules can be used as time-to-digital converters with the resolution of 10ns, which is the system clock period. Note that this time base if significantly more accurate than the timing defined by the delay line used in the original design. The block diagram of the system is depicted on Figure 4.25.

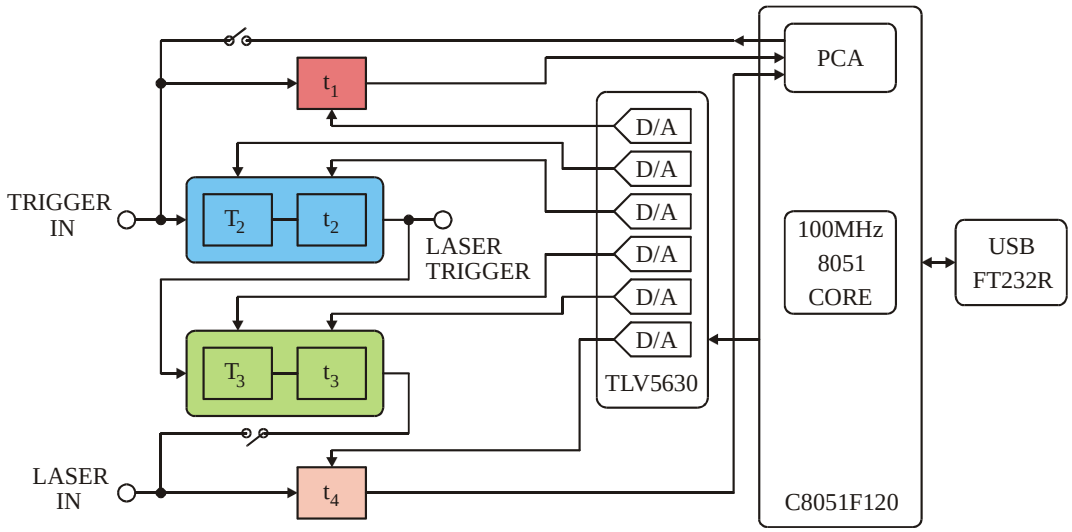

Figure 4.25. *Block diagram of the controller hardware. t_1, t_2,t_3 and t_4 are fine delay elements with range of 50ns, while T_2 and T_3 are coarse delay elements to allow delays of 2500ns. The additional timing and control is provided by the embedded microcontroller.*

The system contains four programmable delay units for different purposes:

- t_1 has a maximum range of 50ns, and it is used to add finely tuned delay for the start pulse before time-to-digital conversion by PCA module 1 (PCA1). It also allows random dithering to enhance resolution [48, 49].
- T_2 and t_2 are cascaded coarse and fine delay units with 2500ns and 50ns range to serve as a programmable delay to get the desired delay. These two units are required to have high enough resolution.
- T_3 and t_3 are cascaded coarse and fine delay units with 2500ns and 50ns range, and can be used to simulate the laser delay even without using the laser. They are useful to test and setup the unit or they can be used as general purpose delay elements.
- t_4 is a delay unit with range of 50ns and used to time shift the detection point of the laser pulse before time-to-digital conversion by PCA module 2 (PCA2). It can also be used to add random dither to enhance the resolution.

All of these programmable delay elements are based on a very simple principle [50]. The digital input signal is buffered and the output of this buffer charges a capacitor via a series resistor. The voltage U_c at the capacitor approximates the supply voltage U_s exponentially:

$$U_c = U_s \cdot \left(1 - e^{-\frac{t}{RC}}\right) \tag{4.17}$$

where R and C are the value of the resistor and the capacitor, respectively.

This voltage is fed into the non-inverting input of a high-speed comparator (ADCMP603), whose inverting input voltage is set by a digital-to-analog converter (TLV5630). The output of the comparator will be switched when the capacitor will be charged to a voltage equal to the voltage at the comparator's inverting input. This means that the output is delayed depending on the output voltage of the DAC U_{DAC}:

$$t = -RC \ln\left(1 - \frac{U_{DAC}}{U_s}\right) \tag{4.18}$$

Note that the buffer and comparator have their own additive delays of a few nanoseconds, marked with circled numbers 1 and 2 on Figure 4.26.

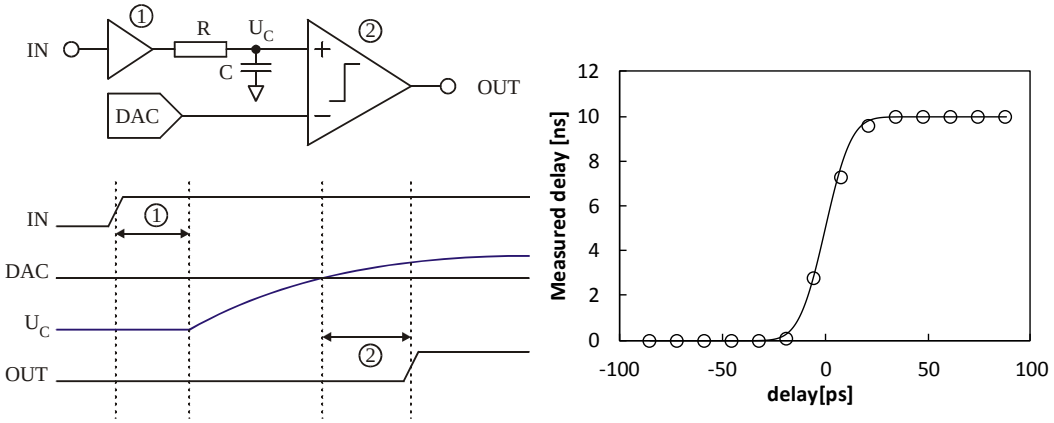

Figure 4.26. *Programmable delay generator. When the input signal goes from low to high state, the voltage U_c at the output approaches the supply voltage exponentially. The digital-to-analog converter (DAC) is used to set the comparator level, thus the outputs signal is delayed depending on this level. Note that the input buffer and the comparator both have their own delays of a few nanoseconds labeled by 1 and 2 in circles and marked in the time diagram by dashed lines. On the right hand side the measured delay is plotted as a function of the programmed delay. The delay has been measured by averaging the result of 1000 trials and the normal distribution curve was fitted to the data to obtain the 10ps RMS value of the jitter.*

The six delay elements are programmed with the TLV5630 single integrated circuit containing eight 12-bit DACs. The microcontroller can set all DAC output voltages and associated time delays via its SPI port and have a USB connection for optional supervised operation by a host computer.

The resolution of the 2500ns full scale range coarse delay units is 1ns with measured jitter of 90ps RMS, while the 50ns full scale range fine delay unit has resolution of 15ps and an impressively low 10ps RMS jitter. The transfer function and accuracy of the delay operation is shown on Figure 4.27.

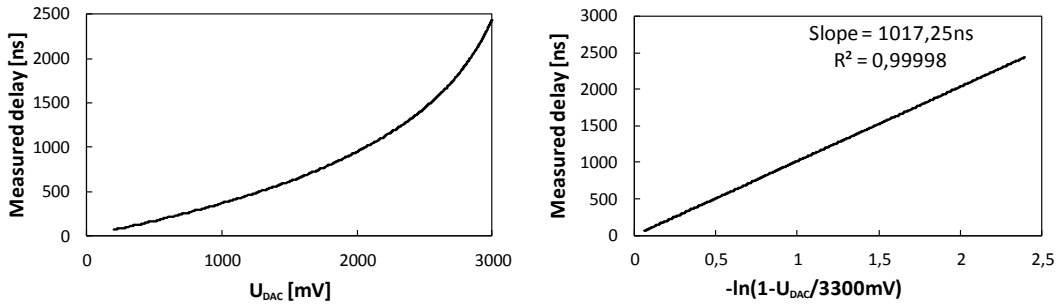

Figure 4.27. *Measured delay as a function of the U_{DAC} control voltage. On the right hand side the linearized function is plotted. The linear fit shows the rather high accuracy.*

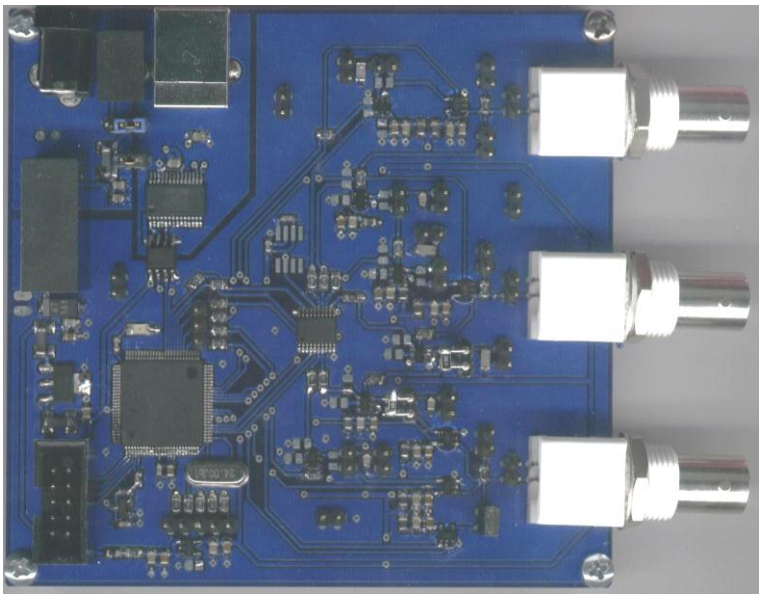

Figure 4.28. *Photo of the prototype printed circuit board.*

Figure 4.28 shows the photo of the realized circuit. The surface mount components are placed on the top side of the printed circuit board, the bottom side provides a high quality ground plane. The external signal can be connected via standard BNC connectors for this prototype, for embedded applications the design can be optimized.

4.8.1 Delay control operation

Two different triggering modes can be realized depending on the source of the start impulse that triggers the laser. If the system is controlled by an external device, the start signal will be asynchronous to the system clock of the controller hardware. The controller can also be used to start the laser and other external devices; in this case the trigger impulse is synchronized to the 100MHz system clock.

4.8.2 Internally triggered operation

As it was mentioned above, the laser can be triggered by the controller hardware, when the start pulse has a fixed delay from the preceding system clock toggle. The T_2+t_2 programmed delay and the laser delay are added to set the position of the laser pulse. The laser pulse triggers the t_4 delay element whose output will be captured by the PCA2 module. Figure 4.29 shows that this time instant can be synchronized to a system clock toggle point by tuning t_4. This means that the small jitter of the laser and the additional electronics will cause random flipping between two neighboring captured PCA2 values. This way the random jitter of the laser can be used to enhance the 10ns resolution by averaging the results obtained in a repetitive operation. It can also be desirable to add some jitter noise by setting t_4 randomly to optimize the effectiveness of the dither. Note that this delay does not affect the position of the laser output since it is only used to shift the counter capture signal. The desired delay is not limited to 10ns multiples, only the 15ps resolution of the fine delay unit limits the positioning.

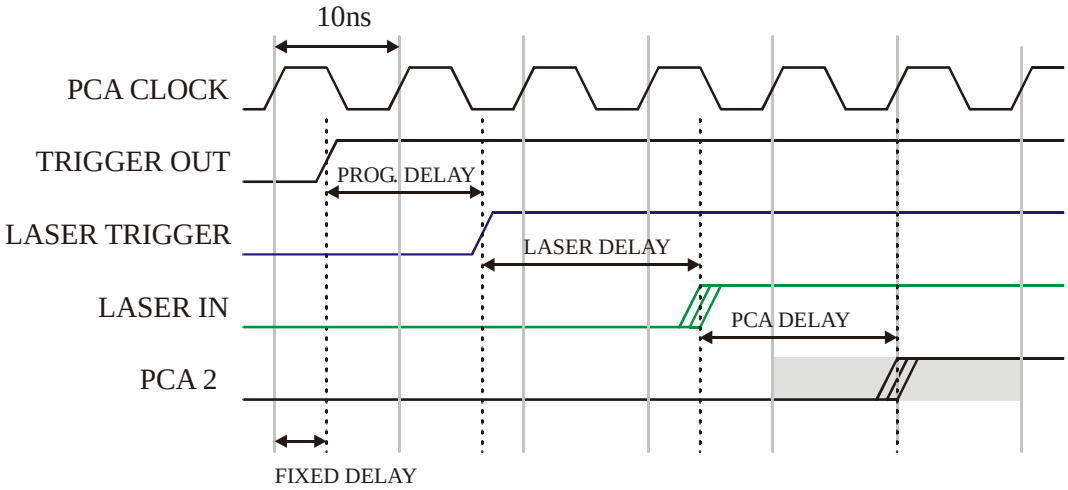

Figure 4.29. *Time diagram of the control signals. The trigger out signal is generated by the controller hardware, therefore it is locked to the system clock which has a period of 10ns. The PCA2 module is used to measure the resulting delay.*

4.8.3 Externally triggered operation

In many cases the laser start signal comes from an external device and must be synchronized to an external event. This means that neither the start pulse nor the laser output pulse is synchronous to the system clock. Therefore it is not any more possible to use the laser jitter alone as a dither signal to enhance resolution, since the capture signal cannot be moved to a system clock toggle point. In this case both the laser start signal and the laser output signal must be randomly dithered before time-to-digital conversion by PCA1 and PCA2 capture latches to allow resolution enhancement for repetitive operation. The uniformly distributed 10ns wide dither signal can be easily generated by programming the t_1 and t_4 delay elements with properly chosen pseudorandom numbers for the corresponding DACs. The time diagram of the signals is depicted on Figure 4.30.

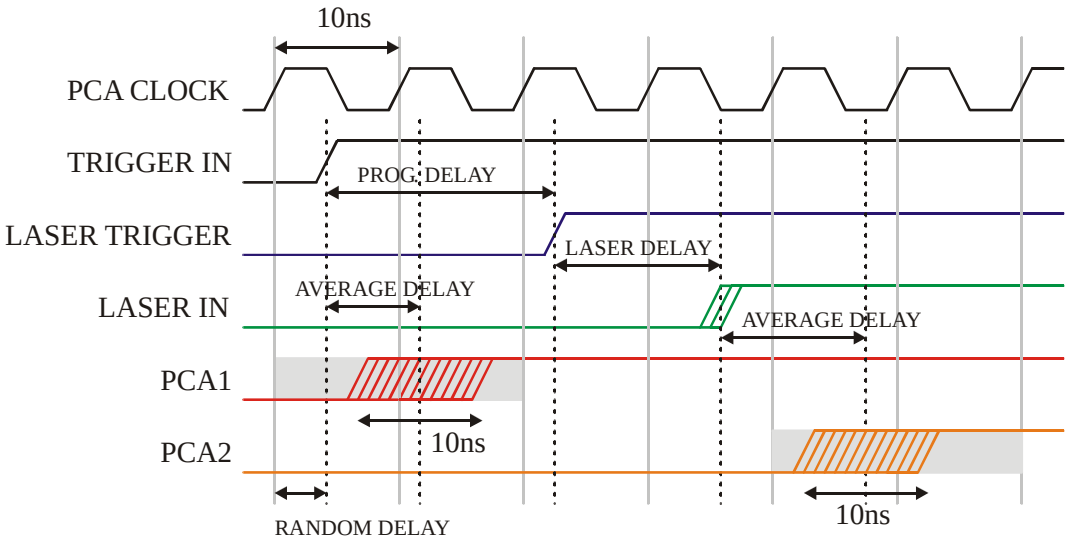

Figure 4.30. *Time diagram of the control signals. The trigger signal is generated externally, therefore it is not synchronized to the system clock therefore two PCA modules are used to measure the resulting delay. The 10ns wide additive dither on both PCA1 and PCA2 signals is used to enhance the 10ns resolution.*

4.8.4 Control algorithm

We have implemented a rather simple and scalable control algorithm to keep the overall delay at the desired level even if the laser delay is changing in time. Note that the flexible hardware allows many solutions for different situations. The algorithm works both for the internally and externally triggered cases; the main difference is the method of measuring the delay as it was described above.

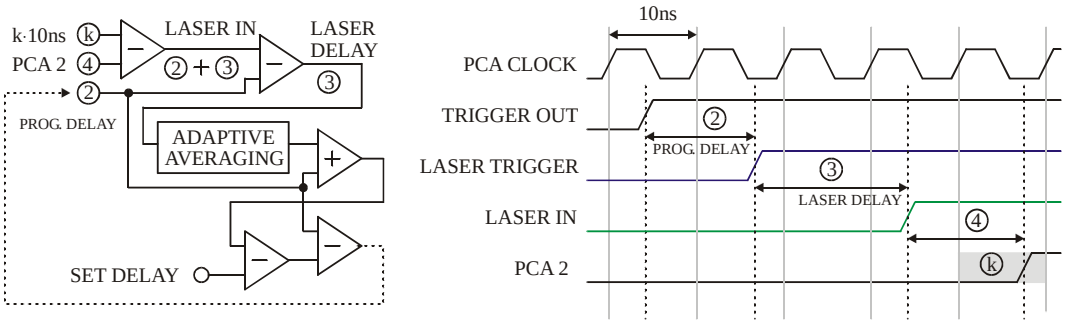

Figure 4.31. *Control algorithm and timing diagram of the signals. The PCA2 module is used to measure the whole delay. Since it has a resolution of 10ns, adaptive averaging is applied to enhance the resolution for repetitive signals.*

The flowchart and time diagram of the control principle can be seen on Figure 4.31. If the laser output is measured at the *k*-th 10ns window, i.e. the PCA2 module captures the value *k*, we can determine the laser delay by subtracting the actual programmed delay values. We can do an adaptive averaging on this fluctuating value to enhance resolution and to get a more precise result. The number of averages is determined during operation; we start with a value of 1 and increase this number if no significant change can be observed in the laser delay. The change detection threshold and maximum number of averages depend on many factors; they must be tuned to their optimum value in the real environment.

4.8.5 Performance of the control operation

We have tested the performance of our control algorithm by numerical simulations using some typical cases and parameter values. The laser jitter was set to 1ns RMS for the simulation of the laser delay step and ramp responses. Figure 4.32 shows the result of the simulation. It can be seen, that due to the adaptive averaging a few laser shots are required to recover from an abrupt change in the laser delay. On the other hand, the algorithm only slightly increases the overall jitter as can be seen by comparing the delay plot with and without jitter

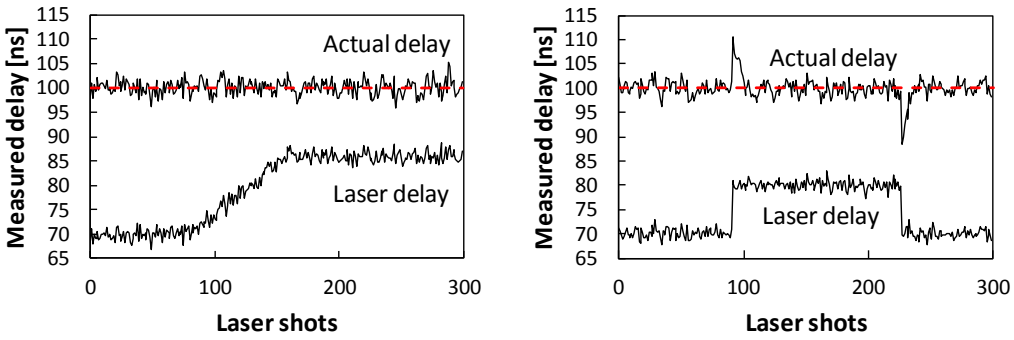

Figure 4.32. *Ramp and step response of the stochastic control system with an adaptive averaging of maximum of 10 samples with laser jitter of 1ns RMS. The dashed line shows the desired delay of 100ns, the actual delay is fluctuating around this value. The ramped and stepped laser delay is shown by in the 70ns-85ns range. The error of the control is 1,52ns RMS.*

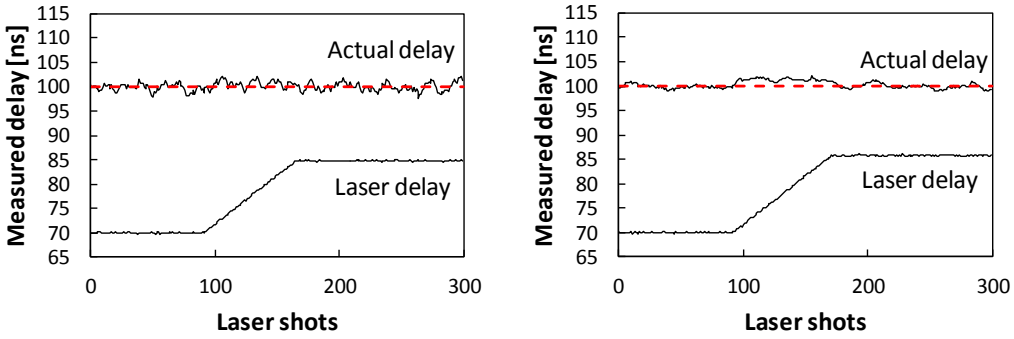

Figure 4.33. *Ramp response of the stochastic control system with an adaptive averaging of maximum of 10 samples (left panel) and 30 samples (right panel) with laser jitter of 100ps RMS. The dashed line shows the desired delay of 100ns, the actual delay is fluctuating around this value. The ramped and stepped laser delay is shown by in the 70ns-85ns range. In the steady state the error of the control for the 10 and 30 maximum averaging number is 660ps RMS and 440ps RMS, respectively.*

Figure 4.33 illustrates ramp response simulation. During ramping the actual delay value is somewhat higher than the desired value, but is it still well below the inherent jitter of the laser. Ramping with higher slope may require different adaptive averaging parameters to have similar performance; however this situation is rather unlikely.

4.9 Conclusions

We have shown several possibilities to obtain high signal-to-noise ratio amplification in systems showing stochastic resonance. According to our numerical simulation results the simplest stochastic resonator, the level-crossing detector can provide very large SNR gains well above 10^4 for periodic pulse like signals with small duty cycles. The mechanism of the gain has been explained theoretically as well.

We have also observed large SNR gains in a bistable system (Schmitt-trigger) for symmetric asymmetric pulse-like signals using the conventional narrow-band and the wide-band SNR calculation. We have built an analog computer and used our DSP data acquisition and control system to show that even a bistable dynamical system, the double well potential has the capability to improve the SNR gain considerably. The same hardware and software environment was used to extend the analysis to aperiodic and wide band signals where we have applied a cross-spectral SNR definition to show SNR gains above unity for all investigated signals.

Numerical simulations and theoretical analysis were performed to analyze the impact of the noise color on the efficiency of stochastic resonance and SNR gain improvement. We have clarified that 1/f noise does not play a special role in the stochastic resonance found in the Fitzhugh-Nagumo neuron model as was suggested earlier. We have extended the investigations to $1/f^{\kappa}$ noises with $0 \leq \kappa \leq 2$ and for the double well system also. We have found that although smaller noise amplitude maximizes the SNR due to the band-pass and low-pass filtering characteristics of these systems, the value of the SNR and SNR gain is smaller, therefore colored noises cannot be considered more efficient. This result is in agreement with the results obtained for different kinds of colored noises [10].

We have shown a rather simple solution to control laser pulse timing using the inherent jitter and additive random dither. We have designed and realized a microcontroller based hardware that has several programmable delay elements and timing units to support control and resolution enhancement by utilizing the different random noise sources. The device can be operated in a stand-alone mode when the embedded processor runs the control algorithm but can also be controlled by a host computer via the USB interface. Internal or external triggering can be selected; random dithering of both the trigger and laser output signals is used to improve time resolution with simple and efficient control algorithm. The low-cost device may also be used in many interdisciplinary applications where sub-ns time resolution and accurate timing control is required with high flexibility. In such applications, the main advantage is that even a single-chip mixed-signal microcontroller can be used with only a few passive external components. There are many microcontrollers on the market with integrated comparators, digital-to-analog converters and timing units, therefore the delay lines and time-to-digital conversion can all be easily implemented, no external circuits or costly application-specific circuits (ASICs) are needed.

5 Fluctuation enhanced gas sensing

5.1 The concept of fluctuation enhanced sensing

Fluctuation enhanced sensing is an emerging way of extracting more information from the output signal of some kind of sensors with the help of intensive analysis of random fluctuations [1-9,E1,E2]. It is well known that noise coming from a system can carry important information about the state and behavior of the subject, however it is not always straightforward to find the experimental and signal processing tools for extracting this information. Safety, home automation, industrial analysis and control are some reasons of growing gas sensor applications. Commercially available Taguchi gas sensors [10,11] and promising nanotechnology-based gas sensors [12-19] show change in their resistance as a function of the concentration of the externally applied different gases. Measuring only the average of this resistance gives only very limited information especially in the presence of a mixture of several gases, while it has been shown that noise analysis can give significantly more information, have the potential to identify the type and concentration of the surrounding gases in some cases.

The principle of fluctuation enhanced sensing is based on the analysis of the power spectral density of the fluctuations. Gas sensors typically exhibit 1/f resistance fluctuations in the low frequency range; however it may have slightly different frequency dependence for different types of applied gases. Sometimes this effect is very weak, therefore simple measures are not enough to make the distinction, more sophisticated pattern recognition methods must be used.

The main advantage of this method is the possibility of providing a single sensor alternative instead of using a set of gas sensors that are sensitive to different types of gases to analyze gas mixtures. This is probably the most frequent situation in a typical gas sensor application.

Developing noise measurement techniques and signal processing methods can help to improve the quality and efficiency of gas sensing, it is also aimed to make low power, portable devices and intelligent sensor networks [20,21, E10].

5.2 Development of measurement systems to support fluctuation enhanced sensing

In most cases a comprehensive set of professional instruments – like low noise preamplifiers, dynamic signal analyzers – are used to perform the measurement and analysis. However, development of compact dedicated instrumentation hardware and associated software can help to improve efficiency of the research and in the same time aids exploitation. We have developed different systems to allow easy and flexible acquisition of resistance fluctuation signals of gas sensors to support fluctuation enhanced analysis [E3-E13].

5.2.1 DSP data acquisition and control system

The gas sensor provides resistance output as a function of the gas concentration, therefore a current source is needed to convert this signal into voltage. Since the resistance fluctuations contain important information about the applied gas type and concentration, a sensitive, high precision and low noise resistance-to-voltage conversion is required.

The first stage of the signal conditioning circuitry is based on a low noise, precision voltage reference, AD780 (Analog Devices). The 2.5V output voltage of this reference is further noise-filtered by passive low pass filters and buffered by a low voltage and current noise operational amplifier.

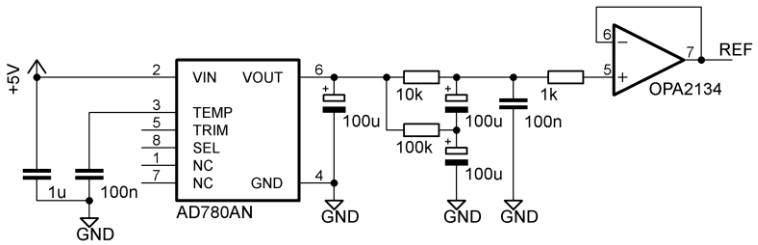

Figure 5.1. *Precision low noise buffered voltage reference. In a single supply application the OPA2134 amplifier can be replaced by a MAX4478 quad operational amplifier.*

This voltage is buffered by a dual (OPA2134) or single supply quad (MAX4478) operational amplifier (see Figure 5.1). Four paralleled low noise amplifiers can be used to reduce the voltage noise of these amplifiers by a factor of two. This filtered, buffered voltage is used as an input to realize a low noise precision current reference using another operational amplifier (OPA2134 or MAX4478). Four selectable reference currents can be used to force current flow through the gas sensor. The output of the current-to-voltage converter amplifier is fed into two different further stages.

One just converts the range of this voltage proportional to sensor resistance to allow digitization of the sensor resistance. The other stage uses high pass filters to remove the DC component of the signal and utilizes a two stage gain of 1000 amplifier to amplify the fluctuating part of the voltage. The schematic of the circuit can be seen on Figure 5.2.

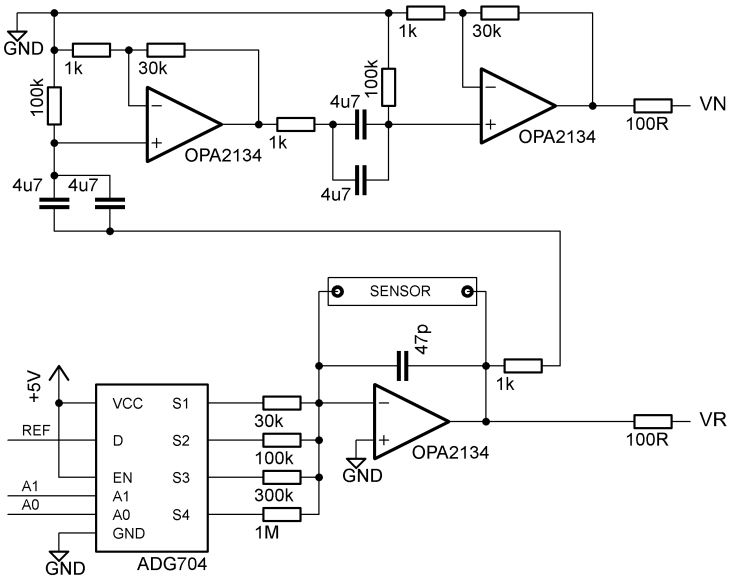

Figure 5.2. *The voltage reference (wire labeled REF) can be connected to the inverting input of the operational amplifier via a software selectable (wires labeled A0 and A1 connected to the ADG704 low R_{ON} analog switch) resistor to form a programmable precision current source. The output VR is a voltage proportional to the sensor resistance while the output VN is the amplified fluctuating component of this voltage.*

The two output signals that are proportional to the resistance and its fluctuations are digitized by a dual 16-bit sigma-delta ADC module and controlled by the personal computer via the DSP interface module (see Chapter 3.4). Note that the oversampling delta sigma architecture of the ADC allowed us to use simple low pass filters to prevent aliasing. The DSP module's UART port is connected to a galvanically isolated UART-to-USB converter (FT232R) to provide a simple host computer interface.

5.2.2 Compact USB port data acquisition module

Although the system described above is a dedicated measurement system for fluctuation enhanced sensing, the modular DSP data acquisition system can be replaced by a more compact solution. We have designed a small FES data acquisition device that consists of an analog signal processing part, a mixed signal microcontroller (C8051F060) to convert the signals into the digital domain and to communicate with the host computer via a universal asynchronous receiver-transmitter (UART)-to-USB interface [E10]. Note that the analog signal conditioning chain includes a programmable gain amplifier and high-precision 8-th order anti-aliasing filter (LTC1564). This filter is required, because the successive approximation sampling ADC does not reject signals above the Nyquist frequency.

Gas sensors often need heating voltage up to 5V; in our system the microcontroller's built-in 12-bit digital-to-analog converter set the heating voltage to the desired value. A second digital-to-analog converter can be used to set the optional gate voltage of the sensor. The block diagram of the system is shown of Figure 5.3, while the photo of the system and the plug-in preamplifier module can be seen on Figure 5.4 and 5.5, respectively.

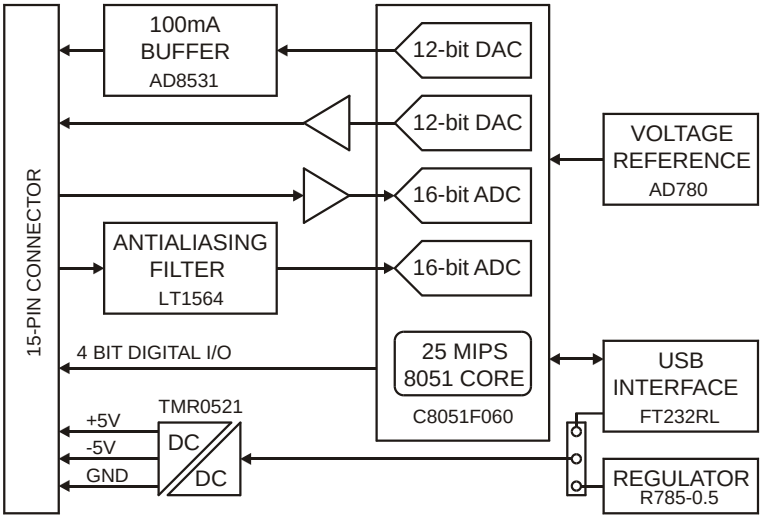

Figure 5.3. *Block diagram of the USB FES data acquisition module.*

Figure 5.4. *Photo of the USB FES data acquisition module*

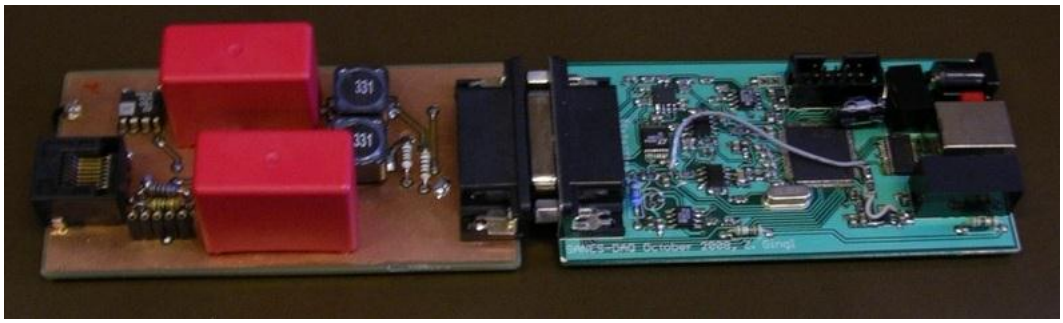

Figure 5.5. *Photo of the USB FES data acquisition module with a signal conditioning plug-in board containing the low noise sensor excitation and preamplifier electronics.*

The external analog signal conditioning plug-in board uses practically the same circuitry as in the case of the DSP data acquisition system.

5.2.3 Complete 2-channel fluctuation enhanced gas analyzer

In some cases a complete system is required that can accept more sensors for the experiments especially in sensor evaluation projects. If the device has a USB interface, it can also be plugged in a USB hub therefore a scalable wired USB sensor network can be realized. In the following we describe our system that fits the above mentioned aims.

The main component of the data acquisition system is again a precision mixed-signal microcontroller (C8051F060). The two output voltages of the analog signal processing part is digitized simultaneously by the microcontroller's dual 16-bit analog-to-digital converters. The on-chip SRAM (BS62LV4006) can be used as a temporary buffer for digitized data to ensure continuous, real-time sampling and data transfer to the host computer via the UART-USB interface chip (FT232RL). The sampling frequency can be set up to 50kHz ensuring maximum measured signal bandwidth of 20kHz, adequate for fluctuation-enhanced sensing applications.

The supply options include powering the device from the USB port or an external DC supply by the use of a low-noise, properly filtered DC/DC converter (TMR2-0521).

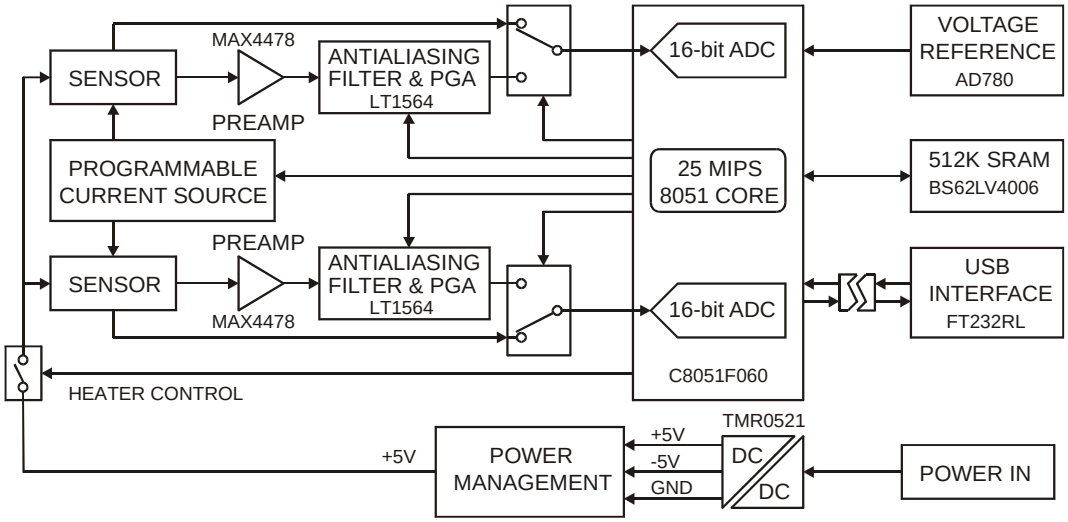

Figure 5.6. *Block diagram of the dual channel complete USB FES module*

The block diagram and the photo of the assembled printed circuit board of the system can be seen of Figure 5.6 and Figure 5.7, respectively.

The standard Eurocard format printed circuit board fits in an enclosure that holds the gas chamber assembly (see Figure 5.8). Note that the enclosure allows the use of two boards therefore a total of four sensors can be measured simultaneously.

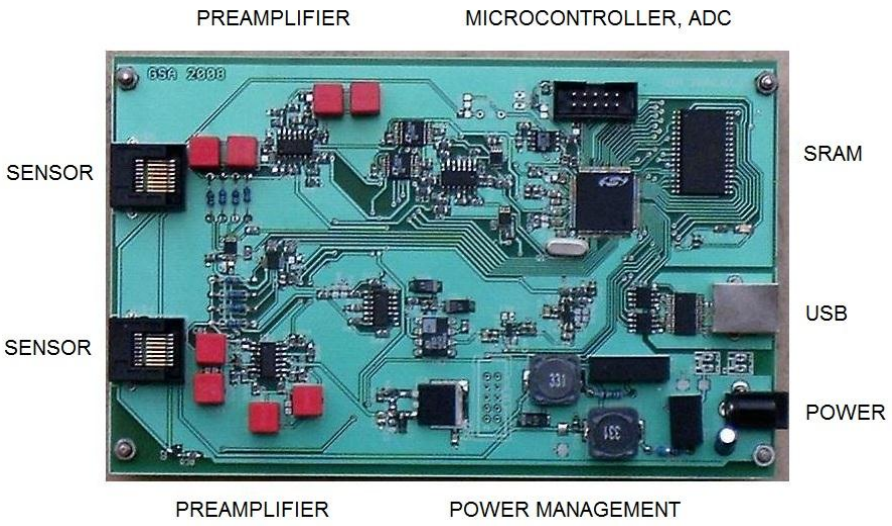

Figure 5.7. *PCB photo of the dual channel complete USB FES module*

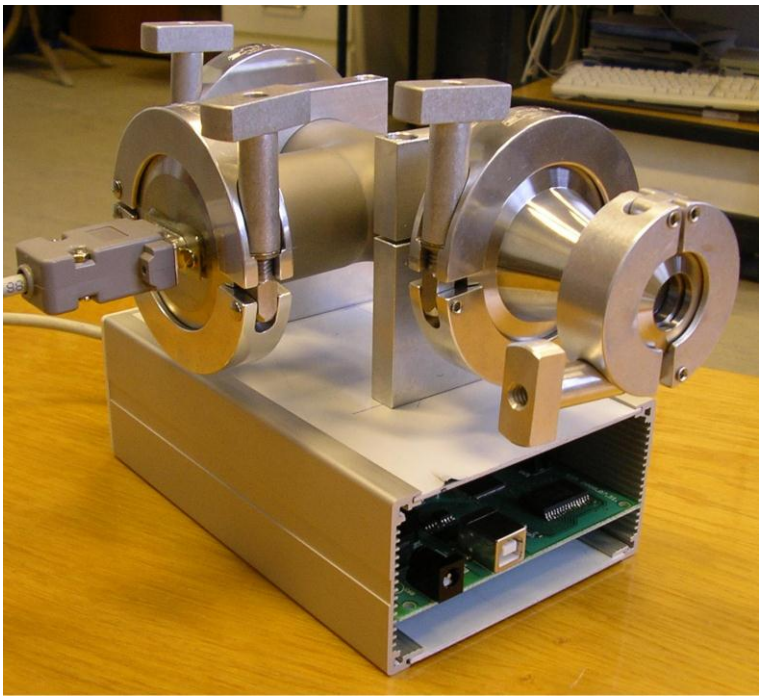

Figure 5.8. *Gas chamber mounted on the enclosure of the dual channel complete USB FES module.*

5.2.3.1 Data acquisition and control software

The microcontroller of the system runs simple software that configures the analog preprocessing circuitry, sets the sample rate and controls the analog-to-digital conversion. The host communication is made easy by interpreting bytes received from the host as commands. The microcontroller does not make complete digital signal processing, only transfers the raw digitized data to the host computer for analysis. Note

that no data loss is guaranteed by the use of the on-board SRAM that is handled as a ring buffer by the FIFO algorithm implemented on the 8051 core.

The host PC controls the data acquisition, sensor excitation and signal conditioning parameters by sending the commands to the microcontroller. The graphical user interface software allows easy setup of the measurement parameters and saves the acquired data into a binary file for further processing. The acquired data can be displayed and the PSD can also be estimated using a given number of averages. The user can select the signal to be measured (resistance or its fluctuation), can set the rotation speed of the gas flow control fan also.

The main software elements are the user interface, which includes the controls and plots the data on the screen. A separate thread is used for communication with the unit. The code is developed using Microsoft Visual C++ and runs under Windows XP and Windows 7. A screenshot is shown on Figure 5.9.

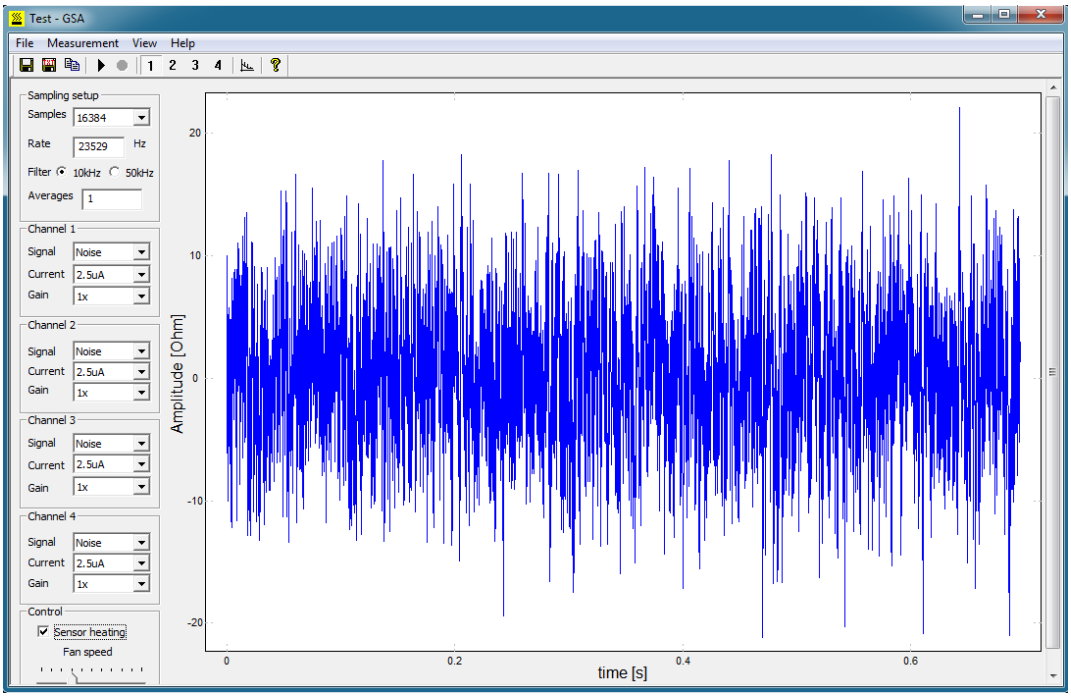

Figure 5.9. *Screen shot of the data acquisition and control software.*

5.3 Experimental results

Our special instruments used in several FES projects done in various collaborations. The following sections summarize the work and the most important research results.

5.3.1 Fluctuation enhanced sensing with carbon nanotube gas sensors

We have started collaboration with research groups working at the Department of Optics and Quantum Electronics, University of Szeged, Hungary, Department of Applied and Environmental Chemistry, University of Szeged, Hungary, Microelectronics and Materials Physics Laboratories and EMPART Research Group of Infotech Oulu, University of Oulu, Finland, Laserprobe LP Ltd, Finland. The collaboration was a part of a successful European Union project called SANES

(*Integrated Self-Adjusting Nano-Electronic Sensors*, for more information see http://cordis.europa.eu/).

Our contribution to the research included the development of the specialized instrumentation, the expertise in the field of noise research and signal processing, development of software for simulations, measurement, control and data evaluation [E3-E9].

The block diagram and the photo of the experimental setup is depicted of Figure 5.10 and Figure 5.11, respectively. Three independent gas sources were connected to software programmable flow controllers (Brooks Instrument type 5850S, full scale flow: 1 l/min, 3 ml/min and 10 ml/min). This allowed accurate control of the concentration of the gas mixture in the chamber. The flow controllers were connected to a galvanically isolated USB-RS485 converter developed by R. Mingesz and the communication was provided by the use of the HART protocol.

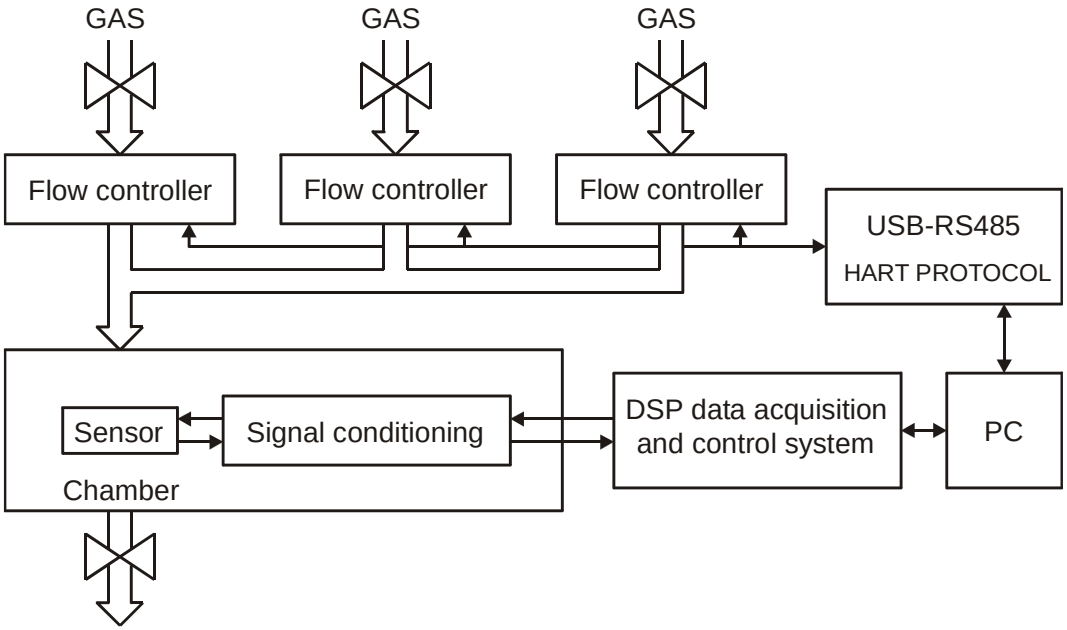

Figure 5.10. *Block diagram of the experimental setup.*

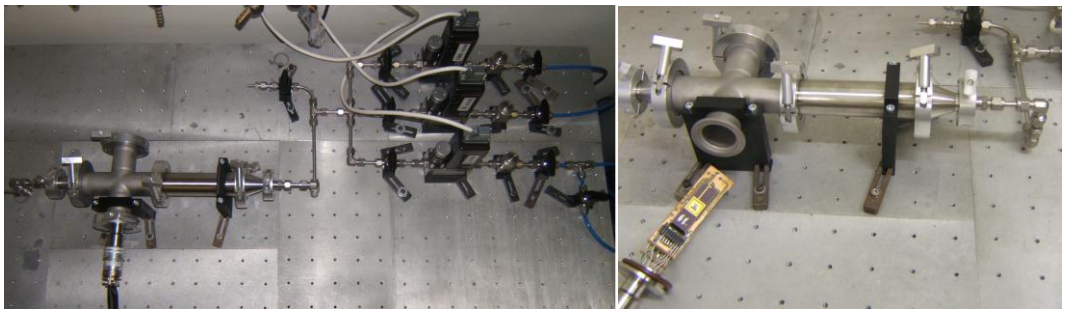

Figure 5.11. *Photo of the gas chamber and flow controller system. The sensor that can be plugged in the four-way chamber is shown on the right. The sensor is mounted on a small printed circuit board that holds the low noise current source and preamplifier.*

The mechanical components were ordered from the Kurt J. Lesker Company (www.lesker.com) and the arrangement has been designed by P. Heszler. The four-way

stainless steel chamber accepted the gas input via a filter that helps to get homogeneous concentration distribution. The sensor was mounted on an electrical feedthrough and was oriented in perpendicular to the gas flow.

The precision low noise source forced a constant current flowing through the resistive sensor and the voltage fluctuations between the sensor contacts were band-limited between 0,1Hz and 20kHz and this AC signal was amplified by 1000. The raw DC voltage and the amplified signals were corresponding to the resistance and its fluctuations, respectively. Both signals were connected to our DSP data acquisition and control system including the dual 16-bit simultaneous data acquisition module described in Chapter 3.4.

Carbon nanotubes have already been used as gas sensors in different application modes. Resistance measurements, transistor gain measurements and field emission current measurements are all explored, however the selectivity of the sensors found to be rather poor. This is a point where fluctuation enhanced sensing has a perspective, since it goes much beyond measuring only a slowly varying average value of the resistance of the sample. Carbon nanotube blocks and contacts between them are non-uniform therefore they have different adsorption properties even if functionalization for tailoring the chemical selectivity is not applied. Consequently analyzing the noise pattern of the resistance may give additional information compared to observing the magnitude or the average value of the fluctuating resistance.

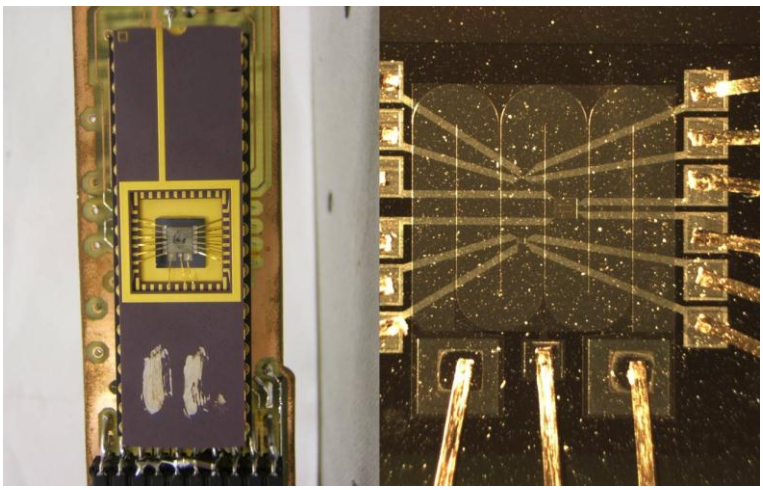

Figure 5.12. *Photo of the carbon nanotube gas sensors mounted on a ceramic dual in-line package. The photo on the left shows the carrier printed circuit board on which the low noise analog signal conditioning components are soldered.*

The thin film carbon nanotube sensors used in the investigation were made at the Department of Applied and Environmental Chemistry. Different single wall functionalized carbon nanotube (SWCNT) and multi wall functionalized carbon nanotube (MWCNT) sensors were tested. Here we briefly demonstrate the applicability of the FES method with some examples only; the detailed results for the are given in the references. The sensor is mounted in a ceramic dual in-line package (see Figure 5.12) and the resistance could be measured in a two or four-wire arrangement. Gas sensors typically need heating during operation to remove contaminants. The thin platinum wire was used for the heating and measuring the substrate temperature as well by monitoring the wire resistance.

The sensor resistance fell into the range from a few kOhms to a few hundred kOhms, therefore we have applied 10μA to 100μA probe currents. The sample rate was 10kHz to 20kHz and the power spectral density of the noise was measured by averaging of 100 recordings. The sensor was exposed to different concentration and mixture of gases including CO, N_2O, H_2S and H_2O vapor, and the principal component analysis (PCA) was used as a pattern recognition method in order to try to get more information out of the data. The aim was to find out if the analysis of the sensor signal can be used to evaluate the type and concentration of the applied gas, or the composition of certain gas mixtures. Figure 5.13 shows the typical power spectral density of the resistance fluctuations and the score plot of the PCA analysis for four different gases with a concentration of 50 ppm. On the right plot a better selectivity of the PCA method is shown. Note that he power spectral density follows the 1/f frequency dependence as it was expected. The power line interference of 50Hz and harmonics were carefully removed before applying the PCA analysis.

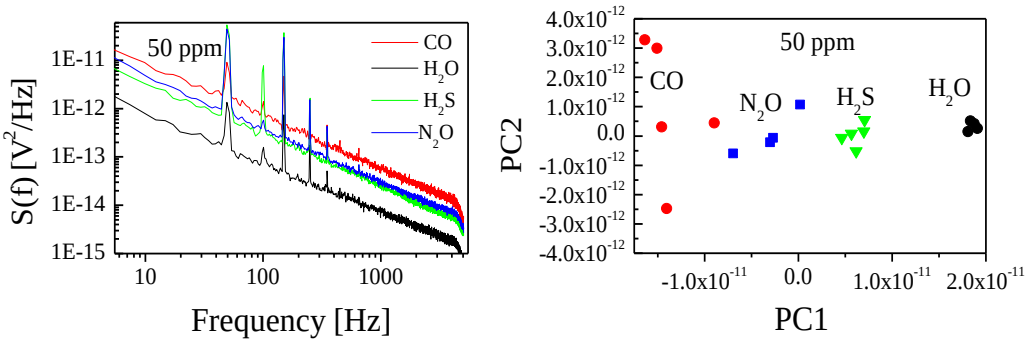

Figure 5.13. *a) Power spectral densities recorded from a 1,8 diamino-octane functionalized CNT sensor exposed to 50 ppm CO, N_2O, H_2S and H_2O respectively. b) Score plot of PCA analysis for the same exposures, CO (red circle), N_2O (blue square), H_2S (green triangle) and H_2O (black circle). The number of averages is 100.*

Figure 5.14 shows the PCA analysis plot for different type and concentration gases using a single CNT sensor. The sensor is functionalized with carboxyl, the temperature was 25°C, the buffer gas was argon. The CO, NO and CH4 gases are clearly separated on the PCA plot. The behavior for different concentration of the chosen CO gas is depicted on Figure 5.15. At low concentration the PCA points are rather scattered showing larger statistical error; at higher concentrations the error is significantly smaller.

We can conclude that while observing the average value of the sensor resistance or the magnitude of its fluctuations can't be used to make distinction between the type of gases and do not give usable information about composition of mixed applied gases, the PCA analysis using the set of power spectral densities may turn the same sensor into a chemically selective device.

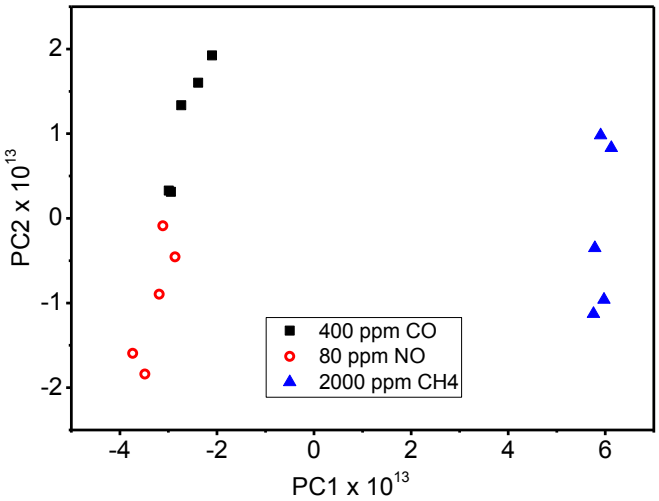

***Figure 5.14**. PCA analysis plot for different type gases using a single CNT sensor is shown. The sensor is functionalized with carboxyl, the temperature was 25°C, the buffer gas was argon.*

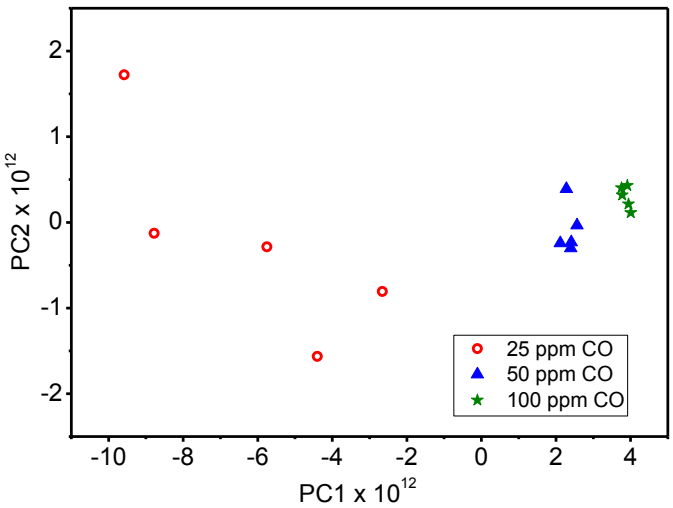

***Figure 5.15**. PCA analysis for different concentration of CO gas using a single sulfonated CNT sensor. The temperature was 80°C, the buffer gas was argon.*

5.3.2 Drift effects in fluctuation enhanced sensing

Significant changes in the concentration, composition of the gas mixture and heating may cause a longer term drift of the sensor resistance. However, the PSD acquisitions need considerable amount of time especially due to averaging; therefore the drift can affect the results of the PSD estimation, what is even worse, this can corrupt the data obtained by the PCA analysis and result in serious degradation of accuracy and selectivity. In order to investigate the effect of various drift levels on the gas sensing accuracy we have carried out measurements and numerical simulations [E4].

Figure 5.16 shows the measured resistance evolution during heat cycling. When the sensor heating was turned on, the resistance started to decrease abruptly and upon turning the heating off a long lasting drift could be observed. The PSD acquisitions are

typically done in this regime. On the right hand side the fluctuating resistance value is plotted showing the additive drift.

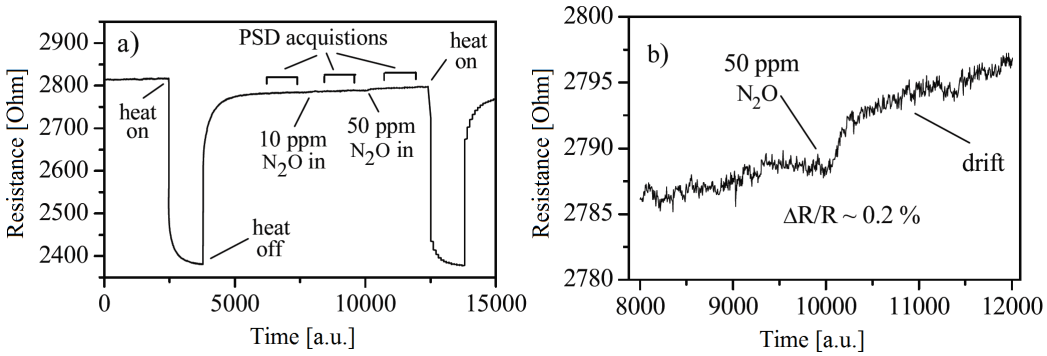

Figure 5.16. *Resistance change versus time for a typical measurement including a) heat pulse on and off followed by introduction of 10 and 50 ppm N_2O with a b) close up region for 50 ppm N_2O injection. The sensor was MWCNT functionalized by 1,8 diamino-octane.*

We have developed a numerical simulation framework in C++ programming environment to analyze the effect of the drift. The sensor's simulated 1/f resistance fluctuations were generated using the method described in Chapter 1.2.1 and the magnitude was fine tuned to be compatible with the measured PSD. On Figure 5.17 the measured and simulated PSDs are plotted.

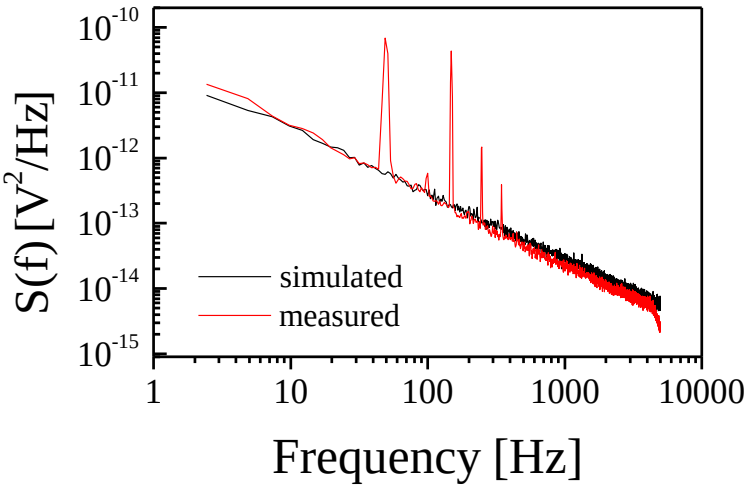

Figure 5.17. *Simulated 1/f (black) and observed (red) power spectral densities of a CNT sensor. The measurement was taken upon 50 ppm N_2O exposure. The simulation was performed with a mean resistance of 2.8 kΩ with no drift, RMS of the resistance variance was 0.01 Ω, probe current 100 μA. These latter data correspond to the experimental values. The peaks at 50, 100, 150, 250 and 350 Hz in the measured spectrum are the fundamental and higher harmonics of the 50 Hz line frequency. The number of averages was 100.*

We have applied drift values of 0.01, 0.05, 0.1, 1 Ω/s and the PSDs were calculated in the range of 2Hz-5000Hz. Figure 5.18 suggests that the PSDs are affected considerably with drift values over 0.1 Ω/s. The much more sensitive PCA analysis confirmed this as depicted on Figure 5.19. The 0.1 Ω/s drift with 2.8 kΩ resistance mean value corresponds to a $4x10^{-5}$ 1/s relative drift. In our observations we have found typical drift values from 0.002 Ω/s to 0.005 Ω/s, this is well in the safe range.

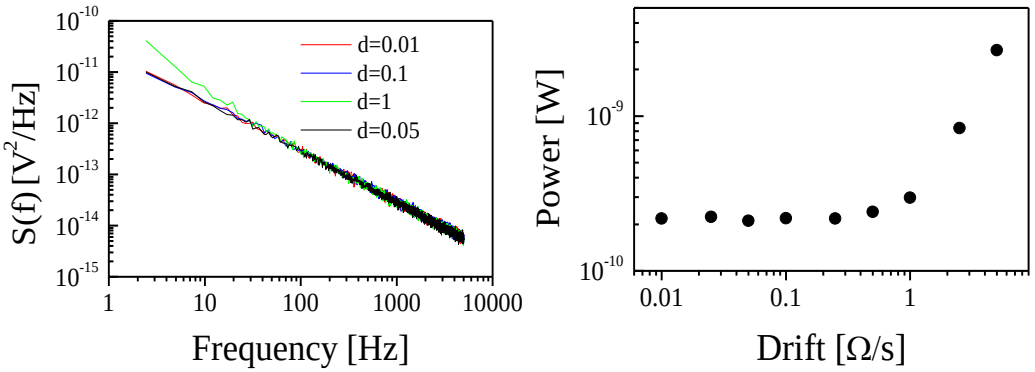

Figure 5.18. *The left panel shows the simulated spectra with different drift (d) values in Ω/s and while noise power in the simulated spectral window versus drift can be seen on the right.*

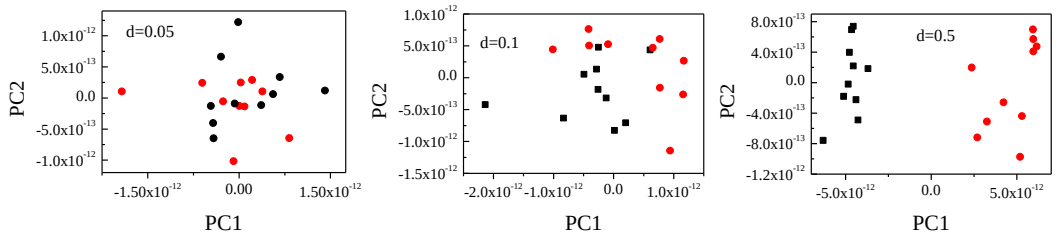

Figure 5.19. *Score plots of PCA analysis of the simulated PSDs for various drift (d) values in Ω/s. Symbols with full and open circles correspond to drift and no drift, respectively. The frequency window of the PSD is 2-5000 Hz.*

5.3.3 Bacterial odor sensing

A very promising application field of fluctuation enhanced sensing is biological agent detection and identification [22]. Taguchi semiconductor gas sensors or nanotechnology gas sensors can be sensitive to such contaminants; therefore the same concept can be applied as was shown in the case of CNT sensors.

We have a continuous collaboration with prof. Kish (Department of Electrical and Computer Engineering, Texas A&M University, USA) in many fields of noise research. A further collaborator is the company Signal Processing Inc. (CEO: Chiman Kwan, Rockville, Maryland, USA) in the FES measurements and analysis. We have developed the USB FES data acquisition and control unit and software described in V.2.C especially to support this collaboration and we have also installed a DSP-based 16-bit simultaneously sampling data acquisition system (see Chapter 3.1. and 3.4.) at the Fluctuation exploitation laboratory of the Texas A&M University to aid the measurements.

Figure 5.20 shows an example of the power spectral densities obtained with an SP32 ethanol-sensitive tin dioxide semiconductor Taguchi-type gas sensor exposed to bacterial odors (vegetative Escherichia coli, and Anthrax-surrogate Bacillus subtilis spores) [E11]. The single sensor could be used to make distinction between the empty chamber (air); tryptic soy agar (TSA) medium and TSA with bacteria. The number of bacteria fell in the range of $2.5 \cdot 10^4$-10^6. Although this number is not low, without using the FES method, the SP32 Taguchi sensor can't give any information about the bacteria; the average value of its resistance remained unchanged.

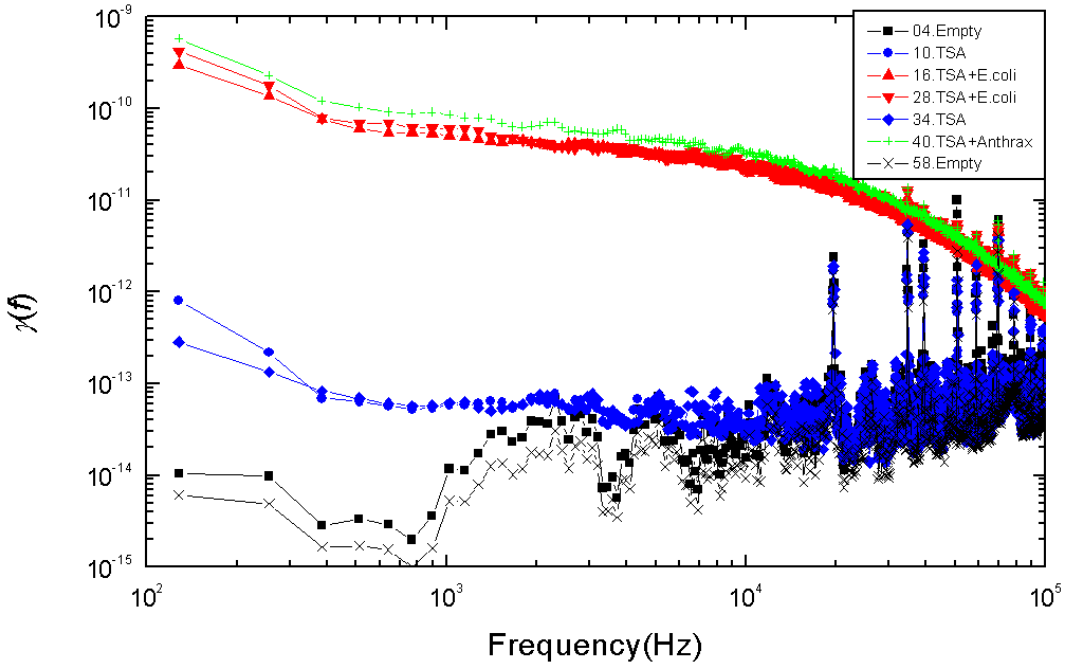

Figure 5.20. *Normalized power density spectra of the resistance fluctuations of the sensor SP32 measured in the sampling-and-hold working mode. Each sample had one million bacteria. The alias "Anthrax" stands for Anthrax surrogate Bacillus subtilis.*

Although there are many efficient pattern recognition methods (including the PCA analysis, for example), even very simple ones can work properly in cases when the PSDs exhibit rather different behavior for different gases or odors to be distinguished. Kish introduced the concept of “binary fingerprint” for FES applications which focuses on the slope of the power spectral density in different frequency bands [23].

The idea is to divide the frequency range used for the analysis into neighboring frequency bands. For each frequency band the local slope of the logarithm of the PSD as a function of the logarithm of the frequency can be determined. If this slope is larger than the global slope using the whole frequency range then 1 is assigned to this frequency band; -1 otherwise. Figure 5.21 shows 6-bit binary patterns corresponding to four different odors. This method is rather simple and allows easy and fast computation.

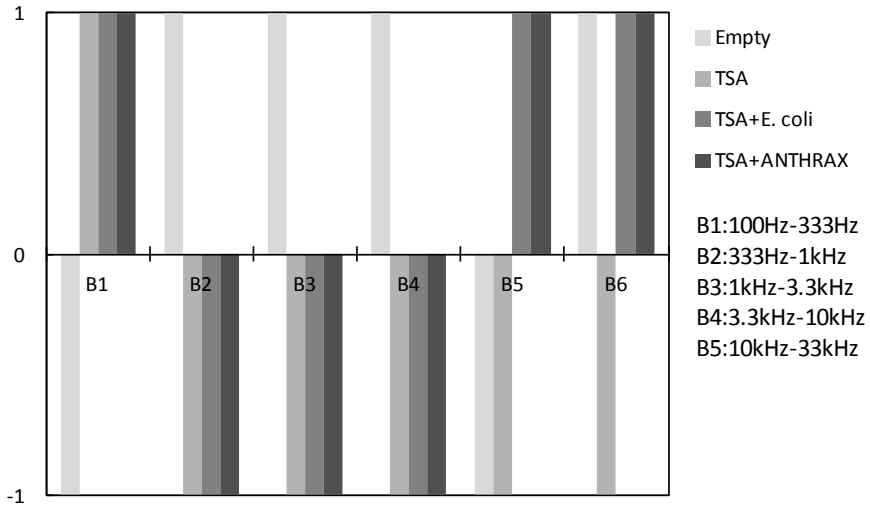

Figure 5.21. 6-bit binary pattern derived from the power spectral densities. Each bit corresponds to a certain frequency range indicated below the bars. The value is 1, if the local slope of the spectrum in the frequency range is larger than the average global slope, -1 otherwise.

5.4 Fluctuation enhanced sensing based on zero crossing statistics

Rapidly growing sensor applications including the detection of various gases and odors more and more often require small, compact size, stand-alone operation and real-time processing and the possibility to be integrated in a wired or wireless sensor network. At first sight FES needs considerable processing power, however we have already shown above that simplifications can be made in certain cases.

In the following we'll show another alternative that does not require the estimation of the power spectral density and can be used to accelerate the calculations therefore lower power operation can be achieved allowing the application of simple low power microcontrollers to make battery-powered sensor nodes, smart sensors [E12].

Our approach is based on the method of Kedem [24] that uses low pass filters and zero-crossing analysis to estimate the power spectral density of Gaussian fluctuations. In order to accelerate the calculations and still provide enough accuracy to provide FES fingerprinting we have modified the Kedem's method.

The zero-crossing frequency of a zero mean stationary Gaussian stochastic process can be given by the Rice formula [3]:

$$f_z = 2\frac{\sqrt{\int_0^\infty f^2 S(f)df}}{\sqrt{\int_0^\infty S(f)df}}, \tag{5.1}$$

where f_z is the average zero-crossing frequency, $S(f)$ is the power spectral density of the fluctuating signal $U(t)$.

We consider a sampled signal and divide the measurement time window into uniform subwindows of length $\Delta t \cdot N_j$, where Δt is the sampling time interval. In such a time window the local average value of the signal can be computed as:

$$U_0(N_j) = \frac{1}{N_j}\sum_{i=1}^{N_j} U(t_i). \tag{5.2}$$

Using this value the average relative zero crossing frequency in the given subwindow can be calculated easily just by counting how many times the signal crosses the level $U_0(N_j)$ divided by N_j. The next step is to calculate the average of the subwindow's zero crossing frequency values over the whole measurement window.

$$f_{z,j} = \frac{N_j}{N}\sum_{k=1}^{N_j/N} f_{z,j,k}\,, \tag{5.3}$$

where $f_{z,j}$ is the average zero crossing frequency over the whole measurement range, $f_{z,j,k}$ is the average zero crossing frequency in the k-th subwindow and N is the total number of samples. In our calculations we have chosen $N_j=N/2^j$ with conditions $j\geq 0$ and $N_j\geq 16$ thus we'll have $\log_2(N)$-4 different values for the average zero crossing frequencies serving as the noise fingerprint data.

In order to demonstrate the efficiency of the method, we have generated four different kind of noise patters using numerical simulations that can correspond to different chemical processes:

- **A** is a Gaussian noise with Lorentzian power spectral density obtained by first order low pass filtering of white noise similar to adsorption-desorption noise, also can be considered as noise of the signal conditioning path;
- **B** is a random telegraph signal that can represent single molecule adsorption-desorption noise of a nanosensor;
- **C** is a single molecule diffusion noise of a nanosensor and is generated by an amplitude-limited one-dimensional random walk;
- **D** is a similar to **C** but the diffusion coefficient is 25 times greater.

We have generated ten different mixtures of the four types of independent processes. A-A, B-B, C-C, D-D are the sum of two independent A,B,C and D processes, respectively, while A-B, A-A-B, A-B-B, C-D, C-C-D, C-D-D represent the sum of the two or three corresponding independent processes. With the original four signals we have then 14 classes of signals for the analysis.

Figures 5.22, 5.23 and 5.24 show the computed zero crossing patterns and the power spectral densities of the corresponding signals. One can see that the zero crossing patters can give more distinct signatures for the different signals with respect to each other, while the PSDs can be more similar.

The efficiency of the use of the zero-crossing patterns compared to the use of the PSDs are classified by two pattern recognizers: a minimum distance classifier and the support vector machine (SVM) classifier that is extensively used as an efficient tool in pattern recognition and regression tasks [25,26]. The results obtained with both classifiers showed that the zero-crossing patterns provided more accurate and reliable classification compared to classification based on the use of the PSDs. The details are given in [E12].

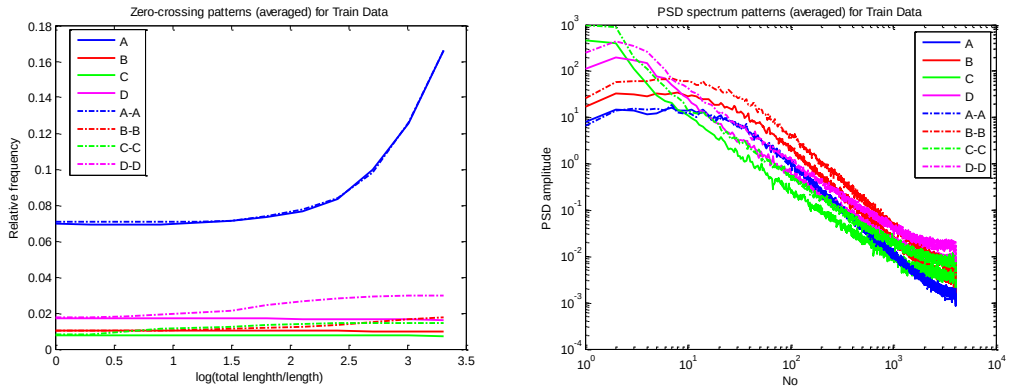

Figure 5.22. *Zero-crossing and PSD patterns (averaged) for stochastic signals (A, B, C, D, A-A, B-B, C-C, D-D)*

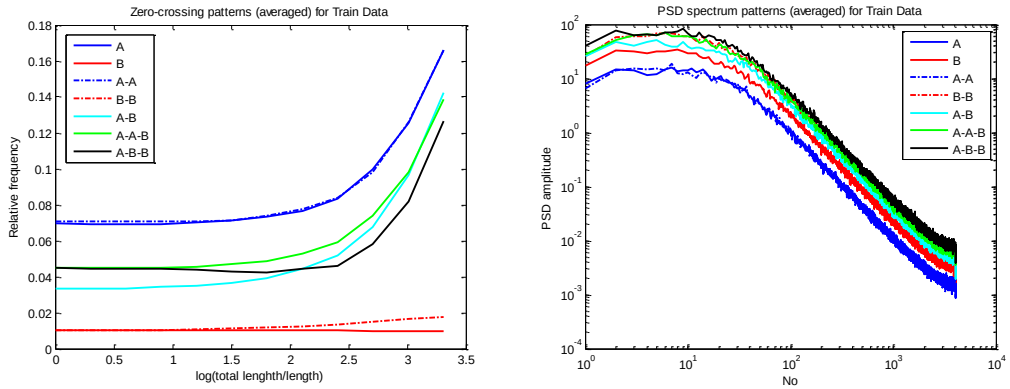

Figure 5.23. *Zero-crossing and PSD patterns (averaged) for stochastic signals (A, B, A-A, B-B, A-B, A-A-B, A-B-B).*

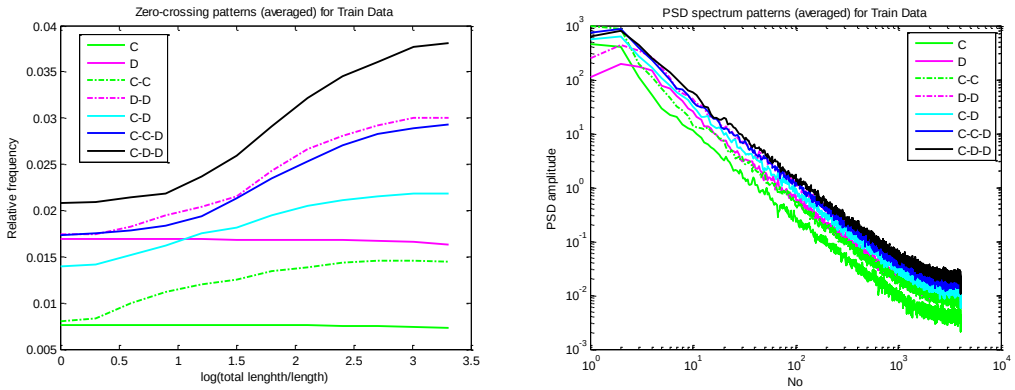

Figure 5.24. *Zero-crossing and PSD patterns (averaged) for stochastic signals (C, D, C-C, D-D, C-D, C-C-D, C-D-D).*

5.5 Conclusions

We have shown computer controlled instruments that have been developed for fluctuation-enhanced gas sensing measurements. The units use special low noise analog signal conditioning to interface the sensor to the high-resolution data converters. In addition to the universal modular DSP processor based version, two small and compact mixed-signal microcontroller based USB powered devices and the associated embedded and host computer software have also been developed. A graphical user interface

software application controls the whole measurement process and allows real-time noise measurement and spectral analysis. A PCA algorithm has been implemented to extract information about the type and concentration of the applied gas. Experiments were carried out on CNT gas sensors with different gases and concentrations in an international collaboration funded by the European Union. It was shown that fluctuation enhanced sensing can improve the selectivity of different nanomaterials. One of the aims of the collaboration that we could successfully achieve was to develop a small portable device that can serve as a basis for further exploitation.

Additionally numerical simulations have been performed to explore the influence of the drift effects typically found in the measurements on the result of the analysis. Comparing the experimental a simulation data we can conclude that the selectivity provided by the PCA analysis is not affected considerably by the typical drifts found in the experiments.

In order to aid the development of low-power, stand-alone fluctuation enhanced devices and sensor nodes we have proposed a method based on the zero crossing statistics of the sensor's resistance fluctuations. The efficiency of the use of the zero-crossing patterns compared to the use of the PSDs were verified by two pattern recognizers.

6 Secure communication using thermal noise

6.1 Unconditionally secure communication

Secure communication is one of the most critical and important problem of information technology, no doubts about that. Protecting information leak about personal and official data, passwords, security information can be extremely challenging since almost every computer is interconnected via the internet, operating systems are rather complex therefore it is hard to guarantee the security against the increasing number of ways of attacks.

Encrypting the information and generating and sharing the security keys are performed by deterministic algorithms. This holds for the software generation of random numbers: more precisely, these are pseudorandom numbers [1]. There are several methods to improve the randomness and to improve encryption (like one-time pad), however due to the deterministic nature unconditional security is a bit questionable.

There are attempts to address this problem, there are devices on the market to provide "true" random numbers [2,3] and researchers hope to find the way of unconditional security with quantum communicators [14] that rely on naturally probabilistic physical phenomena.

Recently a very simple, theoretically unconditionally secure communication scheme based on classical physical phenomena has been introduced [5,6] as an efficient and reliable alternative of the quantum communication that is much more complex and costly. In the following we shall introduce the principle and report the experimental results obtained by a DSP based system that we have developed to demonstrate the communication in a real environment [F1-F3].

6.2 Kirchhoff Loop Johnson Noise secure communications

The block diagram of the Kirchhoff Loop Johnson Noise (KLJN) secure communications is shown on Figure 6.1.

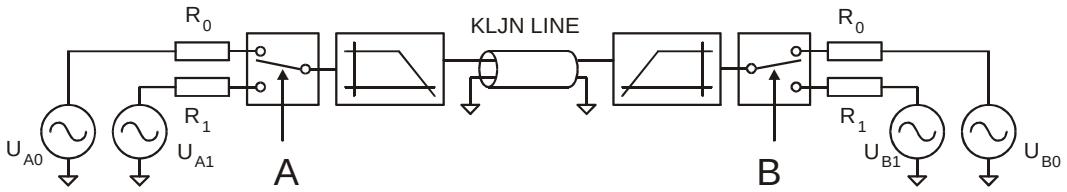

Figure 6.1. *Block diagram of the KLJN communicator. The instantaneous current and voltage data are measured and compared at the two ends and, in the case of deviance an eavesdropping is detected; the currently exchanged bit is not used. The low-pass line filters are required to protect against out-of-alarm frequency band breaking attempts and false alarms due to parasitic transients. False alarms would occur due to transients or propagation effects, illegal frequency components or external disturbance of the current-voltage-balance in the wire.*

The principle is based on the use of a low and high value resistors at both communicators – typically named as Alice and Bob – and one of them can be selected to be connected to the communication wire by a two state signal (*A* and *B*). Real

resistors have their thermal (Johnson) noise; here its electrical equivalent is used: a voltage source and a series noiseless resistor. The U_{Ai} and U_{Bi} independent white noise sources have the power spectral density of KR_i, i=0,1. In a real physical system $K=4kT$, where k is the Boltzmann constant and T is the temperature; however in a model system it is better to choose K using practical consideration like large enough signal amplitude. We assume that all these values are public.

How this arrangement can be used to exchange one bit of information? If the lower value resistor is selected at both ends – in other words A=L and B=L, R_0 and U_{A0},U_{B0} is selected – Alice and Bob knows the state of the A and B bits at both ends by measuring the voltage and the current at their own side, since they will observe low voltage. For the A=H and B=H state, when the high value resistor is switched on at both ends, the voltage will be high on the whole line. This means that the eavesdropper will also know exactly the states of the bits A and B in both cases. However, A=L, B=H and A=H, B=L combination will result the same voltage and current noise on the whole communication line, therefore the eavesdropper has no information about the bits A and B while Alice knows the state of her switch therefore knows the state of the switch at Bob as well. Therefore the LH and HL states can be used for secure communication and information exchange. Note that this communications is used for secure key exchange only; the public communication line (for example the internet) is used to share the data.

In the ideal state this key exchange method is absolutely secure, it has not been cracked. To provide security against arbitrary types of attacks, the instantaneous currents and voltages are measured at both end by Alice and Bob and they are published and compared. In the idealized scheme of the KLJN cipher, the passively observing eavesdropper can extract zero bit (zero-bit security) of information and the actively eavesdropping observer can extract at most one bit before getting discovered (one-bit security) [4].

6.3 Development of a DSP based KLJN secure communicator

The realization of the KLJN communication system introduces non-ideal behavior caused by considerable communication wire resistance and capacitance, limited tolerance of component values, additional noise and interference, transients during the switch state changes and one should make bandwidth considerations as well. Any deviation from the properties of the unconditionally secure ideal system may degrade the reliability, may cause information leak [6-12]. Figure 6.2 shows the block diagram of a real KLJN communicator unit. Since the thermal noise of a resistor is very small and the impedance can be rather high, it is more practical to generate a high enough white noise with a certain bandwidth and use low value resistors to keep the impedance low and prevent from the influence of other noise sources and external interference. The voltage and the current can be measured and used to extract the key information.

In order to demonstrate the KLJN operation in a real system and verify the security of the key exchange protocol we have developed DSP based KLJN secure communicator units that can be connected to a host computer. We have made several experiments to test the operation of the system and several security tests have been performed as well.

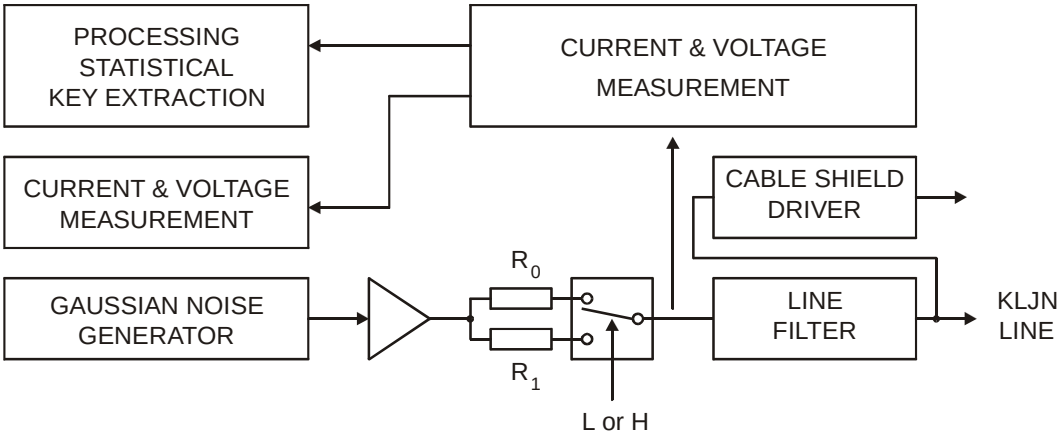

Figure 6.2. *Block diagram of a practical KLJN secure classical communicator. The R_0 (L) and R_1 (H) resistors are randomly selected beginning of each clock period and are driven by corresponding Johnson-like noise voltages. The controlling computer has a regular network connection with the computer of the other KLJN communicator.*

The KLJN units were realized using our modular DSP system described in Chapter 3.

The ADSP-2181 module was connected to the host computer via a legacy RS232 asynchronous serial interface. The four channel analog input/output module based on a AD7865 quad simultaneously sampling 14-bit ADC and four analog outputs were realized by the AD7836 quad 14-bit DAC. The communication line current and voltage data were measured by this unit. The Johnson-like noise was generated on the host computer and downloaded to the DSP's data memory. The DSP sent these data to the DAC with precise timing and the DAC output was filtered by an 8-th order switched capacitor Butterworth filter clocked at 50 kHz, while the remaining small noise components were removed by continuous time analog filters in order to satisfy the KLJN preconditions of removing any spurious frequency components.

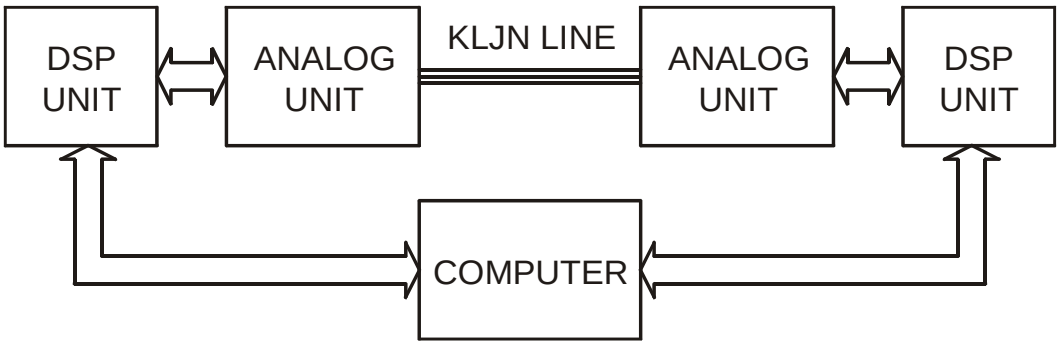

Figure 6.3. *The block diagram of the realized and tested KLJN communicator pair. The KLJN line is a model line with capacitance compensation up to 2000 km range.*

The low and high resistors had values of 2kΩ and 11kΩ, respectively. In both cases an 1kΩ resistor was the first part whose output was connected to ground via 1nF to reduce unwanted high frequency components and this was followed by an 1kΩ and 10kΩ resistor to form the 2kΩ and 11kΩ, respectively. The KLJN line was a model-line representing ranges up to 2000km. Assuming shield driving to cancel capacitance and proper wire diameter a single resistor can be used to realize the KLJN line.

6.4 Experiments

During the tests of a bit exchange the noise was ramped down linearly before making the switching of the resistors and then ramped up. The ramping time was 8% of the whole bit exchange time (clock period). After switching and noise ramp-up another 8% of clock period was elapsed before taking samples from the noise in order to do the statistical key extraction.

Figure 6.4 shows the voltage and current distributions obtained by evaluating 74497 clock cycles. One can easily see that the HH and LL distributions are quite well separated from the LH distribution considering the voltage or current, respectively, therefore Alice and Bob can extract the key with high success rate of 99,98%. The eavesdropper (Eve) has no information, since the LH and HL states yield almost identical distribution.

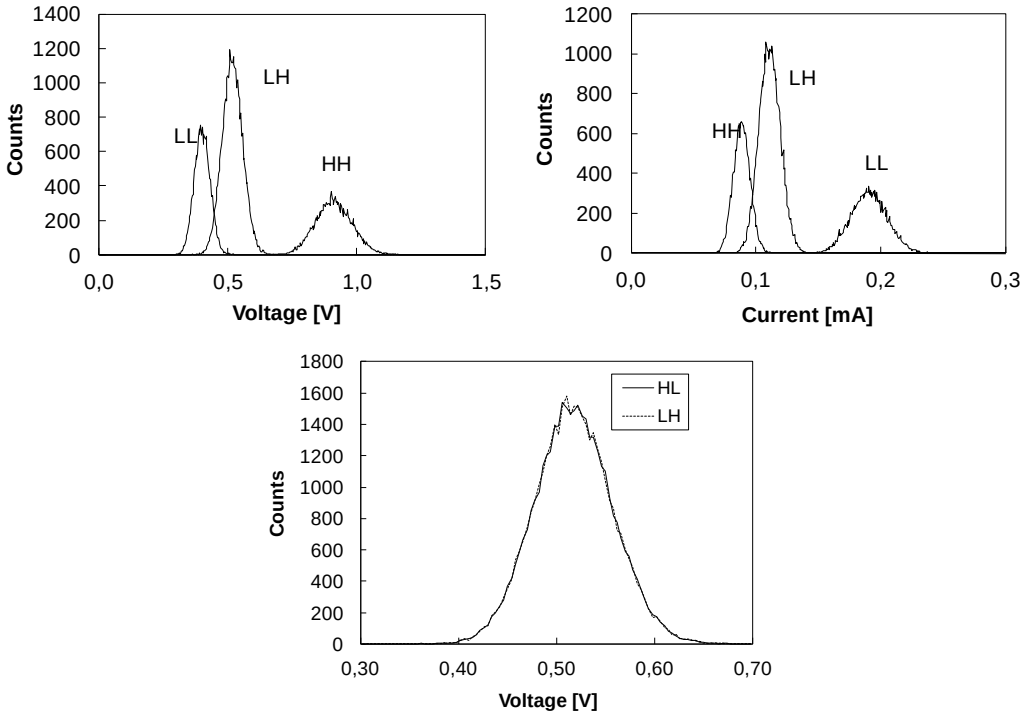

Figure 6.4. *Empirical voltage and current histograms seen by Alice and Bob (top left and top right, respectively) and voltage counts seen by Eve (bottom) at one end of the line for the two different secure bit arrangements (LH and HL) during the whole span of security checks utilizing 74497 clock cycles. It is obvious from the strong overlap of the two curves that Eve has virtually zero information even with fixed bit arrangement for 74497 clock cycles.*

Figure 6.5 shows the statistical data obtained during the exchange of a single bit.

Several attack tests were performed to check the security of the realized system including the Bergou- Scheuer-Yariv test utilizing wire resistance [9]; Hao's test [11]; Kish's tests based on of resistor inaccuracy and current pulse injection [4,12] and we have found no more than 0,19% of information leak.

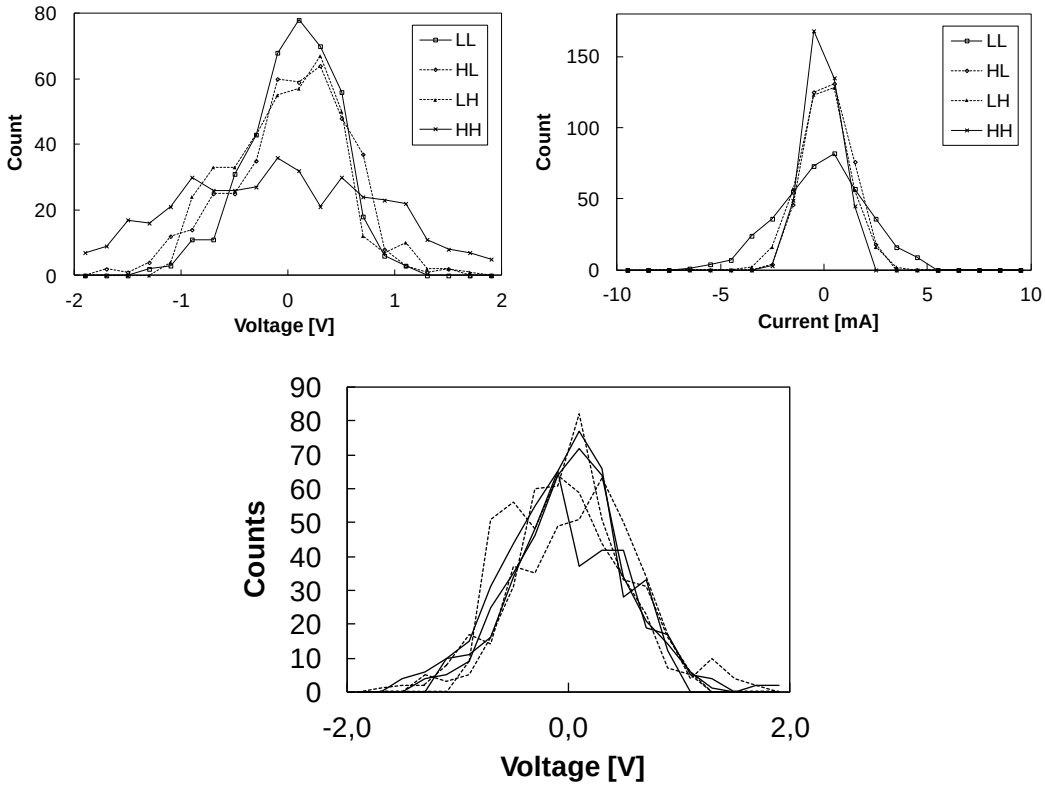

Figure 6.5. *Empirical histograms of the voltage and current counts seen by Alice and Bob (top left and top righ, respectively); voltage counts seen by Eve (bottom) at end of the line at the two different secure bit arrangements, LH and HL, three of each one. These functions correspond to the situation when the bit arrangement is fixed (LH or HL) and then the two distribution functions are the voltage counts measured at the two ends of the line to execute a Bergou- Scheuer-Yariv type of attack. The poor statistics seen in the top left and top right figures are enough for Alice and Bob to identify secure bit alignment with 0.02% error rate (99.98% fidelity). However when Eve tries to identify the bits from the two histogram recorded at the two ends of the line (bottom) she must work with these distributions which are very stochastic, almost identical and totally overlapping with a less than 1% shift of their centers [7] which results in 0.19% eavesdropped bit/transmitted secure bit.*

After the successful tests we have designed microcontroller based KLJN units in order to make the communicator units more compact. The units have a single mixed signal microcontroller with on-chip precision ADCs and DACs and some additional analog signal conditioning to scale the bipolar signals into the range of the single supply data converters. The USB port is used to connect to the host computer and power the units. The small switching units and model KLJN line is integrated on a small plug-in card printed circuit board. Figure 6.7 depicts the schematic and the photo of the units.

The tests of these units were successful, only a slight decrease in the communication speed was observed.

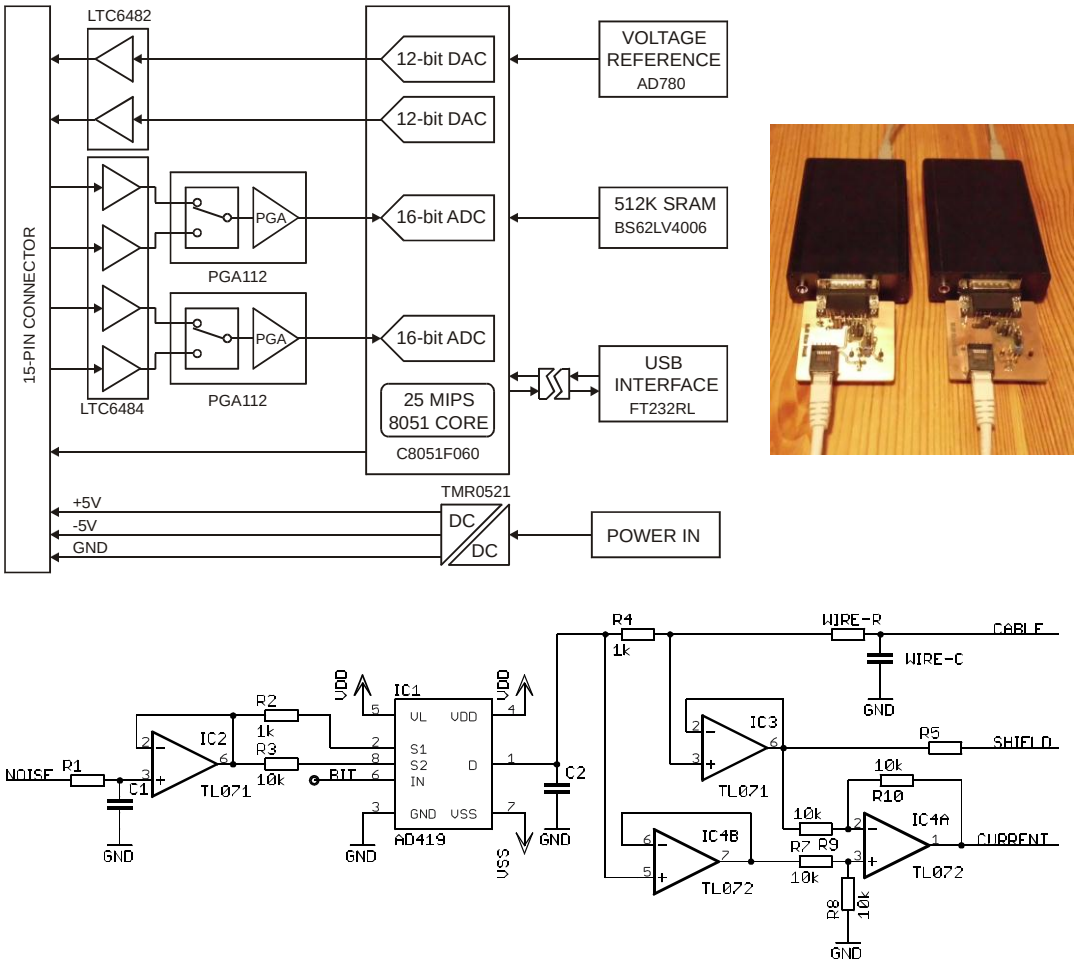

Figure 6.7. *Block diagram (top left) and photo (top right) of the compact microcontroller based KLJN communicator data acquisition and control unit. The simplified schematic of the KLJN switching and signal conditioning unit is shown at the bottom.*

6.5 Conclusions

We have developed DSP based units to realize the theoretically unconditionally secure Kirchhoff Loop Johnson Noise communication method. Our aim was to demonstrate the performance, to find the practical limitations of security and to make several security tests.

As a competitor of secure quantum communicators the KLJN system is much smaller, simpler and cheaper. We have carried out many experiments using our hardware and model communication line equivalent to lengths from 2km to 2000km. Our results indicate unrivalled fidelity and security levels among existing physical secure communicators. There are straightforward ways to improve security, fidelity and communication range further, such as proper choice of resistors, thicker cable, enhanced statistical tools for bit decision.

7 Summary and theses

The six chapters of this dissertation review my most important research results related to basic and applied noise research. The aim of the theoretical and experimental investigations, the analog and numerical simulations, the instrumentation hardware and related embedded and host computer software developments was to contribute to the knowledge of random processes and of the behavior of fluctuating systems. The emphasis was always on the efforts to find new ways in which noise can be used as an information source; how signal-to-noise ratio can be increased or in which we can use even noise as a tool to improve the operation of devices, to enhance the accuracy of measurement and to control and to optimize information transfer.

Most of the results were achieved in active cooperation with the members of my noise research group that I have been leading since 1997 and within the framework of various international and domestic collaborations. The following theses present my contribution to the work and are supported by 51 papers, 18 invited talks and 208 independent citations.

7.1 Theses

Thesis 1 – $1/f^{\alpha}$ noise generation and amplitude saturation

1. 1. I have designed a DSP based $1/f^{\alpha}$ noise generator that can provide power spectral density required over four decades of frequency with better than 1% accuracy. I have made the schematic and printed circuit board design and I have written the 16-bit fixed point ADSP-2105 and ADSP-2181 DSP source code using 9 first order infinite impulse response digital filters.
1. 2. I have discovered a special invariant property of Gaussian $1/f^{\alpha}$ fluctuations: for $\alpha \leq 1$, the power spectral density remains the same if the amplitude is saturated at various levels. Using numerical simulations I have also found the shape of the power spectral density for $1 < \alpha \leq 2$. My coworkers found theoretical explanation for the case of very small saturation levels which showed a good agreement with simulation results.
1. 3. I have extended simulation the results to saturation intervals that do not include the mean value.

This special invariance that occurs under wide range of conditions may help to understand the presence of 1/f noise in several systems and may also be related to its general occurrence. The development of the DSP noise generator is a direct exploitation of the results.

Publications:

3 journal papers [A2,A8,A9]
3 conference papers [A6, A7,A10]
2 invited talks [A7,A10]

Thesis 2 – Biased percolation modeling of electronic device degradation

2. 1. I have developed a numerical simulation framework for the percolation modeling of thermal degradation of thin film resistors. I have optimized the code to allow fast simulations of large two-dimensional resistor networks. I have also created a graphical user interface software version to allow visualization and more efficient analysis of the process.

2. 2. I have carried out numerical simulations to obtain the evolution of the sample resistance and normalized resistance fluctuation. I have found a significant difference compared to the regular percolation degradation and observed filamentary damage pattern and abruptly increasing noise that are in a good agreement with experimental results.
2. 3. I have calculated the power spectral density of the resistance fluctuations and found that the shape of 1/f noise changes significantly close to the breakdown.

The results help to understand the degradation process and may serve as a non-destructive predictor of failure of electronic devices. My collaborators (C. Pennetta and L. Reggiani, University of Lecce, Italy) extended the range of applications and published more than 30 papers about related research.

Publications:
6 journal papers [B2,B6,B8,B9,B11,B12]
7 conference papers [B1,B3,B4,B5,B7,B10,B13]
1 invited talk [B4]

Thesis 3 – DSP data acquisition and control system to support experimental noise research

I have developed a complete modular digital signal processor based data acquisition and control system to support various experiments related to noise research. I have designed a unique mixed-signal bus system for the modules, I have made all the schematic and printed circuit board designs, the embedded software development and I have also made several host computer applications in LabVIEW and C++ for the individual research tasks.

The Eurocard-standard system includes a 16-bit fixed point ADSP-2181 module and three mixed-signal modules with 14 to 16-bit data converters, up to 1MHz sample rate, simultaneous sampling capability and sigma-delta architecture ADCs, multiple DACs and multiplying DACs for fine amplitude control.

The system has been used in a wide range of experiments related to Thesis 1, Thesis 4, Thesis 5 and Thesis 6.

I have shown the system in an invited talk at HUNGELEKTRO 2002, 7th International Exhibition and Conference on Electronics Technology, Budapest, 23 April 2002 [C3]

Related publications (the results are achieved with the help of the system):
6 journal papers [A1,D7,D11,D19, D21,D22]
7 conference papers [A2,C1,C2,C5,D8,D15,D20]
8 invited talks [C3,C4,C6,D15,D16,D18,D19,D22]

Thesis 4 – High signal-to-noise ratio gain by stochastic resonance

4. 1. I supervised the numerical simulation work of the PhD student K. Lőrincz to obtain signal-to-noise ratio (SNR) gain data for stochastic resonance in the level-crossing detector. For small duty cycle periodic pulses we have got very high SNR gain above 10^4.
4. 2. I have developed a software framework and carried out numerical simulations to investigate the SNR gain in the Schmitt-trigger stochastic resonator. For asymmetric and symmetric periodic pulses I have obtained large SNR gain over 100.

4. 3. I have designed and built an analog computer to investigate the SNR gain in the archetypal dynamical stochastic resonance system. The experiments were carried out by the DSP system reported in Thesis 3. Using symmetric periodic pulses large SNR gain was obtained, close to 20.

4. 4. I have introduced the wide band SNR definition broadly used in engineering into the field of stochastic resonance and I have demonstrated the high SNR gain in bistable systems based on this definition.

4. 5. I proposed to investigate the role of the $1/f^{\kappa}$ colored noises in the mechanism of SNR gain in monostable and bistable systems and supervised the related numerical simulation work of my PhD student P. Makra. We clarified that 1/f noise does not play a special role as was proposed in the literature and we have shown that white noise provides better performance.

4. 6. I supervised the experimental work of my PhD student R. Mingesz to obtain SNR gain data for aperiodic and noisy signals using the analog computer and a DSP system mentioned in Thesis 3 and 4.3. We could show significant gain even for very irregular signals.

4. 7. I proposed to use randomly dithered time-to-digital conversion to enhance the control of excimer lasers for external and internal triggering modes. I led the design and realization of a microcontroller-based unit that uses software controlled delay elements and upgrades the old version with a significantly improved performance. Dithering improved the resolution by an order of magnitude using a simple and low cost solution using only a few integrated circuits and enhanced the quality of the control considerably.

The 165 citations (still about 10 citations per year) and 6 invited talks show significant impact of these results; several independent groups continued the research. I was a guest editor of a special issue [D21] of Fluctuation and Noise Letters and the chairman and co-chairman of international conferences related to the subject [D22,D23].

The developed experimental setups can easily aid exploitation and the microcontroller based system described in 4.7 can upgrade the older units already built into several excimer lasers.

Publications:

8 journal papers [D2,D7,D8,D10,D14, D17,D19,D20]
7 conference papers [D6,D9,D11,D13,D15,D16,D18]
6 invited talks [D7,D11,D12,D16,D17,D20]

Thesis 5 – Fluctuation-enhanced gas sensing

5. 1. I have developed a special measurement system for fluctuation enhanced sensing using carbon nanotube gas sensors. The system is based on the modules described in Thesis 3. Using the system we could demonstrate that the chemical selectivity of the sensor could be improved significantly.

5. 2. I have developed a numerical simulation framework to analyze the influence of the drift observed during data acquisition on the principal component analysis used to improve chemical selectivity. Comparing with the measured data it turned out that the drift does not affect the performance of the applied signal processing considerably.

5. 3. I have designed and built a compact USB port instrument and a low noise plug-in preamplifier module to support fluctuation enhanced sensing applications related to the European Union project called SANES (*Integrated Self-Adjusting Nano-Electronic Sensors*, for more information see http://cordis.europa.eu/).

The unit was successfully tested on carbon nanotube sensors and serves as a prototype for further application and exploitation.

5. 4. I have carried out numerical simulations to show that level-crossing statistics can be a much faster and simpler alternative to methods based on power spectral analysis for fluctuation enhanced sensing. The method is promising for embedded applications and stand-alone, battery powered wireless sensor nodes.

We plan to continue the development of the instrumentation and signal processing methods with our collaborators (L.B. Kish, Texas A&M University and Chiman Kwan, CEO of Signal Processing Inc.). I have designed and built a special instrument to support the measurement using the already available the National Institute of Standards and Technology (NIST) sensor modules. A phase 2 proposal will be submitted to NIST for further funding.

Publications:

7 journal papers [E3,E4,E6,E8,E10,E11,E12]
4 conference papers [E1,E2,E9,E13]
5 invited talks [E1,E5,E7,E9,E12]

Thesis 6 – Secure communication using thermal noise

I have built a DSP-based hardware system to support the realization of the Kirchhoff Loop Johnson (-like) Noise unconditionally secure communication and its experimental testing on a model communication line equivalent to lengths from 2km to 2000km. The system is based on the modules described in Thesis 3. I have also designed and built a dedicated compact, microcontroller-based USB device. This secure key exchange scheme is the only existing competitor of quantum key exchange. Our experiments show robustness, fidelity and security levels unprecedented among quantum communicators. The results inspired the development of another key exchange protocol [15-17 in the section 8.7].

Publications:

2 journal papers [F1,F3]
1 conference papers [F2]
1 plenary talk [F2]

7.2 Interdisciplinary applications and exploitation

I have already mentioned application and exploitation possibilities at the theses, here I focus on a wider range of applications. Using my experience in hardware/software development and signal processing – that I have acquired during my noise research projects – I have designed and built several computer controlled instruments for research, educational and industrial applications with 63 associated publications and 163 independent citations. Here the most important results are listed, more detailed information can be found on my personal pages [G1].

- I have designed PC (ISA bus) plug-in cards [G2,G3] and later DSP and microcontroller based instruments plus several data acquisition and analysis software applications for special ECG, blood pressure and respiration monitoring [G4]. Note that one of the aims is to measure heart rate and blood pressure fluctuations and apply statistical a spectral analysis that is also common in noise research [G5-G7]. My latest result is the development of a 128-channel ECG mapping hardware and software [G8]. I'm a coauthor of 56 medical publications – including an invited talk [G6] – that received 74 independent citations.

- I have developed DSP data acquisition and control systems to support photoacoustic measurements including laser diode driving, thermoelectric cooling, low-noise microphone signal conditioning, high-resolution data acquisition and embedded software development. A related publication [G9] has received 22 independent citations.
- I have developed DSP and microcontroller based instrument hardware and graphical user interface software for automatic titration projects. A publication [G10] with 32 independent citations and an international patent [G11] are related.
- I led the development of a special computer controlled system to measure the thermal and electric properties of conducting polypyrrole-silver nanocomposites. The associated publication [G12] received 35 independent citations.
- We have developed a high-precision, compact USB bacteriochlorophyll fluorometer hardware, embedded and graphical user interface software to support measurement of bacterial photosynthesis [G13,G14]. I would like to express my honor to my talented BSc student – my coworker on analog signal processing and embedded programming – Peter Kocsis, who has tragically died in 2012.
- I have developed several computer controlled instruments to support experimental education of physics, chemistry, biology and informatics. I have designed a sensor-to-USB interface [G15] with fully open source hardware, embedded software. I have also developed a graphical user interface Windows application, the open source C# code has been developed by my coauthor P. Makra. I have presented the results in an invited talk [G16]. Over 50 units were assembled and they are used in several secondary schools and also at the higher education. Note that the device has been used for accelerometer based signature recognition also [G17,G18] and I have upgraded my design with a 24-bit resolution sensor-to-USB interface useful in industrial applications also [G19]. I have contributed to engineering education with several other projects as well [G20,G21,C1,C2,C5].

Finally I note that my newest research topic is the so-called noise based logic that has been introduced in 2009 [G22-G25].

8 References

8.1 Publications of Z. Gingl

8.1.1 References for Chapter 1 (A1-A10)

[A1] Ambrózy A, Bánlaki P, **Gingl Z**, Kiss LB, Vajtai R, Trefán G, Hevesi I, $1/f^k$ noise generators based on computer random-walk. In: Ambrózy A (ed.) Noise in Physical Systems: Proc. of the 10th. International Conf. on Noise in Physical Systems. Budapest, Hungary, 21/07/1989-25/07/1989. Budapest: Academic Press, pp. 573-575.

[A2] Mingesz R, Bara P, **Gingl Z**, Makra P, Digital signal processor (DSP) based 1/f (a) noise generator. FLUCTUATION AND NOISE LETTERS 4:(4) pp. L605-L616. (2004)

[A3] Trefan G, Kiss LB, **Gingl Z**, Hevesi I, Torok IM, Diffusion noise generators realized by analog circuits. In: Ambrózy A (ed.) Noise in Physical Systems: Proc. of the 10th. International Conf. on NOISE in Physical Systems. Budapest, Hungary, 21/07/1989-25/07/1989. Budapest: Academic Press, pp. 569-572.

[A4] Kiss L B, **Gingl Z**, Márton Zs, Kertész J, Moss F, Schmera G, Bulsara A, 1/f noise in systems showing stochastic resonance. JOURNAL OF STATISTICAL PHYSICS 70:(1-2) pp. 451-462. (1993)

[A5] **Gingl Z**, Kiss LB, A Crucial Property of Gaussian 1/f Fluctuations. Proceedings of the 7th Vilnius Conferebnce on Fluctuation Phenomena in Physical Systems. Palanga, Lithuania, 04/10/1994-07/10/1994. Vilnius: pp. 274-279.(ISBN:9986-19-078-9)

[A6] **Gingl Z**, Kiss LB, Invariance of 1/f spectrum of Gaussian noises against amplitude-saturation nonlinearity. In: Doering Ch R, Kiss L B, Shlesinger M F (ed.) Proc. of the First International Conference on Unsolved Problems of Noise in Physics, Biology, Electronic Technology and Information Technology, UPoN'96. Szeged, Hungary, 1997 World Scientific, pp. 337-342.

[A7] **Gingl Zoltan**, Ishioka Shunya, Choi Donghak, Fuchikami Nobuko, Theoretical and experimental results concerning the amplitude truncation of Gaussian 1/f[sup alpha] noises. In: Abbott Derek, Kish Laszlo B (ed.) AIP Conference Proceedings: UNSOLVED PROBLEMS OF NOISE AND FLUCTUATIONS. Adelaide, Australia, 12/07/1999-15/07/1999. (511) American Institute of Physics, pp. 136-143.

[A8] Ishioka S, **Gingl Z**, Choi D, Fuchikami N, Amplitude truncation of Gaussian 1/f(alpha) noises. PHYSICS LETTERS A 269:(1) pp. 7-12. (2000)

[A9] **Gingl Z**, Ishioka S, Choi D, Fuchikami N, Amplitude truncation of Gaussian 1/f(alpha) noises: Results and problems. CHAOS 11:(3) pp. 619-623. (2001)

[A10] **Gingl Z**, Mingesz R, Makra P, On the Amplitude and Time-structure Properties of 1/f[sup alpha] Noises. In: Bezrukov Sergey M (ed.) AIP Conference Proceedings: UNSOLVED PROBLEMS OF NOISE AND FLUCTUATIONS. Washington, United States of America, 02/07/2002-06/07/2002. (665) American Institute of Physics, pp. 578-583.

8.1.2 References for Chapter 2 (B1-B14)

[B1] **Gingl Z**, Pennetta C, Kiss LB, Reggiani L, An extended analysis of noise and resistance degradation within the biased percolation model. In: Claeys C,

Simoen E (ed.) Third ELEN Workshop. Leuven, Belgium, 05/11/1996-07/11/1996. pp. 114-119.

[B2] **Gingl Z**, Pennetta C, Kiss LB, Reggiani L, Biased percolation and abrupt failure of electronic devices. SEMICONDUCTOR SCIENCE AND TECHNOLOGY 11:(12) pp. 1770-1775. (1996)

[B3] **Gingl Z**, Pennetta C, Kiss L B, Reggiani L, A biased percolation model for the analysis of electronic-device degradation. In: Stojadinovic N (ed.) 21st International Conference on Microelectronics: Vol.2. Nis, Yugoslavia, 14/09/1997-17/09/1997. (2) pp. 651-654.(ISBN:0-7803-3664-X)

[B4] **Gingl Z**, Pennetta C, Kiss LB, Reggiani L, Biased percolation and noise analysis of electrical breakdown. In: Proccedings of the 14 International Conference on Noise in Physical Systems and Fluctuations (ICNF97). Leuven, Belgium, 14/07/1997-18/07/1997. pp. 409-414.

[B5] Pennetta C, **Gingl Z**, Kiss LB, Reggiani L, A numerical simulation of excess noise for degradation and failure of thin film resistors. In: Proccedings of the 14 International Conference on Noise in Physical Systems and Fluctuations (ICNF97). Leuven, Belgium, 14/07/1997-18/07/1997. pp. 419-422.

[B6] Pennetta C, **Gingl Z**, Kiss LB, Reggiani L, Biased percolation and electrical breakdown. SEMICONDUCTOR SCIENCE AND TECHNOLOGY 12:(9) pp. 1057-1063. (1997)

[B7] Pennetta C, **Gingl Z**, Kiss LB, Reggiani L, Noise, Biased percolation and Abrupt Failure of Electronic Devices. In: Doering Ch R, Kiss L B, Shlesinger M F (ed.) Proc. of the First International Conference on Unsolved Problems of Noise in Physics, Biology, Electronic Technology and Information Technology, UPoN'96. Szeged, Hungary, 1997 World Scientific, pp. 87-91.

[B8] **Gingl Z**, Pennetta C, Kiss LB, Reggiani L, Biased percolation model for the analysis of electronic-device degradation. MICROELECTRONICS RELIABILITY 38:(4) pp. 515-521. (1998)

[B9] Pennetta C, **Gingl Z**, Kiss LB, Reggiani L, De Vittorio M, Cola A, Mazzer M, A percolative simulation of dielectric-like breakdown. MICROELECTRONICS RELIABILITY 38:(2) pp. 249-253. (1998)

[B10] Pennetta C, Reggiani L, **Gingl Z**, Kiss LB, A percolative study of electrical breakdown. In: Fiorentini V, Meloni F (ed.) PROCEEDINGS OF THE VII ITALIAN-SWISS WORKSHOP ADVANCES IN COMPUTATIONAL MATERIALS SCIENCE II. Cagliari, Italy, 19/09/1997-23/09/1997. pp. 87-94.

[B11] Pennetta C, Kiss LB, **Gingl Z**, Reggiani L, Excess thermal-noise in the electrical breakdown of random resistor networks. EUROPEAN PHYSICAL JOURNAL B 12:(1) pp. 61-65. (1999)

[B12] Pennetta C, Kiss LB, **Gingl Z**, Reggiani L, A noise temperature analysis of the electrical degradation of thin nanostructured films. JOURNAL OF NANOPARTICLE RESEARCH 2:(1) pp. 97-101. (2000)

[B13] Kish Laszlo B, Penetta Cecilia, **Gingl Zoltan**, Biased percolation approach to failure propagation in nanostructures and prediction of the total failure by electronic noise analysis. In: Cao Guozhong, Kirk Wiley P (ed.) Nanoscale Optics and Applications. Seattle, United States of America, 01/11/2002-04/11/2002. (4809) SPIE, pp. 217-221.

[B14] http://www.inf.u-szeged.hu/~gingl/achievements/biasperc

8.1.3 References for Chapter 3 (C1-C7)

[C1] **Gingl Zoltán**, Kántor Zoltán, Intelligent General Purpose Data Acquisition Units For Student Labs. In: Pacher Pál, Pipek János (ed.) Proceedings of the Second European Conference on Physics Teaching In Engineering Education (PTEE 2000). Budapest, Hungary, 14/06/2000-17/06/2000. Budapest University of Technology and Economics, pp. P23/1-P23/5. Paper 23.

[C2] **Gingl Zoltán**, Kántor Zoltán, Virtual Measurement Technology In The Education Of Physicists And Communication Engineers. In: Pacher Pál, Pipek János (ed.) Proceedings of the Second European Conference on Physics Teaching In Engineering Education (PTEE 2000). Budapest, Hungary, 14/06/2000-17/06/2000. Budapest University of Technology and Economics, pp. P57/1-P57/6. Paper 57.

[C3] **Gingl Zoltán**, Kántor Zoltán, Mingesz Róbert, A DAS1414 általános célú intelligens adatgyűjtő és vezérlő egység és alkalmazásai. HUNGELEKTRO 2002, 7th International Exhibition and Conference on Electronics Technology, Budapest, 23 April 2002., www.muszeroldal.hu (2002)

[C4] **Gingl Zoltán**, Kántor Zoltán Virtuális méréstechnika a kísérletező oktatásban. p. 348. Program tartalmi összefoglalók, II. Orszagos Nevelestudomanyi Konferencia, MTA Pedagogiai Bizottsaga, Budapest Október 24-26. (2002)

[C5] Kantor Z, **Gingl Z**, Virtual instruments perform real experiments in the physics class. In: Physics Teaching in Engineering Education PTEE 2002. Leuven, Belgium, 05/06/2002-07/06/2002. Paper 1. (ISBN:90-5682-359-0)

[C6] **Gingl Z**, Real measurements using virtual measurement techniques. Invited talk at 11th Workshop on Multimedia in Physics Teaching and Learning University of Szeged 20-22 September 2006 (2006)

[C7] http://www.inf.u-szeged.hu/~gingl/achievements/DAS1414/

8.1.4 References for Chapter 4 (D1-D23)

[D1] **Gingl Z**, Kiss LB, Moss F, Non-dynamical stochastic resonance: Theory and experiments with white and arbitrarily coloured noise. EUROPHYSICS LETTERS 29:(3) pp. 191-196. (1995)

[D2] Loerincz K, **Gingl Z**, Kiss LB, A stochastic resonator is able to greatly improve signal-to-noise ratio. PHYSICS LETTERS A 224:(1-2) pp. 63-67. (1996)

[D3] Lorincz K, Balazsi G, **Gingl Z**, Kiss LB, Stochastic resonance at phase noise. In: Doering Ch R, Kiss L B, Shlesinger M F (ed.) Proc. of the First International Conference on Unsolved Problems of Noise in Physics, Biology, Electronic Technology and Information Technology, UPoN'96. Szeged, Hungary, 1997 World Scientific, pp. 223-228.

[D4] Loerincz K, **Gingl Z**, Kiss LB, Bulsara AR, Higher order stochastic resonance in a level-crossing detector. PHYSICS LETTERS A 254:(3-4) pp. 154-157. (1999)

[D5] **Gingl Z**, Vajtai R, Kiss LB, A self-adaptive stochastic resonator with logarithmic transfer. CHAOS SOLITONS & FRACTALS 11:(12) pp. 1933-1935. (2000)

[D6] Fulei Tamas, **Gingl Zoltan**, Makra Peter, Mechanism of signal-to-noise ratio gain in a monostable threshold stochastic resonators. In: Schimansky-Geier Lutz, Abbott Derek, Neiman Alexander, Van den Broeck Christian (ed.) Noise in Complex Systems and Stochastic Dynamics. Santa Fe, United States of America, 08/05/2003-11/05/2003. (5114) SPIE, pp. 327-334.

[D7] **Gingl Z**, Vajtai R, Kiss LB, Signal-to-noise ratio gain by stochastic resonance in a bistable system. CHAOS SOLITONS & FRACTALS 11:(12) pp. 1929-1932. (2000)

[D8] **Gingl Z**, Makra P, Vajtai R, High signal-to-noise ratio gain by stochastic resonance in a double well. FLUCTUATION AND NOISE LETTERS 1:(3) pp. L181-L188. (2001)

[D9] **Gingl Z**, Vajtai R, Makra P, High signal-to-noise ratio gain by stochastic resonance in a double well. In: Bosman G (ed.) Proceedings of the 16th International Conference on Noise in Physical Systems and 1/f Fluctuations (ICNF 2001). Gainesville, United States of America, 22/10/2001-25/10/2001. Singapore: World Scientific, pp. 545-548.(ISBN:981-02-4677-3)

[D10] Makra P, **Gingl Z**, Kish LB, Signal-to-noise ratio gain in non-dynamical and dynamical bistable stochastic resonators. FLUCTUATION AND NOISE LETTERS 2:(3) pp. L147-L155. (2002)

[D11] Makra Peter, **Gingl Zoltan**, A Dynamical System Exhibits High Signal-to-noise Ratio Gain by Stochastic Resonance. In: Bezrukov Sergey M (ed.) AIP Conference Proceedings: UNSOLVED PROBLEMS OF NOISE AND FLUCTUATIONS. Washington, United States of America, 02/07/2002-06/07/2002. (665) American Institute of Physics, pp. 100-108.

[D12] Makra P, **Gingl Z**, Mingesz R Signal-to-noise ratio gain by stochastic resonance and its possible applications. Invited talk at International Workshop on Stochastic Resonance: New Horizons in Physics and Engineering Dresden 4–7 October 2004 (2004)

[D13] **Gingl Z**, Makra P, Fulei T, Vajtai R, Mingesz R, Colored noise driven stochastic resonance in a double well and in a Fitzhugh-Nagumo neuronal model. In: Bosman G (ed.) Proceedings of the 16th International Conference on Noise in Physical Systems and 1/f Fluctuations (ICNF 2001). Gainesville, United States of America, 22/10/2001-25/10/2001. Singapore: World Scientific, pp. 420-423.(ISBN:981-02-4677-3)

[D14] Makra P, **Gingl Z**, Fulei T, Signal-to-noise ratio gain in stochastic resonators driven by coloured noises. PHYSICS LETTERS A 317:(3-4) pp. 228-232. (2003)

[D15] Makra Peter, **Gingl Zoltan**, Fulei Tamas, Signal-to-noise ratio gain in stochastic resonators driven by colored noises. In: Gingl Z, Sancho JM, Schimansky-Geier L, Kertesz J (ed.) Noise in Complex Systems and Stochastic Dynamics II. Mapalomas, Spain, 25/05/2004-28/05/2004. (5471) SPIE, pp. 213-221. (ISBN:9780819453938)

[D16] Mingesz Robert, Makra Peter, **Gingl Zoltan**, Cross-spectral analysis of signal improvement by stochastic resonance in bistable systems (Invited Paper). In: Kish Laszlo B, Lindenberg Katja, Gingl Zoltan (ed.) Noise in Complex Systems and Stochastic Dynamics III. Austin, United States of America, 23/05/2005-26/05/2005. (5845) SPIE, pp. 283-292. (ISBN:9780819458407)

[D17] Mingesz R, **Gingl Z**, Makra P, Marked signal improvement by stochastic resonance for aperiodic signals in the double-well system. EUROPEAN PHYSICAL JOURNAL B 50:(1-2) pp. 339-344. (2006)

[D18] Mingesz Robert, **Gingl Zoltan**, Almasi Gabor, Makra Peter, Utilising jitter noise in the precise synchronisation of laser pulses. In: Macucci Massimo, Vandamme Lode K, Ciofi Carmine, Weissman Michael B (ed.) Noise and Fluctuations in Circuits, Devices, and Materials. Florence, Italy, 07/06/2007-10/06/2007. (6600) SPIE, pp. 66000Z-8.

[D19] Mingesz R, **Gingl Z**, Almasi G, Csengeri A, Makra P, Utilising jitter noise in the precise synchronisation of laser pulses. FLUCTUATION AND NOISE LETTERS 8:(1) pp. L41-L49. (2008)

[D20] Mingesz R, Barna A, **Gingl Z**, Mellár J, Enhanced control of excimer laser pulse timing using tunable additive noise. FLUCTUATION AND NOISE LETTERS 11:(1) (2012), *in press.* e-print: http://arxiv.org/abs/1109.2632

[D21] **Gingl Z** (ed.) Fluctuation and Noise Letters.: Special Issue on Stochastic Resonance I: Fundamental and Special Aspects. FLUCTUATION AND NOISE LETTERS 2:(3) Singapore: World Scientific, (2002).

[D22] **Gingl Z**, Sancho JM, Schimansky-Geier L, Kertesz J (ed.) Noise in Complex Systems and Stochastic Dynamics II. (5471) Mapalomas, Spain, 2004.05.25-2004.05.28. SPIE, 2004. 660 p.

[D23] Kish Laszlo B, Lindenberg Katja, **Gingl Zoltan** (ed.) Noise in Complex Systems and Stochastic Dynamics III. (5845) Austin, USA, 2005.05.23-2005.05.26. SPIE, 2005. 328 p.

8.1.5 References for Chapter 5 (E1-E13)

[E1] Kish Laszlo B, Mingesz Robert, **Gingl Zoltan**, Schmera Gabor, Smulko Janusz, Kwan Chiman, Heszler Peter, Granqvist Claes-Goran, Novel Applications of Noise in Sensing and Communications. In: Tacano Munecazu, Yamamoto Yoshiharu, Nakao Mitsuyuki (ed.) NOISE AND FLUCTUATIONS: 19th International Conference on Noise and Fluctuations - ICNF 2007. Tokyo, Japan, 09/07/2007-14/07/2007. (922) American Institute of Physics, pp. 405-410. (AIP Conference Proceedings; 922.)(ISBN:978-0-7354-0432-8)

[E2] Kish LB, Solis J, Vajtai R, Granqvist C-G, Marlow W, Olsson J, Schnurer J, Lantto V, **Gingl Z**, How can noise 'smell' and remember that 'smell': sampling-and-hold electronic nose. In: Bosman G (ed.) Proceedings of the 16th International Conference on Noise in Physical Systems and 1/f Fluctuations (ICNF 2001). Gainesville, United States of America, 22/10/2001-25/10/2001. Singapore: World Scientific, pp. 779-782.(ISBN:981-02-4677-3)

[E3] Haspel H, Ionescu R, Heszler P, Kukovecz A, Konya Z, **Gingl Z**, Maklin J, Mustonen T, Kordas K, Vajtai R, Ajayan PM, Fluctuation enhanced gas sensing on functionalized carbon nanotube thin films. PHYSICA STATUS SOLIDI B-BASIC RESEARCH 245:(10) pp. 2339-2342. (2008)

[E4] Heszler P, **Gingl Z**, Mingesz R, Csengeri A, Haspel H, Kukovecz A, Konya Z, Kiricsi I, Ionescu R, Maklin J, Mustonen T, Toth G, Halonen N, Kordas K, Vahakangas J, Moilanen H, Drift effect of fluctuation enhanced gas sensing on carbon nanotube sensors. PHYSICA STATUS SOLIDI B-BASIC RESEARCH 245:(10) pp. 2343-2346. (2008)

[E5] Kukovecz A, Heszler P, Kordas K, Roth S, Konya Z, Haspel H, Ionescu R, Sapi A, Maklin J, Mohl M, **Gingl Z**, Vajtai R, Kiricsi I, Ajayan PM, Improving the performance of functionalized carbon nanotube thin film sensors by fluctuation enhanced sensing. In: Proccedings of SPIE Optics + Photonics 2008. San Diego, United States of America, 10/08/2008-14/08/2008. pp. 70370Y/1-70370Y10.

[E6] Maklin J, Mustonen T, Halonen N, Toth G, Kordas K, Vahakangas J, Moilanen H, Kukovecz A, Konya Z, Haspel H, **Gingl Z**, Heszler P, Vajtai R, Ajayan PM, Inkjet printed resistive and chemical-FET carbon nanotube gas sensors. PHYSICA STATUS SOLIDI B-BASIC RESEARCH 245:(10) pp. 2335-2338. (2008)

[E7] **Gingl Zoltán**, Fluktuációkkal javított gázérzékelés szén nanocsövekkel és más szenzorokkal. Integrált Mikro/Nanorendszerek Nemzeti Technológiai Platform konferencia, 2009. március 27., Budapest (2009)

[E8] Kukovecz Á, Molnár D, Kordás K, **Gingl Z**, Moilanen H, Mingesz R, Kónya Z, Mäklin J, Halonen N, Tóth G, Haspel H, Heszler P, Mohl M, Sápi A, Roth S, Vajtai R, Ajayan P M, Pouillon Y, Rubio A, Kiricsi I, Carbon nanotube based sensors and fluctuation enhanced sensing. PHYSICA STATUS SOLIDI C-CURRENT TOPICS IN SOLID STATE PHYSICS 7:(3-4) pp. 1217-1221. (2010)

[E9] Molnar D, Heszler P, Mingesz R, **Gingl Z**, Kukovecz A, Konya Z, Haspel H, Mohl M, Sapi A, Kiricsi I, Kordas K, Maklin J, Halonen N, Toth G, Moilanen H, Roth S, Vajtai R, Ajayan PM, Pouillon Y, Rubio A, Increasing chemical selectivity of carbon nanotube-based sensors by fluctuation-enhanced sensing. FLUCTUATION AND NOISE LETTERS 9:(3) pp. 277-287. (2010)

[E10] Mingesz R, **Gingl Z**, Kukovecz A, Konya Z, Kordas K, Moilanen H, Compact USB measurement and analysis system for real-time fluctuation enhanced sensing. In: Deen MJ, Kasap S (ed.) Proceedings of the 21st International Conference on Noise and Fluctuations. Toronto, Canada, 12/06/2011-16/06/2011. IEEE, pp. 385-388.(ISBN:978-1-4577-0189-4)

[E11] Kish L, Chang H, King M, Kwan C, Jensen J, Schmera G, Smulko J, **Gingl Z**, Granqvist C, Fluctuation-Enhanced Sensing for Biological Agent Detection and Identification. IEEE TRANSACTIONS ON NANOTECHNOLOGY 10:(6) pp. 1238-1242. (2011)

[E12] **Gingl Z**, Kish LB, Ayhan B, Kwan C, Granqvist CG, Fluctuation-Enhanced Sensing With Zero-Crossing Analysis for High-Speed and Low-Power Applications. IEEE SENSORS JOURNAL 10:(3) pp. 492-497. (2010)

[E13] Schmera G, **Gingl Z**, Kish LB, Ayhan B, Kwan C, Granqvist CG, Separating Chemical Signals of Adsorption-Desorption and Diffusive Processes. IEEE SENSORS JOURNAL 10:(3) pp. 461-464. (2010)

8.1.6 References for Chapter 6 (F1-F3)

[F1] Kish L, Mingesz R, **Gingl Z**, Unconditionally secure communication via wire. SPIE Newsroom, Optoelectronics & Communications (2007)

[F2] Kish Laszlo B, Mingesz Robert, **Gingl Zoltan**, Thermal noise informatics: totally secure communication via a wire, zero-power communication, and thermal noise driven computing. In: Macucci Massimo, Vandamme Lode K, Ciofi Carmine, Weissman Michael B (ed.) Noise and Fluctuations in Circuits, Devices, and Materials. Florence, Italy, 07/06/2007-10/06/2007. (6600) SPIE, pp. 660003-660013.

[F3] Mingesz R, **Gingl Z**, Kish LB, Johnson(-Iike)-Noise-Kirchhoff-loop based secure classical communicator characteristics, for ranges of two to two thousand kilometers, via model-line. PHYSICS LETTERS A 372:(7) pp. 978-984. (2008)

8.1.7 Publications related to interdisciplinary applications (G1-G18)

[G1] http://www.inf.u-szeged.hu/~gingl/achievements/

[G2] Kardos A, **Gingl Z**, A szisztémás vérnyomás és pulzusvariabilitás folyamatos, nem invazív, on-line vizsgálata emberben. CARDIOLOGIA HUNGARICA 2: pp. 39-51. (1994), http://www.inf.u-szeged.hu/~gingl/achievements/COMONOBHV/

[G3] Kardos A, Rudas L, Simon J, **Gingl Z**, Csanady M, Effect of postural changes on arterial baroreflex sensitivity assessed by the spontaneous sequence method and Valsalva manoeuvre in healthy subjects. CLINICAL AUTONOMIC RESEARCH 7:(3) pp. 143-148. (1997)

[G4] http://www.inf.u-szeged.hu/~gingl/achievements/WSMon/

[G5] Szili-Török T, Gingl Z, Kardos A, Halmai L, Rudas L, Windowed FFT – a time-variant spectral analysis: applicability during the head-up tilt test. JOURNAL OF CLINICAL AND BASIC CARDIOLOGY 2: pp. 241-244. (1999)

[G6] Gingl Z, Makra P, Rudas L, Zollei E, Csik N, Spectral analysis problems of heart rate and blood pressure fluctuations. FLUCTUATION AND NOISE LETTERS 7:(2) pp. L143-L150. (2007)
Based on an invited talk presented at the conference Unsolved Problems of Noise, Gallipolli, Italy, 2005

[G7] Sághy László, Vassil Borislavov Traykov, **Gingl Zoltán**, Pap Róbert, Forster Tamás, Frekvenciaanalízis pitvarfibrillációban. CARDIOLOGIA HUNGARICA 39:(3) pp. 229-235. (2009)

[G8] http://www.inf.u-szeged.hu/~gingl/achievements/WSMon/

[G9] Bozóki Z, Sneider J, **Gingl Z**, Mohácsi Á, Szakáll M, Bor Zs, Szabó G, A high-sensitivity, near-infrared tunable-diode-laser-based photoacoustic water-vapour-detection system for automated operation. MEASUREMENT SCIENCE & TECHNOLOGY 10: pp. 999-1003. (1999) http://www.inf.u-szeged.hu/~gingl/achievements/PADL/

[G10] E Tombácz, G Filipcsei, M Szekeres, **Z Gingl**, Particle aggregation in complex aquatic systems. COLLOIDS AND SURFACES A-PHYSICOCHEMICAL AND ENGINEERING ASPECTS 151: pp. 233-244. (1999) http://www.inf.u-szeged.hu/~gingl/achievements/GIMET/

[G11] Szekeres Márta, Fülei Tamás, **Gingl Zoltán**, Tombácz Etelka, Dékány Imre, PROCESS FOR PH-CONTROL AND STOICHIOMETRIC PH-STAT MEAN. Patent ID: 0600636 Publication year: 2008, http://worldwide.espacenet.com

[G12] E Pintér, R Patakfalvi, T Fülei, **Z Gingl**, I Dékány, Cs Visy, Characterization of polypyrrole-silver nanosomposites. Prepared int he presence of different dopants. JOURNAL OF PHYSICAL CHEMISTRY B - CONDENSED MATTER MATERIALS SURFACES INTERFACES AND BIOPHYSICAL 109:(37) pp. 17474-17478. (2005)

[G13] Kocsis P, Asztalos E, **Gingl Z**, Maroti P, Kinetic bacteriochlorophyll fluorometer. PHOTOSYNTHESIS RESEARCH 105:(1) pp. 73-82. (2010) http://www.inf.u-szeged.hu/~gingl/achievements/kbf/

[G14] Asztalos E, **Gingl Z**, Maróti P, Field instrument for determination of the photosynthetic capacity of intact photosynthetic bacteria. EUROPEAN BIOPHYSICS JOURNAL 40:(Supplement 1) p. 174. (2011)

[G15] Kopasz K, Makra P, **Gingl Z**, Edaq530: a transparent, open-end and open-source measurement solution in natural science education. EUROPEAN JOURNAL OF PHYSICS 32: pp. 491-504. (2011), http://www.inf.u-szeged.hu/~gingl/achievements/EDAQ530/

[G16] **Gingl Z**, Makra P, Kopasz K, Thumb-size USB-to-sensor interface supports efficient experimentation in multilevel education of physics and other disciplines. EUPEN's 12th General Forum - EGF2010, "NEW WAYS OF TEACHING PHYSICS", Paris (France): 2-5 September (2010)

[G17] Csirik J, **Gingl Z**, Griechisch E, The effect of training data selection and sampling time intervals on signature verification. In: First International Workshop on Automated Forensic Handwriting Analysis (AFHA 2011). Beijing, China, 17/09/2011-18/09/2011.

[G18] Bunke Horst, Csirik János, **Gingl Zoltán**, Griechisch Erika, Online Signature Verification Method Based on the Acceleration Signals of Handwriting Samples. LECTURE NOTES IN COMPUTER SCIENCE 7042: pp. 499-506. (2011)

[G19] **Gingl Z**, Fabricate a high-resolution sensor-to-USB interface. EDN 56:(22) pp. 54-57. (2011), http://www.inf.u-szeged.hu/~gingl/edaq24/

[G20] **Gingl Z** and Kocsis P, Measure resistance and temperature with a sound card. EDN 56:(10) pp. 58-59. (2011)

[G21] **Gingl Z,** A photoplethysmograph experiment for microcontroller labs. INTERNATIONAL JOURNAL OF ELECTRICAL ENGINEERING EDUCATION 49: pp. 1-19. (2012), in press

[G22] Kish LB, Bezrukov SM, Khatri SP, **Gingl Z**, Sethuraman S, Noise-Based Logic and Computing: From Boolean Logic Gates to Brain Circuitry and Its Possible Hardware Realization. In: Peper F, Umeo H, Matsui N, Isokawa T (ed.) Natural Computing, Proceedings in Information and Communications Technology. Himeji, Japan, 2009.09.22-2009.09.26.

[G23] Kish LB, Khatri S, Bezrukov S, Peper F, **Gingl Z**, Horvath T, Noise-based information processing: Noise-based logic and computing: What do we have so far? In: Deen MJ, Kasap S (ed.) Proceedings of the 21st International Conference on Noise and Fluctuations. Toronto, Canada, 2011.06.12-2011.06.16. IEEE, pp. 28-33.(ISBN:978-1-4577-0189-4)

[G24] Kish LB, Khatri SP, Bezrukov SM, Peper F, **Gingl Z**, Horvath T, Noise-based deterministic logic and computing: a brief survey. INTERNATIONAL JOURNAL OF UNCONVENTIONAL COMPUTING 7:(1-2) pp. 101-113. (2011)

[G25] **Gingl Z**, Kish LB, Khatri SP, Towards brain-inspired computing. FLUCTUATION AND NOISE LETTERS 9:(4) pp. 403-412. (2010)

8.2 References for Chapter 1

[1] Johnson JB,The Schottky effect in low frequency circuits, PHYSICAL REVIEW, 26:71-85 (1925)

[2] Schottky W, Small-shot effect and flicker effect, PHYSICAL REVIEW, 28:74-103. (1926)

[3] Maes HE, Usmani SH, 1/f noise in thin oxide p-channel metal-nitride-oxide-silicon transistors. JOURNAL OF APPLIED PHYSICS 54:(4), pp. 1937-1949. (1983)

[4] Garfunkel, GA, Weissman MB, 1/f noise and the field effect in gated resistors. JOURNAL OF APPLIED PHYSICS 57:(2), pp. 634-636. (1985)

[5] Kiss LB, Svedlindh P, Noise in high Tc superconductors. IEEE TRANSACTIONS ON ELECTRON DEVICES 41:(11), pp. 2112-2122. (1994)

[6] Fronen RJ, Vandamme LKJ, Low-frequency intensity noiae in semiconductor lasers. IEEE JOURNAL OF QUANTUM ELECTRONICS 24:(5), pp. 724-736. (1988)

[7] Fronen RJ, Facet reflectivity and low-frequency noise in the light output of LED and superradiant diodes. IEEE JOURNAL OF QUANTUM ELECTRONICS 25:(7), pp. 1653-1658. (1989)

[8] Nolan PL et al, Rapid variability of 10-140keV X-rays from Cygnus X-1. ASTROPHYSICS JOURNAL 246, pp. 494-501. (1981)

[9] Musha T, Takeuchi H, Inoue T, 1/f Fluctuations in the spontaneous spike discharge intervals of a giant snail neuron. IEEE TRANSACTIONS ON BIOMEDICAL ENGINEERING 30:(3), pp. 194-197. (1983)

[10] Musha T, Higuchi H, The 1/f fluctuation of a traffic current on an expressway. JAPANESE JOURNAL OF APPLIED PHYSICS 15:(7), pp. 1271-1275. (1976)

[11] Mandelbrot B B, Wallis JR, Some long-run properties of geophysical records. WATER RESOURCES RESEARCH, 5:(2) pp.321-340 (1969)

[12] Voss RF, Clarke J, '1/f noise' in music and speech. NATURE 258:(5533), pp. 317-318. (1975)

[13] Kobayashi M, Musha T, 1/f fluctuation of heartbeat period, IEEE TRANSACTION OF BIOMEDICAL ENGINEERING, 29 pp. 456-457. (1982)

[14] Singer DH, Martin GJ, Magid N, Weiss JS, Schaad JW, Kehoe R, Zheutlin T, Fintel DJ, Hsieh AM, Lesch M, Low heart rate variability and sudden cardiac death. JOURNAL OF ELECTROCARDIOLOGY 21 p S46 (1988)

[15] Dutta P, Horn PM, Low frequency fluctuations in solids: 1/f noise. REVIEWS OF MODERN PHYSICS, 53: (3) pp. 497-516 (1981)
M. S. Keshner, 1/f noise, Proc. IEEE, vol. 70, no. 1, pp. 212–218, (1982)

[16] Kasdin NJ, Discrete simulation of colored noise and stochastic processes and $1/f^{\alpha}$ power law noise generation, Proceedings of the IEEE, 83:(5) pp. 802-827 (1995)

[17] Narasimha R, Bandi SP, Rao RM, Mukund PR, 1/f noise synthesis model in discrete-time for circuit simulation, IEEE TRANSACTIONS ON CIRCUITS AND SYSTEMS I, 52:(6) pp.1104-1114 (2005)

[18] Murao K, Kohda T, Noda K, Yanase M, 1/f noise generator using logarithmic and antilogarithmic amplifiers, IEEE TRANSACTIONS ON CIRCUITS AND SYSTEMS I: Fundamental Theory and Applications, 39:(10) pp. 851-853 (1992)

[19] Knuth D E, The Art of Computer Programming, Volume 2: Seminumerical Algorithms, Third ed. Addison-Wesley, 1997, ISBN-13: 978-0201896848

[20] L'Ecuyer P, Tables of maximally equidistributed combined LFSR generators. MATHEMATICS OF COMPUTATION 68:(225), pp. 261–269. (1999)

[21] Panneton F, L'Ecuyer P, Matsumoto M, Improved long-period generators based on linear recurrences modulo 2. ACM TRANSACTIONS ON MATHEMATICAL SOFTWARE 32:(1) pp.1-16. (2006)
[22] Richardson JM, The linear theory of fluctuations arising from diffusional mechanisms - An attempt at a theory of contact noise. BELL SYSTEMS TECHNOLOGY JOURNAL 29, pp. 117-141. (1950)
[23] Bernamont J, Fluctuations de potential aux bornes d'un conducteur metallique de faible volume parcouru par un courant, ANNALEN DER PHYSIK (Leipzig) 7, pp. 71–140. (1937)
[24] Van der Ziel A, On the noise spectra of semi-conductor noise and of flicker effect, PHYSICA 16:(4) pp. 359–372 (1950)
[25] Mar A, Analog Devices, inc. DSP Division, Digital signal processing applications using the ADSP-2100 family, Prentice Hall, 1990, ISBN:9780132129787
[26] Brophy JJ, Current noise in silver β 'alumina ceramics and single crystals. JOURNAL OF APPLIED PHYSICS 61:(2) pp. 581-584 (1987)

8.3 References for Chapter 2

[1] Chen Tsong-Ming, Yassine AM, Electrical noise and VLSI interconnect reliability. IEEE TRANSACTIONS ON ELECTRON DEVICES, 41:(11) pp. 2165-2172. (1994)

[2] Bareikis V, Katilius R (Eds.) Noise in Physical Systems and 1/f Fluctuations, Palanga, Lithuania, pp. 573-625. (1995)

[3] Vandamme LKJ, Noise as a diagnostic tool for quality and reliability of electron devices. IEEE TRANSACTIONS ON ELECTRON DEVICES 41:(11) pp. 2176-2187. (1994)

[4] Jones BK, Xu YZ, Measurement of the electrical properties of electromigration specimens. REVIEW OF SCIENTIFIC INSTRUMENTS 66:(9) pp. 4676-4680. (1995)

[5] Jones BK, Characterisation of electromigration damage by multiple electrical measurements. MICROELECTRONICS RELIABILITY 33:(11-12) pp. 1829-1840. (1993)

[6] Jones BK, Electrical measurements as early indicators of electromigration failure. MICROELECTRONICS RELIABILITY 35:(1) pp. 13-25. (1995)

[7] Dagge K, Frank W, Seeger A, Stoll H, 1/f noise as an early indicator of electromigration damage in thin metal films. APPLIED PHYSICS LETTERS 68:(9) pp. 1198-1200. (1996)

[8] Çelik-Butler Z, Ye M, Prediction of electromigration failure in W/Al-Cu multilayered metallizations by 1/f noise measurements. SOLID-STATE ELECTRONICS 35:(9) pp. 1209-1212. (1992)

[9] Sanchez Jr JE, Pham V Materials Reliability in Microelectronics, Pittsburgh: Materials Research Society (edited by Borgesen P et al), p. 459. (1995)

[10] Dagge K, Briggmann J, Seeger A, Stoll H, Reuter C, Conf. on Noise in Physical Systems and 1/f Fluctuations (AIP Conf. Proc. 285) (St Louis, USA, 1993), p. 603. (1993)

[11] Howes MJ, Morgan DV (Eds.), Reliability and Degradation of Semiconductor Devices and Circuits. New York: Wiley (1981)

[12] Gangulee A, d'Heurle FM, Mass transport during electromigration in aluminum-magnesium thin films. THIN SOLID FILMS 25:(2) pp. 317-325. (1975)

[13] Pierce JM, Thomas ME, Electromigration in aluminum conductors which are chains of single crystals. APPLIED PHYSICS LETTERS 39:(2) pp. 165-168. (1981)

[14] Stauffer D, Aharony A, Introduction to Percolation Theory. London: Taylor and Francis (1992)

[15] Rammal R, Tannous C, Tremblay AMS, 1/f noise in random resistor networks: Fractals and percolating systems. PHYSICAL REVIEW A 31:(4) pp. 2662-2671. (1985)

[16] Rammal R, Tannous C, Breton P, Tremblay AMS, Flicker (1/f) noise in percolation networks: A new hierarchy of exponents. PHYSICAL REVIEW LETTERS 54:(15) pp. 1718-1721. (1985)

[17] Batrouni GG, Hansen A, Larson B, Current distribution in the three-dimensional random resistor network at the percolation threshold. PHYSICAL REVIEW E - STATISTICAL PHYSICS, PLASMAS, FLUIDS, AND RELATED INTERDISCIPLINARY TOPICS 53:(3) pp. 2292-2297. (1996)

[18] Kiss LB, Svedlindh P, New noise exponents in random conductor-superconductor and conductor-insulator mixtures. PHYSICAL REVIEW LETTERS 71:(17) pp. 2817-2820. (1993)
[19] Kiss LB, Larsson T, Svedlindh P, Lundgren L, Ohlsén H, Ottosson M, Hudner J, Stolt L, Conductance noise and percolation in YBa2Cu3O7 thin films. PHYSICA C: SUPERCONDUCTIVITY AND ITS APPLICATIONS, 207:(3-4) pp. 318-332. (1993)
[20] Lust LM, Kakalios J, Computer simulations of conductance noise in a dynamical percolation resistor network. Physical Review E 50:(5) pp. 3431-3435. (1994)
[21] Lust LM, Kakalios J, Dynamical percolation model of conductance fluctuations in hydrogenated amorphous silicon. PHYSICAL REVIEW LETTERS 75:(11), pp. 2192-2195. (1995)
[22] Seidler GT, Solin SA, Marley AC, Dynamical current redistribution and non-gaussian 1/f noise. PHYSICAL REVIEW LETTERS 76:(17) pp. 3049-3052. (1996)
[23] de Arcangelis L, Redner S, Random fuse model for breaking processes. JOURNAL DE PHYSIQUE. LETTRES 46:(13) pp. 585-590. (1985)
[24] Wu K, Bradley RM, Theory of electromigration failure in polycrystalline metal films. PHYSICAL REVIEW B 50:(17) pp. 12468-12488. (1994)
[25] Sornette D, Vanneste C, Dynamics and memory effects in rupture of thermal fuse networks. PHYSICAL REVIEW LETTERS 68:(5) pp. 612-615. (1992)
[26] Ohtsuki T, Keyes T, Biased percolation: forest fires with wind. JOURNAL OF PHYSICS A: MATHEMATICAL AND GENERAL, 19, pp. L281-L287 (1986)
[27] Frey E, Täuber UC, Schwabl F, Crossover from isotropic to directed percolation. PHYSICAL REVIEW E, 49:(6) p 5058 (1994)
[28] Kertesz J, Vicsek T, Oriented bond percolation. JOURNAL OF PHYSICS C: SOLID STATE PHYSICS 13:(14) p. L343 (1980)
[29] Spence R, Linear Active Network. London: Wiley - Interscience (1970)
[30] Hooge FN, Kleinpenning TGM, Vandamme LKJ, Experimental studies on 1/f noise. REPORTS ON PROGRESS IN PHYSICS 44:(5) pp. 479-532. (1981)

8.4 References for Chapter 3

[1] www.thinksrs.com
[2] www.ni.com
[3] www.analog.com
[4] www.linear.com
[5] www.ti.com
[6] Mar A, Analog Devices, inc. DSP Division, Digital signal processing applications using the ADSP-2100 family, Prentice Hall, 1990, ISBN:9780132129787
[7] Kester W (ed), Mixed-signal and DSP design techniques, Newnes, 2003, ISBN-13: 978-0750676113, http://www.analog.com/en/content/mixed_signal_dsp_design_book/fca.html
[8] Kester W (ed), Data conversion handbook, Newnes, 2005, ISBN-13: 978-0750678414, http://www.analog.com/library/analogDialogue/archives/39-06/data_conversion_handbook.html
[9] Smith SW, The Scientist & Engineer's Guide to Digital Signal Processing, California Technical Pub.; 1st edition, 1997, ISBN-13: 978-0966017632, http://www.dspguide.com/

8.5 References for Chapter 4

[1] Benzi R, Sutera A, Vulpiani A, The mechanism of stochastic resonance. JOURNAL OF PHYSICS A: MATHEMATICAL AND GENERAL 14:(11), art. no. 006, pp. L453-L457. (1981)

[2] Nicolis C, Nicolis G, Stochastic aspects of climatic transitions - additive fluctuations. TELLUS 33:(3), pp. 225-234. (1981)

[3] Moss F, Bulsara A, Shlesinger M, Proc. NATO adv. Research workshop on stochastic resonance in physics and biology. JOURNAL OF STATISTICAL PHYSICS 70 (1993)

[4] Bulsara AR, Chillemi S, Kiss LB, McClintock PVE, Mannella R, Marchesoni F, Nicolis K, Wiesenfeld K, Int. Workshop on fluctuations in physics and biology: Stochastic resonance, signal processing and related phenomena. NUOVO CIMENTO D 17. (1995)

[5] Wiesenfeld K, Moss F, Stochastic resonance and the benefits of noise: From ice ages to crayfish and SQUIDs. NATURE 373:(6509), pp. 33-36. (1995)

[6] Collins, JJ, Chow CC, Imhoff TT, Aperiodic stochastic resonance in excitable systems. PHYSICAL REVIEW E 52 (4), pp. R3321-R3324. (1995)

[7] Collins JJ, Chow CC, Imhoff TT, Stochastic resonance without tuning. NATURE 376:(6537), pp. 236-238. (1995)

[8] DeWeese M, Bialek W, Information flow in sensory neurons. Il NUOVO CIMENTO D 17:(7-8), pp. 733-741. (1995)

[9] Fauve S, Heslot F, Stochastic resonance in a bistable system. PHYSICS LETTERS A 97:(1-2), pp. 5-7. (1983)

[10] Gammaitoni L, Hänggi P, Jung P, Marchesoni F, Stochastic Resonance. REVIEWS OF MODERN PHYSICS 70:(1) pp. 223–287. (1998)

[11] Chapeau-Blondeau F, Godivier X, Theory of stochastic resonance in signal transmission by static nonlinear systems. PHYSICAL REVIEW E - STATISTICAL PHYSICS, PLASMAS, FLUIDS, AND RELATED INTERDISCIPLINARY Topics 55:(2), pp. 1478-1495. (1997)

[12] McNamara B, Wiesenfeld K, Roy R, Observation of stochastic resonance in a ring laser. PHYSICAL REVIEW LETTERS 60:(25), pp. 2626-2629. (1988)

[13] McNamara B, Wiesenfeld K, Theory of stochastic resonance. PHYSICAL REVIEW A 39:(9), pp. 4854-4869. (1989)

[14] Goychuk I, Hänggi P, Stochastic resonance in ion channels characterized by information Theory. PHYSICAL REVIEW E 61 pp. 4272–4280. (2000)

[15] Bulsara A, Jacobs EW, Zhou T, Moss F, Kiss L, Stochastic resonance in a single neuron model: Theory and analog simulation. JOURNAL OF THEORETICAL BIOLOGY 152:(4), pp. 531-555. (1991)

[16] Longtin A, Bulsara A, Moss F, Time-interval sequences in bistable systems and the noise-induced transmission of information by sensory neurons. PHYSICAL REVIEW LETTERS 67:(5), pp. 656-659. (1991)

[17] Longtin A, Bulsara A, Pierson D, Moss F, Bistability and the dynamics of periodically forced sensory neurons. BIOLOGICAL CYBERNETICS 70:(6), pp. 569-578. (1994)

[18] Douglass JK, Wilkens L, Pantazelou E, Moss F, Noise enhancement of information transfer in crayfish mechanoreceptors by stochastic resonance. NATURE 365:(6444), pp. 337-340. (1993)

[19] Russett DF, Wilkens LA, Moss F, Use of behavioural stochastic resonance by paddle fish for feeding. NATURE 402:(6759), pp. 291-294. (1999)

[20] Bezrukov SM, Vodyanoy I, Noise-induced enhancement of signal transduction across voltage-dependent ion channels. NATURE 378:(6555), pp. 362-364. (1995)
[21] Jung P, Threshold devices: Fractal noise and neural talk. PHYSICAL REVIEW E 50:(4), pp. 2513-2522. (1994).
[22] Wiesenfeld, K., D. Pierson, E. Pantazelou, C. Dames, and F. Moss, Stochastic resonance on a circle. PHYSICAL REVIEW LETTERS, 72:(14) pp. 2125-2129 (1994)
[23] Gammaitoni L, Stochastic resonance and the dithering effect in threshold physical systems. PHYSICAL REVIEW E 52:(5), pp. 4691-4698. (1995)
[24] Kester W, ADC input noise: The good, the bad and the ugly. Is no noise good noise? ANALOG DIALOGUE 40:(2), pp. 13-17. (2006)
[25] De-chun G, Gang H, Xiao-Dong W, Chun-Yan Y, Guang-Rong Q, Rong L, Da-fu D, Experimental study of the signal-to-noise ratio of stochastic resonance systems, PHYSICAL REVIEW A 46:(6) pp. 3243-3249 (1992)
[26] De-chun G, Gang H, Xiao-Dong W, Chun-Yan Y, Guang-Rong Q, Rong L, Da-fu D, Erratum: Experimental study of the signal-to-noise ratio of stochastic resonance systems. PHYSICAL REVIEW A 48:(6) pp. 4862-4862 (1993)
[27] Dykman MI, Luchinsky DG, Mannella R, McClintock PVE, Stein ND, Stocks NG, Stochastic resonance in perspective. Il NUOVO CIMENTO D 17:(7-8), pp. 661-683. (1995)
[28] Kiss LB, Possible breakthrough: Significant improvement of signal to noise ratio by stochastic resonance. CHAOTIC, FRACTAL, AND NONLINEAR SIGNAL PROCESSING 375, pp. 382-396. (1996)
[29] S O Rice, "Mathemathical analysis of random noise", BELL SYSTEMS TECHNOLOGY JOURNAL, 23, 46-156 (1945).
[30] Khovanov IA, Anishchenko VS, Nonlinear signal transformation in the regime of SR. AIP Conference Proceedings, 411, p. 267 (1997)
[31] Bulsara AR, Zador A, Threshold detection of wideband signals: A noise-induced maximum in the mutual information. PHYSICAL REVIEW E - STATISTICAL PHYSICS, PLASMAS, FLUIDS, AND RELATED INTERDISCIPLINARY TOPICS 54:(3), pp. R2185-R2188. (1996)
[32] Heneghan C, Chow CC, Collins JJ, Imhoff TT, Lowen SB, Teich MC, Information measures quantifying aperiodic stochastic resonance. PHYSICAL REVIEW E - STATISTICAL PHYSICS, PLASMAS, FLUIDS, AND RELATED INTERDISCIPLINARY TOPICS 54:(3), pp. R2228-R2231. (1996)
[33] Godivier X, Chapeau-Blondeau F, Stochastic resonance in the information capacity of a nonlinear dynamic system. INTERNATIONAL JOURNAL OF BIFURCATION AND CHAOS IN APPLIED SCIENCES AND ENGINEERING 8:(3), pp. 581-589. (1998)
[34] Hänggi P, Inchiosa ME, Fogliatti D, Bulsara AR, Nonlinear stochastic resonance: The saga of anomalous output-input gain. PHYSICAL REVIEW E 62 pp. 6155–6163. (2000)
[35] Liu F, Yu Y, Wang W, Signal-to-noise ratio gain in neuronal systems. PHYSICAL REVIEW E - STATISTICAL, NONLINEAR, AND SOFT MATTER PHYSICS 63:(5 I), pp. 519121-519124. (2001)
[36] Hidaka I, Nozaki D and Yamamoto Y, Functional stochastic resonance in the human brain: Noise induced sensitization of baroreflex system. PHYSICAL REVIEW LETTERS 85 pp. 3740-3743. (2000)

[37] Nozaki D, Yamamoto Y, Enhancement of stochastic resonance in a FitzHugh-Nagumo neuronal model driven by colored noise. PHYSICS LETTERS, SECTION A: GENERAL, ATOMIC AND SOLID STATE Physics 243:(5-6), pp. 281-287. (1998)
[38] Nozaki D, Mar DJ, Grigg P and Collins JJ, Effects of Colored Noise on Stochastic Resonance in Sensory Neurons. PHYSICAL REVIEW LETTERS 82 p. 2402 (1999)
[39] Nozaki D, Collins JJ and Yamamoto Y, Mechanism of stochastic resonance enhancement in neuronal models driven by 1/f noise, PHYSICAL REVIEW E 60 p.4637 (1999)
[40] Godivier X, Chapeau-Blondeau F, Stochastic resonance in the information capacity of a nonlinear dynamic system. INTERNATIONAL JOURNAL OF BIFURCATION AND CHAOS IN APPLIED SCIENCES AND ENGINEERING 8:(3), pp. 581-589. (1998)
[41] Misono M, Kohmoto T, Fukuda Y, Kunitomo M, Noise-enhanced transmission of information in a bistable system. PHYSICAL REVIEW E - STATISTICAL PHYSICS, PLASMAS, FLUIDS, AND RELATED INTERDISCIPLINARY TOPICS, 58:(5 SUPPL. A), pp. 5602-5607. (1998)
[42] Minamikawa T, Tanimoto N, Hashimoto M, Araki T, Kobayashi M, Fujita K, Kawata S, Jitter reduction of two synchronized picosecond mode-locked lasers using balanced crosscorrelator with two-photon detectors. APPLIED PHYSICS LETTERS 89 (2006) 191101
[43] Yoshidaa Y, Mizutania Y, Kozawaa T, Saekia A, Sekia S, Tagawaa S, Ushidab K, Development of laser-synchronized picosecond pulse radiolysis system. RADIATION PHYSICS AND CHEMISTRY 60:(4-5) pp. 313-318 (2001)
[44] Kalisz J, Review of methods for time interval measurements with picosecond resolution. METROLOGIA 41 p. 17 (2004)
[45] Dudek P, A High-Resolution CMOS Time-to-Digital Converter Utilizing a Vernier Delay Line. IEEE TRANSACTIONS ON SOLID-STATE CIRCUITS 35:(2) pp. 240-247 (2000)
[46] Aloisio A, Branchini P, Cicalese R, Giordano R, Izzo V, Loffredo S, Lomoro R, High-Resolution Time-to-Digital Converter in Field Programmable Gate Array. Topical Workshop on Electronics for Particle Physics, Naxos, Greece (Sep 2008) pp. 383-387
[47] Jones B, 83C51FA/FB PCA cookbook, Intel Application Note AP-415 (1994) see also the datasheet of the processor C8051F120 (Silicon Laboratories, www.silabs.com)
[48] Ito S, Nishimura S, Kobayashi H, Uemori S, Tan Y, Takai N, Yamaguchi TJ, Niitsu K, Stochastic TDC architecture with self-calibration, Circuits and Systems (APCCAS), 2010 IEEE Asia Pacific Conference on, 978-1-4244-7454-7 pp. 1027 - 1030 (2010)
[49] Straayer MZ, A Multi-Path Gated Ring Oscillator TDC With First-Order Noise Shaping. IEEE JOURNAL OF SOLID-STATE CIRCUITS 44:(4) pp. 1089-1098 (2009)
[50] Suchenek M, Picosecond resolution programmable delay line. MEASUREMENT SCIENCE AND TECHNOLOGY 20:(11), (2009)

8.6 References for Chapter 5

[1] Kish LB, Vajtai R, Granqvist CG, Extracting information from noise spectra of chemical sensors: Single sensor electronic noses and tongues. SENSORS AND ACTUATORS, B: CHEMICAL, 71:(1-2), pp. 55-59. (2000)

[2] Schmera G, Kwan C, Ajayan P, Vajtai R, Kish LB, Fluctuation-enhanced sensing: Status and perspectives. IEEE SENSORS JOURNAL 8:(6), art. no. 4529215, pp. 714-719. (2008)

[3] Gottwald P, Kincses Zs, Szentpali B, Anomalous additional low-frequency noise of surface origin generated in Thin GaAs Layers. Unsolved Problems of Noise (UPoN'96) pp. 122-127. (1997)

[4] Vidybida AK, Adsorption-desorption noise can be used for improving selectivity. SENSORS AND ACTUATORS, A: PHYSICAL 107:(3), pp. 233-237. (2003)

[5] Vidybida AK, Usenko AS, Rospars J-P, Selectivity improvement in a model of olfactory receptor neuron with adsorption-desorption noise. JOURNAL OF BIOLOGICAL SYSTEMS 16 (4), pp. 531-545. (2008)

[6] Kish LB, Smulko J, Heszler P, Granqvist C-G, On the sensitivity, selectivity, sensory information and optimal size of resistive chemical sensors. NANOTECHNOLOGY PERCEPTIONS 3, pp. 43-52. (2007)

[7] Szczurek A, Szecówka PM, Licznerski BW, Application of sensor array and neural networks for quantification of organic solvent vapours in air. SENSORS AND ACTUATORS, B: CHEMICAL 58:(1-3), pp. 427-432. (1999)

[8] Gomri S, Seguin J-L, Aguir K, Modeling on oxygen chemisorption-induced noise in metallic oxide gas sensors. SENSORS AND ACTUATORS, B: CHEMICAL 107:(2), pp. 722-729. (2005)

[9] Gomri S, Seguin J-L, Guerin J, Aguir K, Adsorption-desorption noise in gas sensors: Modelling using Langmuir and Wolkenstein models for adsorption. SENSORS AND ACTUATORS, B: CHEMICAL 114:(1), pp. 451-459. (2006)

[10] Taguchi N, US Patent 3644795 (1972)

[11] Solis JL, Kish LB, Vajtai R, Granqvist CG, Olsson J, Schnürer J, Lantto V, Identifying natural and artificial odours through noise analysis with a sampling-and-hold electronic nose. SENSORS AND ACTUATORS, B: CHEMICAL 77:(1-2), pp. 312-315. (2001)

[12] Kong J, Franklin NR, Zhou C, Chapline MG, Peng S, Cho K, Dai H. Nanotube molecular wires as chemical sensors. SCIENCE 287:(5453), pp. 622-625. (2000)

[13] Comini E, Metal oxide nano-crystals for gas sensing. ANALYTICA CHIMICA ACTA 568:(1-2), pp. 28-40. (2006)

[14] Mäklin J, Mustonen T, Kordás K, Saukko S, Tóth G, Vähäkangas J, Nitric oxide gas sensors with functionalized carbon nanotubes. PHYSICA STATUS SOLIDI (B) BASIC RESEARCH 244:(11), pp. 4298-4302. (2007)

[15] Wan Q, Li QH, Chen YJ, Wang TH, He XL, Li JP, Lin CL, Fabrication and ethanol sensing characteristics of ZnO nanowire gas sensors. APPLIED PHYSICS LETTERS 84:(18), pp. 3654-3656. (2004)

[16] Simon I, Bârsan N, Bauer M, Weimar U, Micromachined metal oxide gas sensors: Opportunities to improve sensor performance. SENSORS AND ACTUATORS, B: CHEMICAL 73:(1), pp. 1-26. (2001)

[17] Sinha N, Ma J, Yeow JTW, Carbon nanotube-based sensors. JOURNAL OF NANOSCIENCE AND NANOTECHNOLOGY 6:(3), pp. 573-590. (2006)

[18] Cantalini C, Valentini L, Armentano I, Kenny JM, Lozzi L, Santucci S, Carbon nanotubes as new materials for gas sensing applications. JOURNAL OF THE EUROPEAN CERAMIC SOCIETY, 24:(6), pp. 1405-1408. (2004)
[19] Zettl A, Extreme oxygen sensitivity of electronic properties of carbon nanotubes. SCIENCE 287:(5459), pp. 1801-1804. (2000)
[20] Kotarski M, Smulko, J, Noise measurement set-ups for fluctuations-enhanced gas sensing. METROLOGY AND MEASUREMENT SYSTEMS 16:(3) pp. 457-464 (2009)
[21] Smulko J, The measurement setup for gas detection by resistance fluctuations of gas sensors. Instrumentation and Measurement Technology Conference, 2006. IMTC 2006. Proceedings of the IEEE 2028-2031 (2006)
[22] Chang H-C, Kish LB, King MD, Kwan C, Fluctuation-enhanced sensing of bacterium odors. SENSORS AND ACTUATORS, B: CHEMICAL 142:(2), pp. 429-434. (2009)
[23] Chang H-C, Kish LB, King MD, Kwan C, Binary fingerprints at fluctuation-enhanced sensing. SENSORS 10:(1), pp. 361-373. (2010)
[24] Kedem B, Time Series Analysis by Higher Order Crossings. IEEE Press, New York, 1994
[25] Vapnik VN, Statistical Learning Theory. New York: Wiley, 1998.
[26] Burges C, A tutorial on support vector machines for pattern recognition. In "Data Mining and Knowledge Discovery". Kluwer Academic Publishers, Boston, 1998, (Volume 2).

8.7 References for Chapter 6

[1] Knuth D E, The Art of Computer Programming, Volume 2: Seminumerical Algorithms, Third ed. Addison-Wesley, 1997, ISBN-13: 978-0201896848

[2] Yalcin ME, Suykens JAK, Vandewalle J, True random bit generation from a double-scroll attractor. IEEE TRANSACTIONS ON CIRCUITS AND SYSTEMS I: Regular Papers, , 51:(7) pp. 1395-1404 (2004)

[3] Sunar B, Martin WJ, Stinson DR, A provably secure true random number generator with built-in tolerance to active attacks, IEEE TRANSACTIONS ON COMPUTERS, 56:(1) pp.109-119 (2007)

[4] Kish LB, Totally secure classical communication utilizing Johnson (-like) noise and Kirchoff's law. PHYSICS LETTERS, SECTION A: GENERAL, ATOMIC AND SOLID STATE PHYSICS 352:(3), pp. 178-182. (2006)

[5] Cho A, Simple noise may stymie spies without quantum weirdness. SCIENCE, 309:(5744), p.p. 2148. (2005)

[6] Kish LB, Protection against the man-in-the-middle-attack for the kirchhoff-loop-johnson(-like)-noise cipher and expansion by voltage-based security. FLUCTUATION AND NOISE LETTERS 6:(1), pp. L57-L63. (2006)

[7] Kish LB, Mingesz R, Totally secure classical networks with multipoint telecloning (teleportation) of classical bits through loops with Johnson-like noise. FLUCTUATION AND NOISE LETTERS 6:(2), pp. C9-C21. (2006)

[8] Kish LB, Methods of Using Existing Wire Lines (power lines, phone lines, internet lines) for Totally Secure Classical Communication Utilizing Kirchoff's Law and Johnson-like Noise, http://arxiv.org/abs/physics/0610014.

[9] Scheuer J, Yariv A, A classical key-distribution system based on Johnson (like) noise-How secure? PHYSICS LETTERS, SECTION A: GENERAL, ATOMIC AND SOLID STATE PHYSICS 359:(6), pp. 737-740. (2006)

[10] Kish LB, Response to Scheuer-Yariv: "A classical key-distribution system based on Johnson (like) noise-how secure?" PHYSICS LETTERS, SECTION A: GENERAL, ATOMIC AND SOLID STATE PHYSICS 359:(6), pp. 741-744. (2006)

[11] Hao F, Kish's key exchange scheme is insecure. IEE PROCEEDINGS: INFORMATION SECURITY 153:(4), pp. 141-142. (2006)

[12] Kish LB, Response to Feng Hao's paper "Kish's key exchange scheme is insecure". FLUCTUATION AND NOISE LETTERS 6:(4), pp. C37-C41. (2006)

[13] Bennett CH, Brassard G, Crepeau C, Maurer UM, Generalized privacy amplification. IEEE TRANSACTIONS ON INFORMATION THEORY 41:(6 pt 2), pp. 1915-1923. (1995)

[14] Ursin R, Tiefenbacher F, Schmitt-Manderbach T, Weier H, Scheidl T, Lindenthal M, Blauensteiner B, Jennewein T, Perdigues J, Trojek P, Ömer B, Fürst M, Meyenburg M, Rarity J, Sodnik Z, Barbieri C, Weinfurter H, Zeilinger A, Entanglement-based quantum communication over 144km. NATURE PHYSICS, 3:(7), pp. 481-486. (2007)

[15] Liu PL, A Key Agreement Protocol Using Band-Limited Random Signals and Feedback, JOURNAL OF LIGHTWAVE TECHNOLOGY 27: (23) 5230-5234 (2009)

[16] Liu PL, Key Exchange Using Random Signals and Feedback-Statistical Analysis, JOURNAL OF LIGHTWAVE TECHNOLOGY 28: (1) 65-70 (2010)

[17] Liu PL, Josan MS, QUANTIZATION NOISE IN STATISTICAL KEY EXCHANGE, FLUCTUATION AND NOISE LETTERS 10: (3) 239-247 (2011)

9 Acknowledgement

I'm grateful to László Kish for helping me so much to start my scientific career and for his continuous support.

I thank my colleagues, Péter Makra and Róbert Mingesz for their reliable and essential work in my research group. I thank them and my students, Gergely Vadai and Gergely Makan for their help to improve the manuscript.

I'm indebted to Tibor Csendes, János Csirik and Zoltán Fülöp for their valuable advises and for their kind support.

I would never achieve my results without my collaborators, coauthors in my primary and interdisciplinary research fields, I thank all of them. Special thanks to Angéla Barna, Sergey Bezrukov, Zoltán Bozóki, Norbert Csík, Imre Dékány, Nobuko Fuchikami, Tamás Fülei, Claes-Göran Granqvist, Péter Heszler, Zoltán Kántor, Attila Kardos, Péter Kocsis, Zoltán Kónya, Katalin Kopasz, Ákos Kukovecz, Károly Lőrincz, Péter Maróti, János Mellár, Frank Moss, Lino Reggiani, László Rudas, László Halmai, Róbert Pap, Cecilia Pennetta, László Sághy, Janusz Smulko, Peter Svedlindh, Márta Szekeres, Etelka Tombácz, Tamás Török, György Trefán, Imre Ungi, Róbert Vajtai, Lode Vandamme, Csaba Visy, Éva Zöllei.

I thank all my colleagues at the Institute of Informatics and at the Institute of Physics for providing supportive and friendly atmosphere.